ESTIMATING MIXING PARAMETERS USING OCEAN BUOYANCY GLIDER HYDROGRAPHY AND VEHICLE DYNAMICS: APPLICATIONS TO GULF LOOP CURRENT STRUCTURE

A Dissertation

by

SAKIB MAHMUD

Submitted to the Graduate and Professional School of
Texas A&M University
in partial fulfillment of the requirements for the degree of

DOCTOR OF PHILOSOPHY

Chair of Committee,	Steven F. DiMarco
Committee Members,	Anthony Knap
	James Kaihatu
	Kerri Whilden
Head of Department,	Shari Yvon-Lewis

August 2022

Major Subject: Oceanography

ABSTRACT

This dissertation has combined observations from four Slocum glider missions in the deep Gulf of Mexico to quantify the turbulent kinetic energy (TKE) dissipation rates (ϵ) and diffusive mixing processes in the basin. The Thorpe scale (TM) method is used to estimate ϵ and then used to construct depth ϵ profiles (surface to 1000 m) using the Large Eddy Method (LEM). The accuracy of the TM-LEM estimates are compared and quantified against direct estimates from a simultaneous /co-located MicroRider deployment in the Gulf of Mexico (i.e., a glider equipped with MicroRider). Survey-averaged profiles of the three methods are compared and found to be within the range of expected error, i.e., within a factor of 2. Profile to profile comparison of ϵ reveals that LEM overestimates when the magnitude of ϵ is small. The overestimation is attributed to the stratification-dependent detection limits of the LEM and is mostly observed in deep water, where ϵ falls close to the noise level of LEM. Spectral comparison of dissipation rates from the three methods (using histograms of occurrence) confirms that the LEM and TM are able to capture dissipation rate variability greater than $1 \times 10^{-9}\, Wkg^{-1}$; however, less than this limit, only the direct measurement of TKE dissipation rate (in regions of weak vertical density gradients) are robust. Despite this limitation, the TM -LEM-derived dissipation rate estimates are able to provide structures that are interpretable as associated with the underlying physical processes of the deep ocean. Maps showing the temporal and spatial variability of ϵ are able to reveal the well-defined turbulence structure of LCE and LC. Eddy-induced elevated ϵ are observed around the core of LC and LCE, but the interior of the eddy core is relatively quiescent when compared to the oceanic frontal regions of the eddy. Diapycnal mixing around the eddy cores is suppressed due to the presence of stronger stratification. Away from the eddy cores, where stratification is less, diapycnal mixing is enhanced. The analysis quantifying the relative strength of the diffusion processes, using Turner Angle and density ratio, concluded that salt-fingering is the dominant double-diffusive process in the GoM and is related to proximity to the LC and to depth of observation influence the strength of the salt-fingering in the water column. The potential for fine-structure thermohaline staircases is

quantified and observations of irregular shape staircases in the deep GoM are reported for the first time. The glider-based measurements provide an economical option to estimate ocean turbulence and has the potential to fill the gaps between the direct microstructure measurements provides opportunity to obtain mixing parameters of the world ocean in the absence of direct microstructure observations.

DEDICATION

In loving memory of my mother, Delwara Begum, and my father, Salauddin Ahamed.

ACKNOWLEDGMENTS

I would like to thank my committee chair, Dr. Steven F. DiMarco, for his support as a mentor and as a friend and colleague. Even at my lowest point, your support and confidence in me helped me get here.

For their leadership and support throughout my time at A&M and with my research, I would also like to extend a heartfelt thank you full of gratitude to my committee members, Dr. Anthony Knap, Dr. James Kaihatu, and Dr. Kerri Whilden.

No one achieves success in a vacuum. Without the team of support I have had from friends who helped me go backpacking when I needed a break, from colleagues who imparted their knowledge to me through all five years at A&M. My department faculty, staff, and amazing people of GERG for their guidance and support, I could not have done it without each and every one of you. I have had many colleagues who acted as both friends and mentors during my graduate education.

I would like to thanks to Dr. Zhankun Wang of NOAA for his expert opinion and support throughout this research.

I would like to extend a heartfelt thanks to Dr. Ruth Perry of Shell Upstream Americas for her continuous motivation and financial support.

My family laid a foundation for me to build my success on. They instilled in me the values of hard work, perseverance, and belief in myself that have culminated in this work product. To my parents and my sister, you are always in my heart, I love you, and thank you.

Above all I would like to thank my lovely wife Ashley for her love, constant support, and motivation for keeping me focused over the past few years. Thank you for being my editor and proofreader. I owe you everything.

CONTRIBUTORS AND FUNDING SOURCES

Contributors

This work was supported by a dissertation committee consisting of Dr. Steven F. DiMarco, Dr. Anthony Knap of the Department of Oceanography, Dr. James Kaihatu of the Department of Civil & Environmental Engineering and Ocean Engineering and Dr. Kerri Whilden of FUGRO. The data described in chapter II was provided by Dr. Steven F. DiMarco under the project of Gulf of Mexico Mixing (GoMix) experiment and Gulf of Mexico Integrated Spill Response Consortium (GISR) project from funding from the Gulf of Mexico Research Initiative (GoMRI). All other work conducted for the dissertation was completed by the student independently under the guidance from the advisor and the committee's members. MATLAB® code for MicroRider data processing was provided by Dr. Zhankun Wang (NOAA NCEI).

Funding Sources

This research was partially funded by the Shell Upstream Americas, NOAA Center for Sponsored Coastal Ocean Research (Contract No. NA15NOS4780168), Texas OneGulf RESTORE, the Texas General Land Office, the Gulf of Mexico Coastal Ocean Observing System Regional Association (GCOOS) and the Gulf of Mexico Research Initiative (by multiple contracts with Department of Oceanography, the Geochemical and Environmental Research Group (TAMU). Partial funding was also generously contributed to by the Vettlesen Foundation thru an award to A.H. Knap (TAMU/GERG).

NOMENCLATURE

GoM	Gulf of Mexico
SUW	Subtropical Under Water
TACW	Tropic Atlantic Central water
GCW	Gulf Common Water
AAIW	Antarctic Intermediate Water
LC	Loop Current
LCE	Loop Current Eddy
TKE	Turbulence Kinetic Energy
GoMix	Gulf of Mexico Mixing Experiment
CTD	Conductivity Temperature Depth
CDOM	Colored Dissolved Organic Matter
SSHA	Sea Surface Height Anomaly
FFT	Fast Fourier Transform
TM	Thorpe Scale Method
LEM	Large Eddy Method

TABLE OF CONTENTS

Page

LIST OF FIGURES

FIGURE Page

LIST OF TABLES

TABLE Page

1. INTRODUCTION

1.1 Ocean Mixing

This dissertation deals with the turbulent and double-diffusive mixing processes in the Loop Current (LC) and Loop Current Eddies (LCEs) in the Gulf of Mexico (GoM) using the data collected by underwater gliders. Further, a new methodology was developed to use the Large Eddy Method (LEM) to infer turbulence kinetic energy (TKE) dissipation rates (ϵ) without microstructure measurement. The spatial scale of ocean physical processes ranges from a fraction of a millimeter to thousands of kilometers, and the temporal scale ranges from a fraction of a second to years (Dickey and Bidigare, 2005). Large-scale processes like winds, tides, and atmospheric buoyancy forcing with the order of 100–1000 km horizontal scale drives wave motions such as Rossby waves and internal waves and, basin-scale gyres, the meridional overturning circulation. The instabilities resulting from the large-scale physical processes ultimately lead to viscous dissipation at small scales (i.e., Kolmogorov scale, on the order of 1 cm) and cause mixing (MacKinnon et al., 2013). Studies show a wide range of spatial and temporal variability of the magnitude of mixing across different density layers, i.e., diapycnal mixing in the world ocean (Wunsch and Ferrari, 2004; Richards et al., 2009; Whalen et al., 2012; MacKinnon et al., 2017). The spatio-temporal patterns of diapycnal mixing in the surface ocean ($\approx$ upper 200 m) are driven by the forcing from the large-scale (spatial scale 100 - 1000 km) processes such as wind, tides, and buoyancy. In the ocean interior, the spatio-temporal patterns of diapycnal mixing are dominated by the generation, propagation, and dissipation of internal waves (spatial scale 1 - 100 km), shear-generated or double-diffusive instabilities (Gargett, 1989; Wunsch and Ferrari, 2004; Talley, 2011; MacKinnon et al., 2017).

In the ocean pycnocline, nearly all microstructure mixing is produced by the double-diffusion and the turbulence resulting from internal waves breaking (Gargett, 1989; Gregg, 2021). The term microstructure refers to the measurement of the fluctuation of ocean temperature, salinity,

and velocity ranges from the Kolmogorov scale to two orders of magnitude higher. As stated above, the generation, propagation, and dissipation of internal waves ultimately dissipate to small-scale turbulence and cause mixing. Double-diffusive instability plays an important role in oceanic mixing and is widely present in the world ocean (Schmitt, 2003; Schmitz Jr et al., 2005). In the ocean, the molecular diffusivity of heat is greater than that of salt in nearly two orders of magnitude. In a density stratified ocean, faster heat diffusion compared to salt leads to statically unstable temperature- and salinity-induced stratification, resulting in double-diffusion (Stern, 1960). An example of double-diffusive instability is salt-finger, a form of double diffusion that occurs when warm-salty water overlies above cold-fresh water (Talley, 2011; Schmitt, 2012).

1.2 How Ocean Mixing is Studied

As Gregg (2021) discussed (in a review book), the study of ocean mixing historically, up to the present day, is conducted in the following five ways: inference, processes studies, microstructure and tracer, finestructure observation, and integrated study. The measurement of ocean mixing requires high-resolution instruments. Therefore, before 1959 inference played a vital role in the study of ocean mixing. Inference of ocean mixing relies on simplified momentum (Ekman, 1905) or heat equations (Munk, 1966) to understand the underlying causes of large-scale processes.

In 1959, the first successful microstructure turbulence measurement was conducted via a hot-film anemometer (Grant et al., 1959). The anemometer probe was mounted on the nose of a heavy body and towed by a ship. Today, loosely tethered vertical microstructure profilers (VMP) deployed from research ships dominate the direct measurement of ocean turbulence (Lueck et al., 2002). Microstructure probes have been deployed on autonomous vehicles (Goodman et al., 2006; Goodman and Wang, 2009), floats (D'Asaro and Lien, 2000a; Whalen et al., 2012), CTD (conductivity, temperature and depth) (Wang et al., 2016), and gliders (Wolk et al., 2009; Fer et al., 2014; Wang et al., 2018; Molodtsov et al., 2020). Oceanographers additionally use various chemical tracers to estimate the net mixing rates between microstructure observations (Ledwell et al., 2016). The tracers are released at a specific depth depending on research objectives. After they are released, the concentration of the tracers is observed over time. These observations have led to a

better understanding of ocean diffusive and advective processes and mixing patterns.

Process studies involve highly focused observations, laboratory experiments, and theoretical models to advance understanding of specific ocean physical processes. They are useful in developing a hypothesis, refining a mathematical concept, or developing models that will lead to a deeper understanding of a process or phenomena. A noteworthy example of process study is the development of the theory of the salt finger, which was conducted in a small water tank (Stern, 1960).

The deployment of high-resolution instruments is expensive and relies on a highly trained workforce. Due to these cost-prohibitive restrictions, oceanographers often rely on finestructure observations of ocean mixing. The finestructure in the ocean is defined as the vertical fluctuations in temperature, salinity, density, velocity in the order of one meter to one hundred meters which can be sampled with standard CTD or ADCP (Acoustic Doppler Current Profiler). Finestructure observations are used to estimate mixing parameters from coarser-resolution (Order of meter) density (Thorpe, 1977) and/or shear and strain profiles (Kunze et al., 2006). Thorpe Scale (TM) analysis offers a methodology to study the ocean's small-scale mixing from coarser-resolution density (i.e., CTD) data when no microstructure measurement is available. Scientists have successfully used the TM to characterize turbulence in different contexts since 1977. Several studies, including numerical simulation (Thorpe, 2012) and observational (Howatt et al., 2021) show, TM can be applied to the CTD data collected by underwater gliders. Although TM using glider data reportedly overestimates the ϵ but effectively resolves the spatio-temporal distribution of the ϵ. (Howatt et al., 2021).

Integrated studies are composed of multiple programs to study ocean mixing and underlying physical processes. One example of an integrated mixing study is the Hawaii Ocean Mixing Experiment (HOME) (Pinkel et al., 2000). HOME complementary programs include analyzing historical data, modeling, and nearfield and farfield direct microstructure survey to understand the multi-scale nature and complex spatial geometry of the mixing process near the Hawaiian Ridge.

A list of commonly used platforms with the data type and applied methods are given in the table below:

Table 1.1: Methods of studying ocean mixing.

	Method	**Platform**	**Data Type**	**Measurement/ Estimate**
Inference	Theoretical			k_ρ, k_t, k_s^1
Process Studies	Observation, laboratory, model	Laboratory tank, observation[2]		
Microstructure	Measurement	Profilers, Floats, Gliders, AUV	High-resolution velocity temperature (Microscale)	$\epsilon, k_\rho, k_t, k_s, \Gamma$[3]
Tracer	Measurement	Ship		k_ρ^4
Finescale	Estimate	CTD, Floats, Gliders	Coarser-resolution CTD, velocity	$\epsilon, k_\rho, k_t, k_s^5$
Integrated	Combination of methods addressed above[6]			

[1]Munk (1966), [2]Stern (1960), [3]Goodman and Wang (2009), [4]Ledwell et al. (2016), [5]Thorpe (1977) Kunze et al. (2006), [6]Pinkel et al. (2000).
where, k_ρ = eddy diffusivity, k_t = eddy diffusivity of heat ,k_s = eddy diffusivity of salt, ϵ = Turbulence dissipation rates, Γ =mixing effieciency.

1.3 Underwater Glider as a platform for Ocean Mixing observations

The concept of an observing platform that can autonomously observe the world ocean and provide a comprehensive spatial and temporal view of the ocean interior was first presented by Stommel (1989). Nowadays, underwater gliders (and the close platform cousin ARGO floats) have become a ubiquitous platform for ocean observation because of their ability to provide critical data for many applications, including the military. The underwater glider is a buoyancy-driven ocean observing vehicle, which travels vertically through the water column (Eriksen et al., 2001; Sherman et al., 2001) (Fig. 1.1). Depending on the buoyancy pump, a glider can dive from the ocean surface to between 200 - 1000 m with a vertical speed as low as $\approx$ 0.1 m s^{-1}, and horizontal speed $\approx$ 0.25 m s^{-1} (Davis et al., 2002; Rudnick et al., 2016). Active piloting and near real-time reporting ability make gliders useful for observing mesoscale and submesoscale oceanic features like eddies and convective plumes (Rudnick et al., 2015; Margirier et al., 2017).

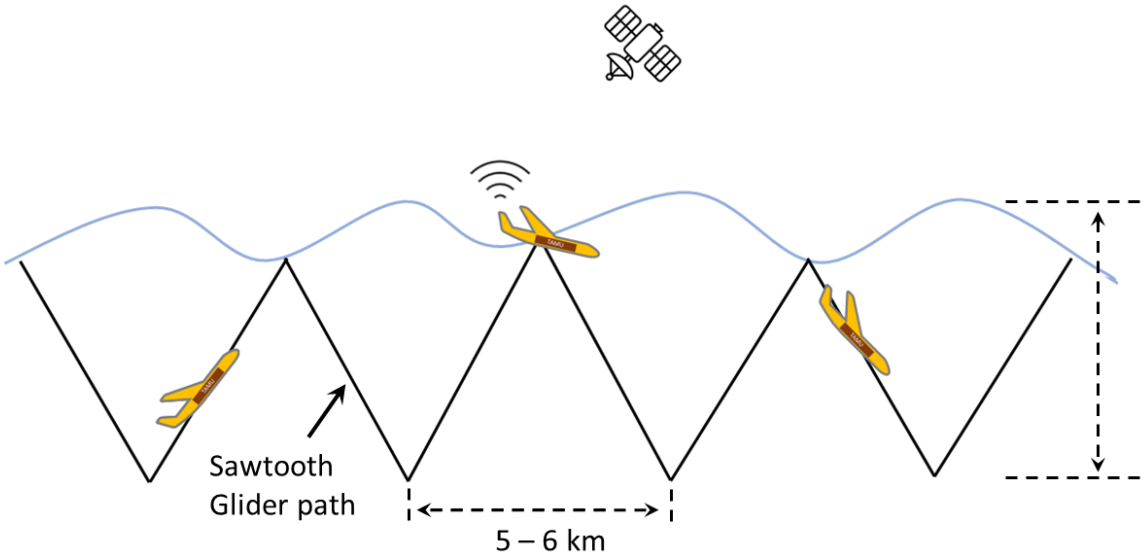

Figure 1.1: Schematic of glider movement in the water in a saw-tooth path. The glider transmits data through satellite when at the surface.

Gliders equipped with a turbulence package are used in numerous studies (Fig. 1.2) (Wolk et al., 2009; Fer et al., 2014; Palmer et al., 2015; Schultze et al., 2017; Molodtsov et al., 2020). The oceanic turbulence measurement requires precise measurements of environmental flow at the Kolmogorov scale. Instrumental vibration can disrupt the flow and introduce noise into the measurement. As a buoyancy-driven vehicle, glider offers relatively low noise from flight controlling mechanisms (Wolk et al., 2009; Fer et al., 2014), making it a suitable platform for microstructure observation. Wolk et al. (2009) first carried out turbulence measurements using a glider carrying a MicroRider. MicroRider is an oceanic microstructure profiler made by Rockland Scientific (Canada). The fast-response thermistor and shear probes (sampling rate of 512 Hz) of MicroRider measures the small-scale temporal fluctuations of temperature and velocity, respectively. Several studies have reported the statistical agreement (within a factor of 2) of vertically averaged profiles of ϵ from glider and VMP measurement (Wolk et al., 2009; Fer et al., 2014; Schultze et al., 2017).

Figure 1.2: Graduate student Christian Nygren deploying Slocum glider (Sverdrup) to study turbulence on the continental slope of Gulf of Mexico. Picture source: GERG Facebook page.

Glider data was used to estimate ϵ in the Nordic Overflow region (Beaird et al., 2012) and in the northeast Atlantic (Evans et al., 2018). This method to estimate ϵ using glider data is called the Large Eddy Method (LEM) (Beaird et al., 2012). As originally developed, the LEM requires directly measured turbulence profiles from the glider survey area to calibrate a proportionality constant to scale the LEM-derived ϵ. LEM estimates ϵ from the vertical velocity of water and

buoyancy frequency (N). The vertical velocity of water was estimated (Frajka-Williams et al., 2011) from glider hydrography and flight parameters of a Seaglider vehicle. Beaird method of LEM was developed in the weakly stratified Faroe Bank Channel and reportedly overestimated the ϵ at strong stratification (Evans et al., 2018). Therefore, caution needs to be taken to applying LEM in highly stratified oceans like the GoM to avoid overestimation.

1.4 Regional Importance of Ocean Mixing

The GoM is a marginal sea of the Atlantic Ocean. The oceanographic system of the GoM is highly dominated by the LC and LCEs (Fig. 1.3) (Schmitz Jr et al., 2005; DiMarco et al., 2005). The LC enters the GoM through the Yucatan Channel, transporting ≈ 25 Sv of warm, salty Caribbean water (Merrell Jr and Morrison, 1981; Hamilton et al., 2005; Meunier et al., 2018). The decay LCEs under strong interaction with other existing mesoscale features and the near-slope topography (Vidal et al., 1992; Lipphardt et al., 2008) diffuse the large amounts of heat and salt contributing to the characteristics of the Common Gulf Water (CGW) (Meunier et al., 2018; Sosa-Gutiérrez et al., 2020).

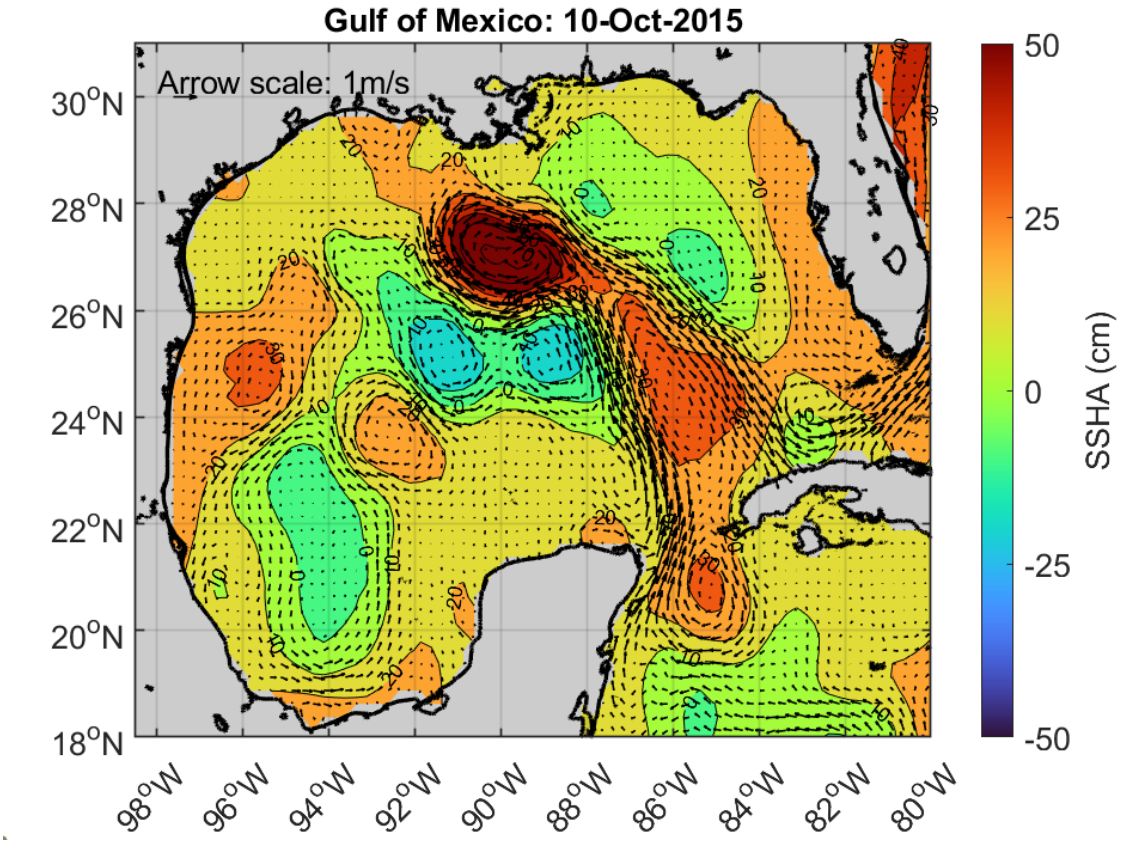

Figure 1.3: Loop Current and Loop Current eddy in the Gulf of Mexico over plotted with Sea Surface Height Anomaly (SSHA) and surface current. Sea Surface Height Anomaly (SSHA) and surface current data is provided by NOAA CoastWatch/ OceanWatch.

The four main water masses found in the GoM are 1) Gulf Common Water (GCW; ≈ 36.4, ≈ 22°C) in above 200 m, 2) Subtropical Underwater (SUW; >36.5, ≈ 23°C) in between 200 and 300 m, 3) Tropical Atlantic Central Water (TACW; ≈ 35.2, ≈ 10°C) in between 300 and 600 m, and 4) Antarctic Intermediate Water (AAIW; ≈ 34.9, ≈ 6°C) (Fig. 1.4) (Sosa-Gutiérrez et al., 2020). The superposition of warm-salty Subtropical Underwater over cold-fresh Antarctic Intermediate Water provides the necessary conditions to drive salt finger convection. A similar water mass is found in the tropical North Atlantic east of Barbados, where strong thermohaline staircase structures are observed between the Subtropical Underwater and the Antarctic Intermediate Water (Schmitt, 1987). Several studies reported the favorable condition of double-diffusion instability in the GoM

(Meunier et al., 2019; Molodtsov et al., 2020).

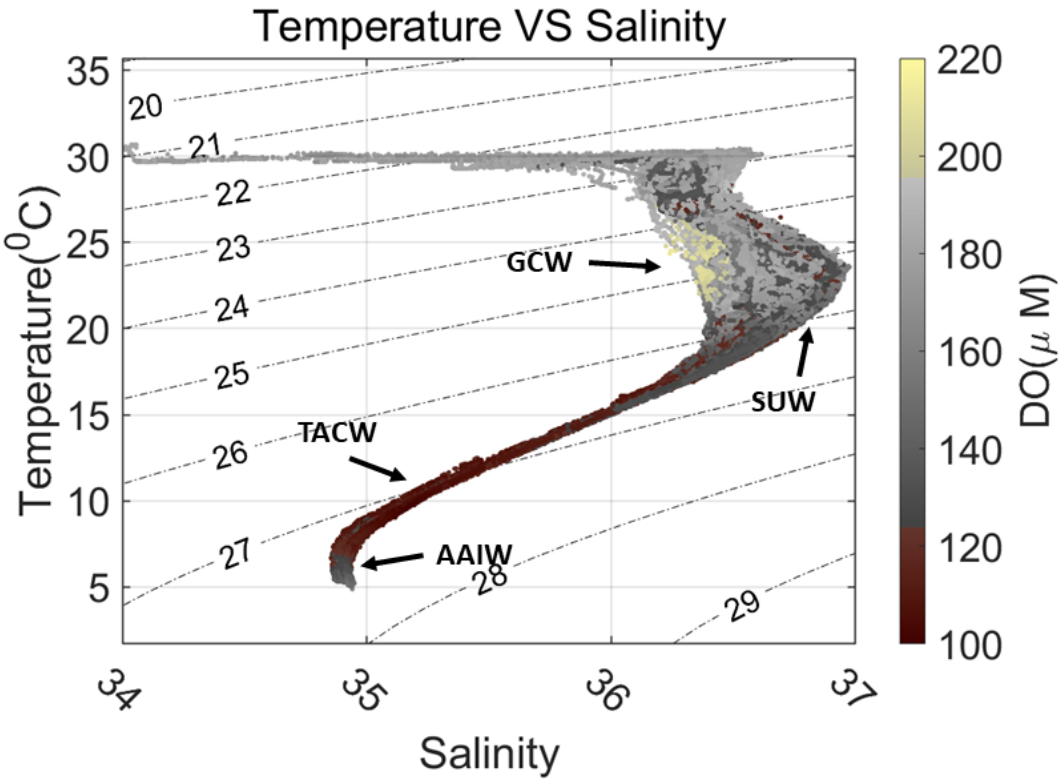

Figure 1.4: Temperature vs. Salinity diagram color plotted with the dissolve oxygen concentration of the upper 1000 m of the Gulf of Mexico.

Understanding the dynamics of LC and LCEs is crucial for the Gulf coast economy. The LC and LCEs directly impact offshore safety, oil spill response, the fishing industry, and tourism. The surface current speed of the LC and LCEs can reach up to 2 m s^{-1} (Koch et al., 1991; National Academies of Sciences, Engineering, and Medicine and others, 2018). The position and intensity of LC directly affect the oil and gas production; current speeds over 2 knots (1 m s^{-1}) can potentially shut down offshore drilling and oil production. LCEs are also a significant contributor to the nutrient supply to the euphotic zone (Chen et al., 2020), which is critical to maintaining the living resources Gulf. Mesoscale variability affects the surface ocean properties, oceanic heat advection,

and air-sea heat fluxes (Putrasahan et al., 2017; Pezzi et al., 2021). It also influences North American climate extremes (Jung and Kirtman, 2016) and hurricane intensifications in the GoM (Shay et al., 2000; Jacob and Shay, 2003; Jaimes et al., 2015; Spencer et al., 2016).

Regional observations suggest a high degree of spatial variability of ocean mixing in GoM. Multiple studies suggest the turbulent diffusivity on the continental slope is about 20 times higher than the GoM interior (Ledwell et al., 2016; Wang et al., 2016). GoM is a well-known region for intense mesoscale and sub-mesoscale eddy activities. Diapycnal and isopycnal mixing within eddies play an essential role in transporting the mass, heat, and nutrients between the ocean surface and the interior (Baird and Ridgway, 2012; Mukherjee et al., 2016; Liang et al., 2017; Chen et al., 2020). Microstructure study of LCEs in GoM (Mitchell et al., 2007; Molodtsov et al., 2020) reported intense turbulent mixing in the eddy core and periphery.

As discussed above, the originally developed LEM requires calibration relative to directly measured turbulence profiles, which limits the application of LEM to the glider missions that have microstructure measurements during the glider survey. In contrast to Beaird et al. (2012), this dissertation propose to calibrate LEM relative to ϵ estimated using Thorpe Scale Method (TM) (Thorpe, 1977), which can be done using glider CTD data. The proposed calibration will allow estimating turbulence from glider data without microstructure measurement.

1.5 Scientific Hypothesis

In contrast to the original calibration method of LEM, which was performed using the microstructure, the new calibration of proportionality constant was performed against the ϵ estimated from TM.

Therefore, my first **Hypothesis (H1)** is: Survey average profile of ϵ using LEM (calibrated with TM) and MicroRider measurements produce statistically consistent estimates of the magnitude and vertical structure of ϵ.

In a density stratified ocean, unstable temperature- or salinity- induced stratification can result in double-diffusion instability. The warm-salty Subtropical Underwater layers above the cold-fresh Antarctic Intermediate Water in the GoM provides the necessary conditions for unstable

stratification due to temperature or salinity.

Therefore, my second **Hypothesis (H2)** is: Double-diffusive instability significantly contributes to the mixing process of the GoM between the Subtropical Underwater and the Antarctic Intermediate Water layer.

1.6 Organization

This dissertation is structured in the following way. Chapter One provides an overview of the motivation of this research and the methodologies associated with microstructure measurement systems, the use of autonomous ocean buoyancy vehicles outfitted with microstructure sensors, and the environmental conditions of the Gulf of Mexico. Chapter 2 present the data sources, the analytical methodologies, and analytical techniques applied in this research. Chapter 3 focuses on the calibration and validation of oceanic vertical velocity using the LEM and TS methods. Chapter 4 addresses the application of the methodology developed in Chapter 3 to glider datasets collected in the deep Gulf of Mexico. These two long missions (90+ days) experienced a variety of oceanographic conditions (including Loop Current and Loop Current Eddy interior, frontal region, and outside eddies) to provide estimates of dissipation rate, Turner angle, characterization of mixing process (salt fingering, thermohaline staircases, mixing efficeience) and assessment of the vertical structure and relative contributions of those process as a function of depth and proximity to oceanographic fronts. Chapter 5 is a summary of findings and a look toward future work.

2. DATA AND METHOD

2.1 Data

The proposed research will use data from four different Slocum glider missions surveyed in the northwestern between 2015 and 2018. The details of the missions and data are given below. Table 2.1 summarizes the four glider data sets used in this dissertation.

Table 2.1: List of the glider survey, sensor and data used to achieve the research goals.

Data	Reffed name	Survey period	No. of days	No. of profiles	Sensor	
					Finescale	Micrstructure
Glider Data I	M18	05/09/2018 - 06/22/2018	35	224 (FS[1]) 146 (MS[2])	CTD[3] OF[4] CDOM[5]	MicroRider
Glider Data II	M16	11/02/2016 - 11/11/2016	8	104 (FS[1]) 10 (MS[2])	CTD[3] OF[4]	MicroRider
Glider Data III	M15a	08/05/2015 - 10/12/2015	67	495 (FS[1])	CTD[3] OF[4] CDOM[5]	
	M15b	08/22/2015 - 11/102015	79	353 (FS[1])	CTD[3] OF[4] CDOM[5]	

[1]Finescale, [2]Microstructure, [3]Conductivity - temperature - depth, [4]Optical - fluorescence, [5]Colored dissolved organic matter

2.1.1 Glider Data I

Glider "Sverdrup" S/N - 541 was deployed in the GoM (Fig. 2.1) on May 9, 2018, as part of the Gulf of Mexico Mixing (GoMix) experiment. When refering to this glider data, it will be referred to a M18. The black line in Fig. 2.1 is showing the glider track and the red dot showing the glider deployment location ($27°51.866'$ N $93°34.916'$ W) and the colormap represent the sea surface height anomaly (SSHA) on May 20, 2018. During that mission, M18 completed multiple transects over the continental slope of GoM. The primary objectives of this glider deployment were to profile LCEs fronts with the MicroRider, characterize the impact of oceanographic and atmospheric weather fronts (as available during the mission), and to profile the entire water-column on and off the Texas- Louisiana shelf.

During M18, the glider was equipped with finescale sensors conductivity - temperature - depth (CTD), colored dissolved organic matter (CDOM), and optical fluorescence which measures chlorophyll and dissolved oxygen. The finescale sensors sample at a rate of 0.5 Hz. Additionally the glider also has flight controlling sensors which a number of flight parameters including pitch, displacement of the buoyancy engine etc. M18 had a total of 224 dives and collected scientific data for 35 days. M18 completed multiple transect over the continental slope of GoM and did periods of shallow and deep dives ($\approx\ 1000\,m$).

In order to measure ocean microstructure, M18 was equipped with a MicroRider. The MicroRider is an ocean microstructure measurement instrument by Rockland Scientific International Inc (Canada). The MicroRider was equipped with five microstructure probes, including two fast-response thermistors, one micro- conductivity probe, and two velocity shear probes. The MicroRider sample at a rate of 512 Hz. During M18, the MicroRider collected a total of 146 microstructure profiles.

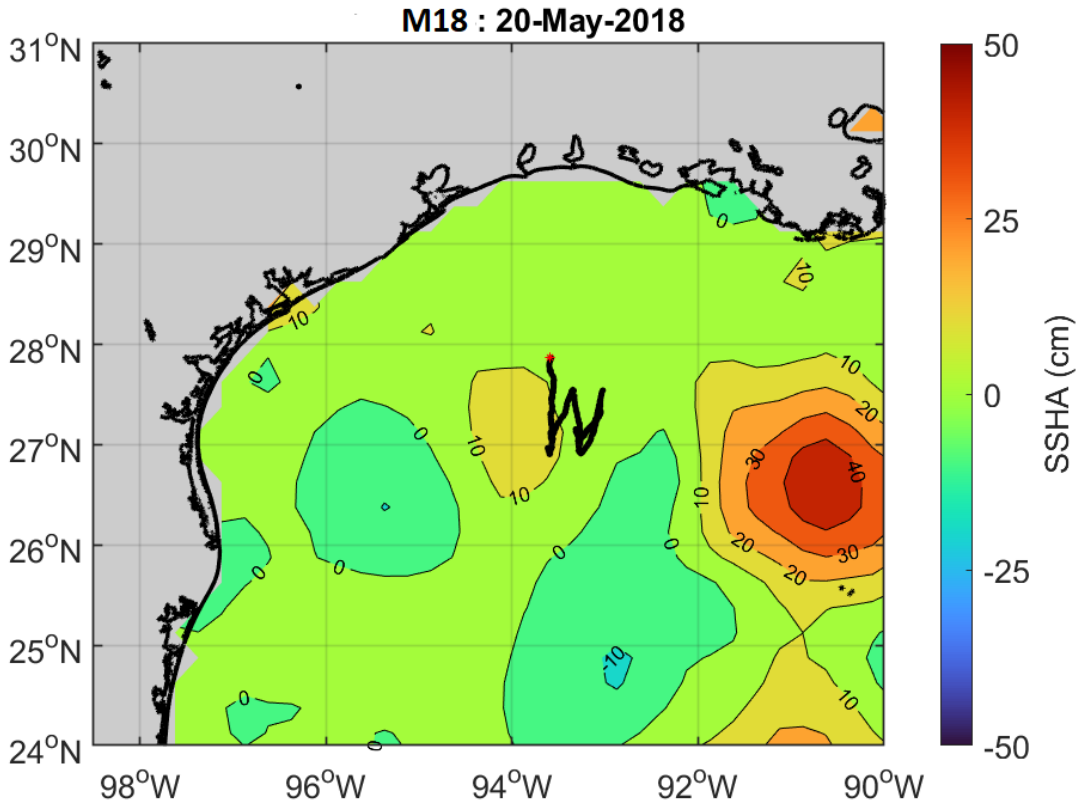

Figure 2.1: Mission track of Glider “Sverdrup” (black), M18, in the Northwestern Gulf of Mexico deployed on May 9, 2018. The starting point of the track is marked by the red dot. The colormap represent the Sea Surface Height Anomaly (SSHA) on May 20, 2018, of the glider survey area. Sea Surface Height Anomaly (SSHA) provided by NOAA CoastWatch/OceanWatch.

2.1.2 Glider Data II

A Slocum G2 Glider "Howdy" S/N - 308, referred to as M16, was deployed in the western Mississippi Canyon (Fig. 2.2) on September 2, 2016, also as part of the GoMRI-funded GoMix experiment to quantify the horizontal and vertical structure of turbulence at the edge of the continental slope of the northern GoM. The track of the glider are represented by the black line in Fig. 2.2 and the red dot identifying the glider deployment location ($27°53.955'$ N $93°35.381'$ W). The colormap represent the SSHA of glider survey area on September 6, 2016. The SSHA is is highley influency by the presence of the LCE identified by the high SSHA (Red color). However, the glider didn’t encounters the LCE during that survey.

M16 was equipped with CTD, turbidity, CDOM, and optical fluorescence. M16 has a total of 104 dives and has a mixture of shallow and deep dives. Shallow dives when over the continental shelf and slope; deep dives ($\approx$ $1000\,m$) when seaward of continental shelf and slope.

M16 also carried a MicroRider. The configuration of the MicroRider is as described in subsection 2.1.1. The MicroRider collected data for 10 complete dives, before failure due to saltwater leakage in the electronics compartment.

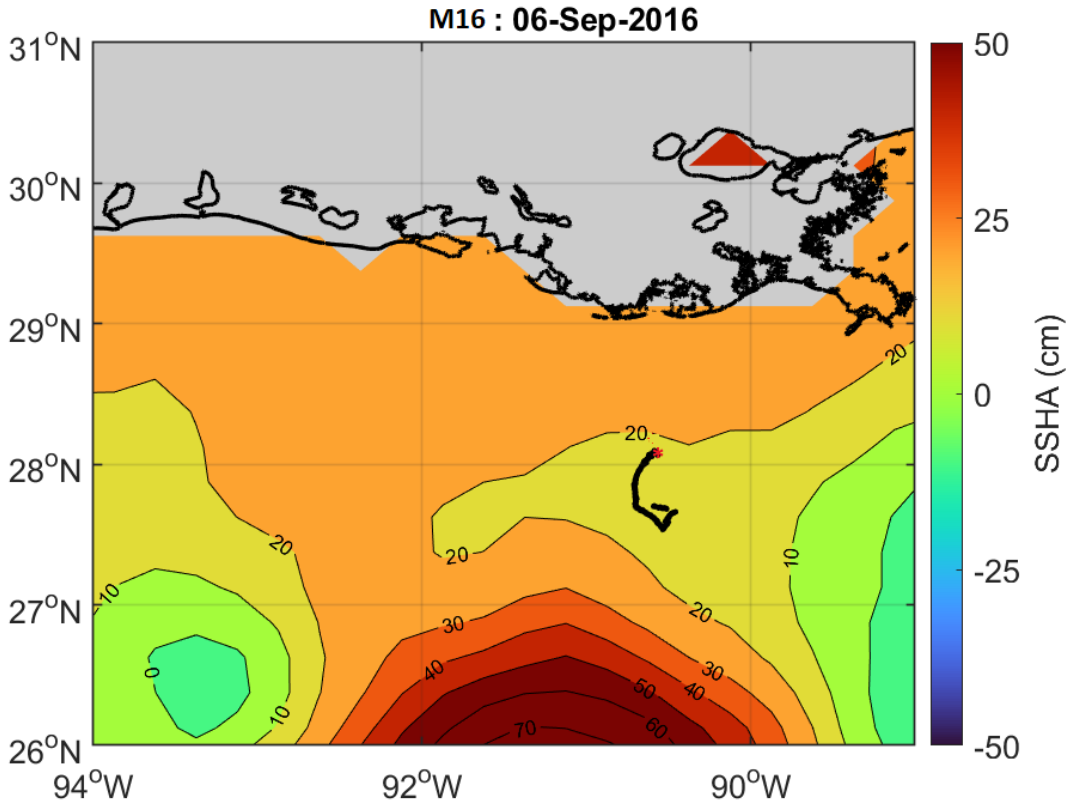

Figure 2.2: Mission track of Glider "Howdy" (black), M16, in the Northwestern Gulf of Mexico deployed in September 2, 2016. The starting point of the track is marked by the red dot. The colormap represent the Sea Surface Height Anomaly (SSHA) in September 2, 2016 of the glider survey area. Sea Surface Height Anomaly (SSHA) provided by NOAA CoastWatch/OceanWatch.

2.1.3 Glider Data III

Two Slocum G2 Glider "Stommel" S/N - 540, M15a, and “Sverdrup” S/N - 541, M15b, were deployed in the northwestern GoM (Fig. 2.3) on August 5 and August 22, 2015, respectively, as a part of the Gulf of Mexico Integrated Spill Response Consortium (GISR) project. The track of the glider M15a and M15b are represented in Fig. 2.2 by the by the black and red line, respectively. The colormap represent the SSHA of glider survey area on October 10, 2015. During the mission, both gliders transited multiple current features including Loop Current (LC) extension and an anticyclonic Loop Current Eddy (LCE).

M15a entered in the LCE on August 28, 2015, and sampled for $\approx$ 10 days. On August 28, 2015 the center of the LCE was in 27.5° N 94° W, where Fig. 2.2 shows the center of the LCE on October 10, 2015 is located around (25° N 94° W). The actual location of the LCE during glider survey are shown in chapter - 4 Fig. 4.2. The total survey duration of M15a was 67 days and completed 495 dives.

M15b entered the LC on September 11, 2015, and sampled for $\approx$ 35 days. The center of the LC can be identified by SSHA >+50, located around 27° N 90° W (Fig. 2.2). M15b surveyed total 79 days around the LC and LC periphery and completed 353 dives.

Both glider were equipped with CTD, CDOM, and optical fluorescence. The gliders sampled the water column from 0 to 1000 m depth at a rate of 0.5 Hz and were configured to sample only during descent (i.e., the science sensors were turned off during ascent).

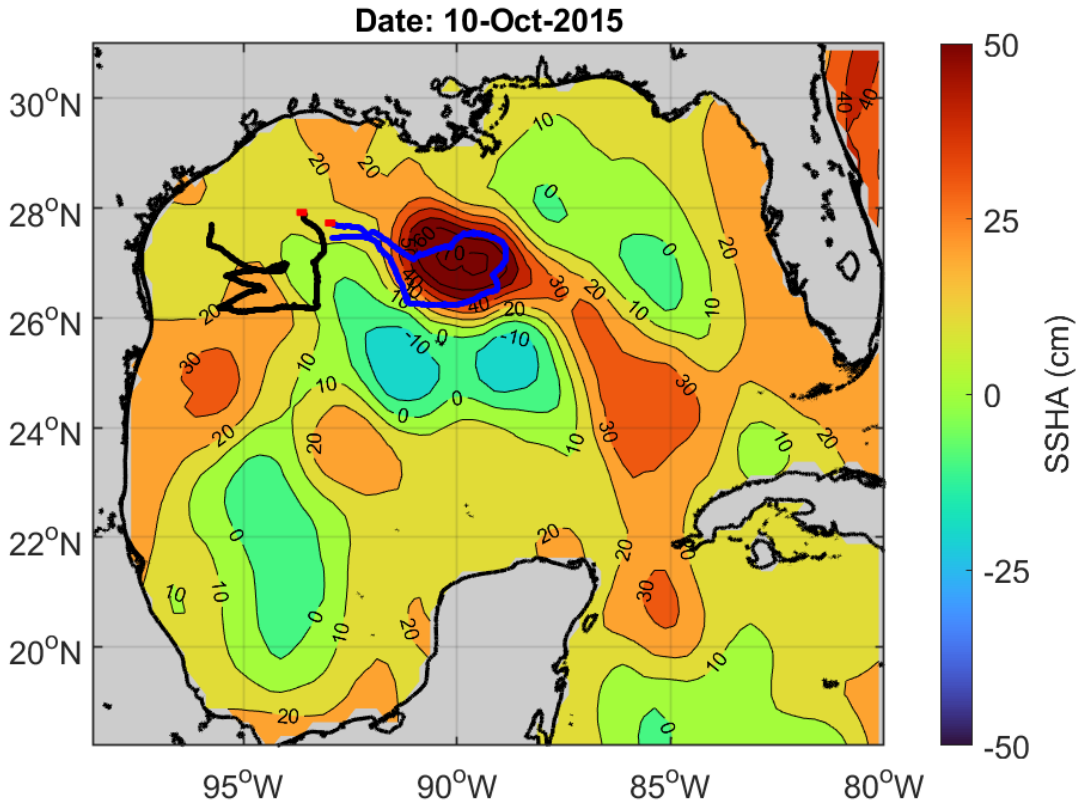

Figure 2.3: Tracks of glider "Stommel", M15a, (black) and Glider "Sverdrup", M15b, (blue) in the Northwestern Gulf of Mexico between August 5 to November 5. The colormap represent the Sea Surface Height Anomaly (SSHA) in October 10, 2015. Location of the LCE and LC extension surveyed by the glider M15a and M15b can be identified fron the positive SSHA $> +30$ and $> +50$, respectievely. Sea Surface Height Anomaly (SSHA) provided by NOAA CoastWatch/OceanWatch.

2.1.4 Altimetry Data

Altimetry derive data were used in this research are Sea Surface Height Anomaly (SSHA) and geostrophic current. Altimetry data are provided by the NOAA Laboratory for Satellite Altimetry (NOAA, 2018). https://coastwatch.noaa.gov/

2.2 Method

2.2.1 The Large Eddie Method (LEM)

Beaird et al. (2012) first applied the LEM to estimate TKE dissipation rates (ϵ) using the data collected by a Seaglider ocean buoyancy vehicle (Eriksen et al., 2001). A similar methodology was used in several other studies of turbulence (Moum, 1996; D'Asaro and Lien, 2000a,b; Evans et al., 2018) to estimate the turbulence from the vertical velocity spectrum at frequencies larger than the bulk buoyancy frequency. LEM estimates ϵ as a function of buoyancy frequency (N) and turbulent velocity scale (q') as

$$e = c_\epsilon N (q')^2 \tag{2.1}$$

where, c_ϵ is a proportionality constant. The buoyancy frequency, N, is calculated

$$N = \sqrt{-\frac{g}{\rho_0}\frac{\delta\rho}{\delta z}} \tag{2.2}$$

where, z is the depth calculated from the glider SBE CTD pressure data and g = 9.8 m s^{-2} is the gravitational acceleration.

To estimate q', Beaird et al. (2012) filter the vertical velocity (w) profiles with a highpass filter with a fixed 30-m cutoff wavelength. The applied filter removes low-frequency internal wave variability but fails when the stratification is more variable and strong (Evans et al., 2018). In contrast to Beaird et al. (2012), for this study the mean and trend from the vertical velocity profiles were removed. Then, the vertical velocity (w) profiles were treated in two different segments based on the buoyancy frequency at the bottom of the maximum salinity layer. For simplicity, $N = 0.012\ s^{-1}$ were used as the buoyancy frequency of the bottom of the maximum salinity layer (Fig. 3.8d). When in the strongly stratified maximum salinity layer, the vertical velocity data are first filtered with a low-pass filter with a cutoff frequency of 0.020 s^{-1} (N maximum) and then high-pass filtered with a 15 m cutoff wavelength. When below the maximum salinity layer, the vertical velocity data is first filtered with a low-pass filter with a cutoff frequency of 0.020 s^{-1}

and then with a high-pass filter with a cutoff wavelength of 200 m. Finally, the root mean square (RMS) of filtered vertical velocity profiles over a moving 10-m window is chosen as q'. Table 2.2 summarizes the filters applied for q' estimation.

Table 2.2: Filter classification for q' estimation.

Buoyancy frequency (N)	Filter cut-off	
	Low-pass	High-pass
$N >$ 0.012 s^{-1}	0.02 s^{-1}	Frequency equivalent to 15 m wavelength
$N <$ 0.012 s^{-1}	0.02 s^{-1}	Frequency equivalent to 200 m wavelength

2.2.2 Estimation of the Vertical Velocity of Water

The vertical velocity of water (w) is the velocity of the ocean fluid in the upwards or downwards direction. The vertical velocity may be estimated from the difference between the absolute vertical speed of the glider in water (w_p) and the modeled platform-based vertical speed (w_g) of the glider (in an idealized ocean at rest) as:

$$w = w_p - w_g \tag{2.3}$$

(Merckelbach et al., 2010; Frajka-Williams et al., 2011). This presumes that multiple properties and characteristics of the glider aerodynamic qualities are known or inferred.

The absolute vertical speed of the glider is calculated as the pressure rate as

$$w_p = \frac{dz}{dt} \tag{2.4}$$

where z is the depth of the glider calculated from pressure (P). Following Merckelbach et al. (2010), a schematized glider flight in the vertical direction with acting forces is shown in Fig. 2.4. The glider path and axis is represented by the solid and dashed black arrow marked by y' and the y, respectively. The angle between the horizontal x and glider axis is called the pitch (θ) and angel between glider axis and glider path is called the angle of attack (α). The glider glide angle(γ) is the sum of pitch (θ) and angle of attack (α). Four small black arrow represent the four forces due to buoyancy (F_B), gravity (F_g), lift (F_L), and drag (F_D) acting on the glider centre of mass at any given time during the glider flight.

The force balance equation of a glider moving through still water can be written as,

$$F_B - F_g - \frac{1}{2}\rho S U^2 [C_{D_0} + (C_{D_{1,w}} + C_{D_{1,h}})\alpha^2] \times \frac{\sin^2(\gamma) + \cos^2(\gamma)}{\sin(\gamma)} = 0 \tag{2.5}$$

where, ρ is the in-situ density of water, s is the area of the wings, α angle of attack, θ in the pitch angle, $\gamma = \theta + \alpha$ is the glide angle, C_{D_0} parasite drag, $C_{D_{1,w}}$ and $C_{D_{1,h}}$ are the drag induced by the glider wings and hull respectively and U is the glider velocity along glide axis. For this research, the updated drag and lift parameter for the glider wings and hull is adopted from Merckelbach et al. (2019), which were updated against a Doppler velocity log (DVL) measurement.

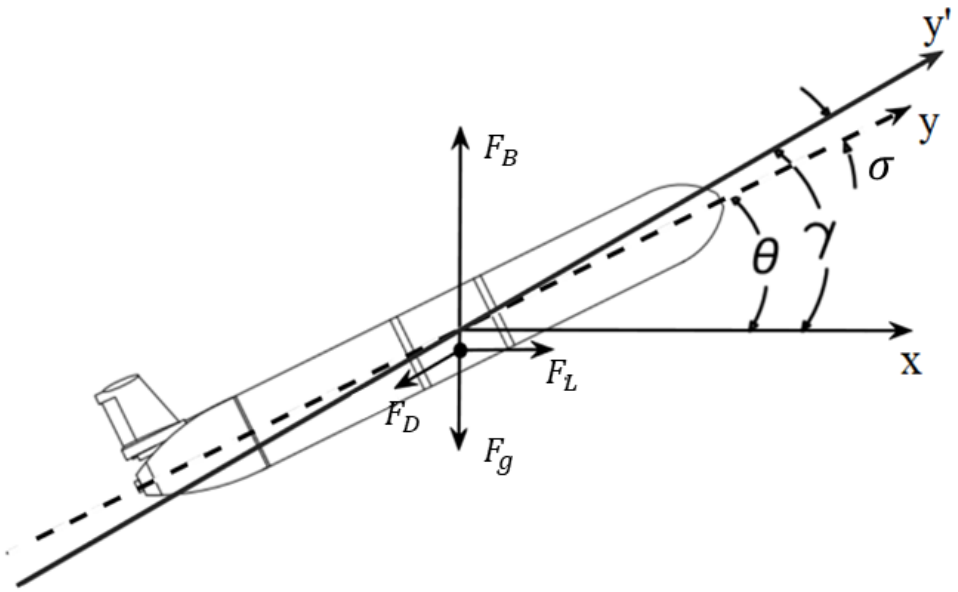

Figure 2.4: A schematic representation of the glider flight in the vertical direction, where γ is the glide angle, θ is the pitch, and α is the angle of attack. Four forces acting on the glider are buoyancy F_B, gravity F_g, lift F_L, and drag F_D.

The gravitational force acting on the glider is given by,

$$F_g = m_g g \tag{2.6}$$

where m_g is the mass of the glider, and g is the gravitational acceleration. The buoyancy force acting on the glider,

$$F_B = g\rho\{V_g[1 - \epsilon P + \alpha_T(\Delta T)] + \Delta V_{bp}\} \tag{2.7}$$

where V_g is the volume of glider at atmospheric pressure, ϵ is the compressibility of the hull, P is the water pressure, α_T is the thermal expansion coefficient, ΔT temperature gradient, and ΔV_{bp} the buoyancy change resulting from the buoyancy engine.

Finally, the vertical velocity of the glider is given by,

$$w_g = U \sin(\gamma) \tag{2.8}$$

where, U is the glider velocity along glide axis and γ is the glide angle.

The science and mission sensors of the glider record most parameters were used in the glider flight model. C_{D_0}, ϵ, and V_g are optimized using a nonlinear least-squares optimization relative absolute vertical speed w_p.

2.2.3 Thorpe Scale Method (TM)

TM (Thorpe, 1977; Galbraith and Kelley, 1996; Ferron et al., 1998; Gargett and Garner, 2008; Howatt et al., 2021) offers a CTD-based method to estimate small-scale mixing in the water column where density overturning takes place. The energy dissipation rate for each individual overturn is given by

$$\epsilon = 0.64 L_{Th}^2 \langle N \rangle^3 \tag{2.9}$$

where the Thorpe-scale L_{Th} of an overturning eddy is defined as

$$L_{Th} = \sqrt{\langle d'^2 \rangle} \tag{2.10}$$

where, d' is the Thorpe displacement. Thorpe displacement (d') is obtain from the difference of actual and density sorted depths over each turbulent patch.

There are several challenges involve in applying TM in the glider data. Gliders move the water at an angle compared to a complete vertical path, leading to errors in the measurements of Thorpe displacement and overturns (Smyth and Thorpe, 2012; Thorpe, 2012) resulting underestimation of ϵ. Glider base TM method reportedly overestimate ϵ when turbulence is week (Howatt et al., 2021). The sampling resolution of the CTD is the main constrain of overturning detection for TM analysis (Galbraith and Kelley, 1996).

To apply the TM, data were filtered with a low-pass with filter SeaBird Data Processing Manual. The filter runs forward and then back through the data to eliminate any delays caused by the filter. The time constant for the filter was chosen to be 2 seconds which is four times the sampling frequency. The filter smoothes high-frequency data and removes unwanted spikes. Finally, a manual inspection was conducted to ensure the quality of the data. To detect overturn, the glider

data were checked and processed using the criteria described in Galbraith and Kelley (1996). The sampling theorem required the length of the overturns at least twice the density resolution of the instrument. For this calculation, the minimum resolvable overturn length was set to 1 m; which is governed by the sampling frequency of the CTD is 0.5 Hz and the vertical resolution of the data 0.2– 0.24 m. The density resolution imposes another restriction on overturning detection; and the minimum overturning length was set using $L_\rho = 2\frac{g}{N^2}\frac{\delta\rho}{\rho}$, where $\delta\rho = \rho - \rho_{sorted}$. We used the density noise level as $1 \times 10^{-4} kgm^{-3}$ (Howatt et al., 2021) to calculate the minimum overturning length. The density noise level was set to two times the minimum value for $\delta\rho$. Finally, the overturn ratio, as suggested by Gargett and Garner (2008), was calculated as $R_0 = min(\frac{L^+}{L}, \frac{L^-}{L})$, where L is the overturning length, L^+ and L^-, are the lengths of that portion of L where the Thorpe displacements are positive and negative, respectively. R_0 values less than 0.2 is attributed as overturns caused by a single density spike attributable to instrumental noise and therefore not indicative of the physical environment and thus discarded from further analysis as a false overturn (Gargett and Garner, 2008).

2.2.4 Calibration of LEM

The smallest scale of turbulent flows is determined by the Kolmogorov scale $\eta = (\frac{\nu^3}{\epsilon})^{1/4}$, where ν is the kinematic viscosity and ϵ is the kinetic energy dissipation rate (Moum, 1996). In the ocean, η is in the order of $10^{-3}m$, which is smaller than the measuring capacity of a standard glider sensor. Therefore, the turbulence equation needs to scale to estimate turbulence dissipation using LEM. The scaling is done assuming the turbulence is isotropic and the kinetic energy of the largest scales of turbulent motions dissipates to the viscous scale (Moum, 1996). In this research, the proportionality constant c_ϵ of LEM will be estimated relative to the ϵ estimated from the TM.

Survey average profiles of ϵ_{LEM} from LEM using equation (2.1) and ϵ_{TH} from TM using equation (2.9) were used to calibrate the proportionality constant. Survey average profiles were constructed by averaging data point for the entire mission over 10 meters depth bin (Fig. 3.8a). Finally, a linear least-squares fit between the survey averaged ϵ_{LEM} and ϵ_{TH} is applied to estimate c_ϵ.

2.2.5 MicroRider data processing

The MicroRider has five probes: two velocity shear probes (one for each ordinal direction u,v), two redundant termperature probes, and one conductivity probes. The MicroRider samples each probe simultaneously at 512 Hz. Prior to analysis the quality and integrity of the MicroRider data were inspected for outliers, non-physical sensor performance, and utility. As indicated in Table 2.1, the number of useful MicroRider profiles for M16 and M18 is 10 and 146, respectively. The shear probe time series from MicroRider is used to calculate ϵ. In isotropic turbulence, the TKE dissipation rates, ϵ, can be estimated by integrating the wavenumber (k) spectrum (Φ) as,

$$\epsilon = \frac{15}{2}\nu\overline{\left(\frac{\partial u_j}{\partial x}\right)^2} = \frac{15}{2}\nu\int_{k_u}^{k_l}\Phi(k)\,dk \tag{2.11}$$

where $j = (1,\, 2)$ are the shear probe number, $\nu \approx 10^{-6}\ m^2\, s^{-3}$ is the kinematic viscosity. The lower (k_l) and upper (k_u) limits of the integral were determined by the by Nasmyth (1970) empirical model for the turbulence spectrum.

We used the ODAS MATLAB® package developed by Rockland Scientific to process the MicroRider data and estimate the TKE dissipation rate ϵ. The dissipation rate is calculated for each $16\,s$ block of data with $50\,\%$ overlap with a fast Fourier transform (FFT) of $4\,s$ (this is standard processing of the microRider and is detailed in the Fer et al. (2014) and Wang et al. (2018)). Finally, the TKE dissipation rate is calculated as the geometric mean from both shear probes. Data near the top or bottom of the profiles were excluded due to the contamination at turning depth (i.e., the depths in which the glider vehicle is actively changing orientation from ascent to descent and vice versa. Anomalous spikes were identified and removed before calculating the turbulent dissipation rate.

3. QUANTITATIVE ASSESSMENT OF THE PERFORMANCE OF GLIDER BASED TURBULENCE ESTIMATION RELATIVE TO MICROSTRUCTURE MEASUREMENT

3.1 Introduction

Two gliders (M16 and M18) surveyed the northwestern GoM between 2016 and 2018. During that deployment, both gliders were equipped with finescale hydrographic sensors CTD, dissolved oxygen, fluorescence, and MicroRider. M18 has 224 finescale and 146 microstructure measurements. In addition, M16 has 104 finescale and only 10 microstructure measurements (MicroRider turned off due to saltwater leakage). The details of the M16 and M18 surveys and the sensor details are given in Table: 2.1. In this chapter, the glider-based estimation of TEK dissipation rates (ϵ) (outlined in chapter 2) will be applied to the finescale hydrographic data of M18, and the accuracy of the estimation will be statistically compared and quantified relative to the turbulence measured by the MicroRider carried by glider. In addition, glider-based turbulence estimation will be applied to the M16 data to construct the turbulence structure for the entire mission.

3.2 Hydrographic Condition

Temperature (T), salinity (S), and density (ρ) sections obtained during the glider mission are represented in Fig.3.1 to Fig. 3.3 for the depth between $20 \breve{} 1000\,m$. Temperature data shows the presence of a thick thermocline until $\approx$ 700 m depth with maximum temperature observed at surface $\approx\ 27.5°C$ and gradually decreased to $\approx\ 5°C$ with depth.

The salinity plot shows the high salinity in the upper $\approx\ 300\,m$, gradually decreasing with depth. Most water mass with salinity < 36.4 in the mixed layer and upper thermocline can be characterized as Gulf Common Water (Wang et al., 2016) (Fig. 3.2). The low salinity near the surface suggests the influence of Mississippi River plume water in the study region during summer (Fig. 3.5) (Wang et al., 2016; Hamilton et al., 2018), which is only detected at the beginning of the glider survey. High salinity water mass with salinity > 36.5 shows the presence of SUW residual in the upper thermocline between the depth of $100\ -\ 200\,m$ (Fig. 3.2). The presence of SUW is

also visible in the temperature-salinity plot, with maximum values reaching $\approx$ 36.65 (Fig. 3.5). The Tropical Atlantic Central Water (TACW; $\approx 35.2, \approx 10°C$) is found at depths between ≈ 300 and $\approx$ 600 m, and the Antarctic Intermediate Water (AAIW; $\approx 34.9, \approx 6°C$) at depth > $600\,m$ (Morrison et al., 1983; Sosa-Gutiérrez et al., 2020).

The density shows the highly stratified water column of the GoM (Fig. 3.3). The higher salinity controls the density gradient in the near-surface water, and partial compensation of the effects of temperature and salinity is also visible. The Brunt-Väisälä frequency profiles calculated from the CTD shows relatively strong stratification in the water column above 200 m with maximum stratification of $N = 2.8 \times 10^{-2} s^{-1}$ (Fig.3.4).

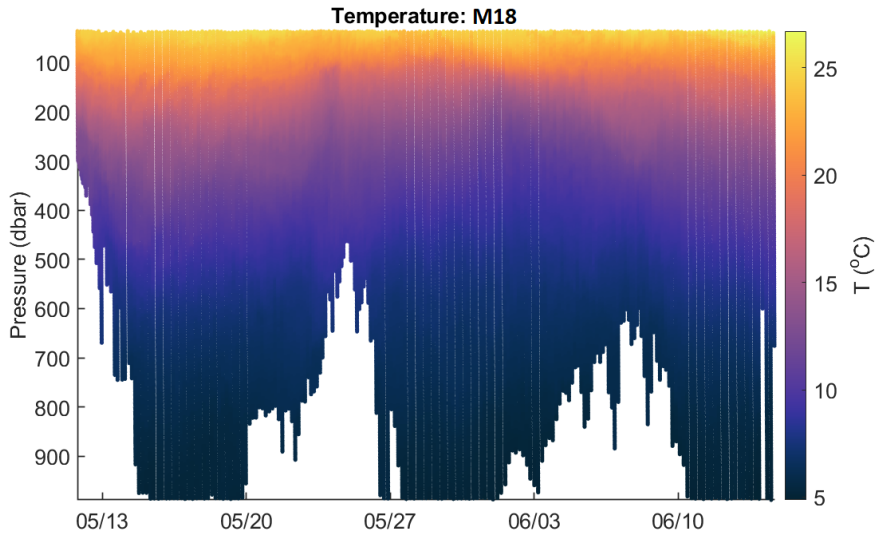

Figure 3.1: Hovmöller plot of temperature as a function of pressure and time form data collected M18 deployed in 2018 in the northwestern Gulf of Mexico.

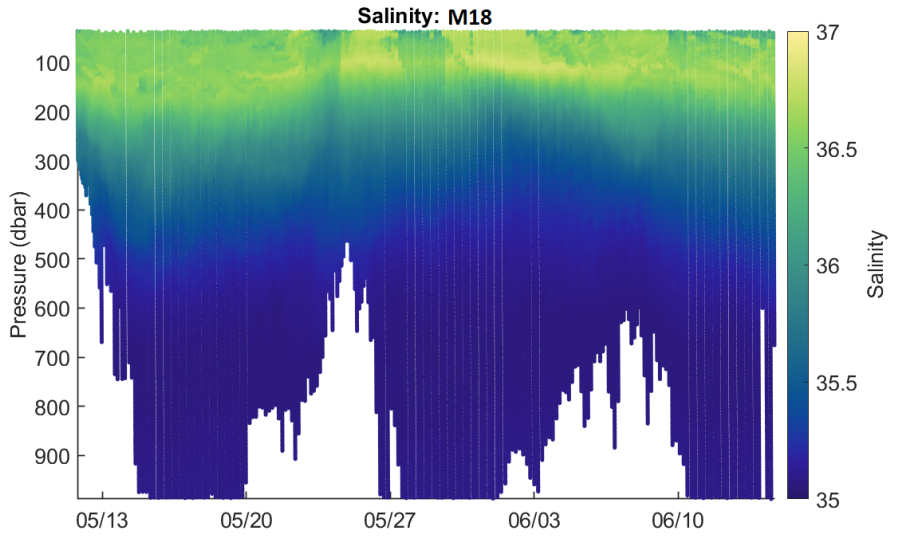

Figure 3.2: Hovmöller plot of salinity as a function of pressure and time form data collected M18 deployed in 2018 in the northwestern Gulf of Mexico.

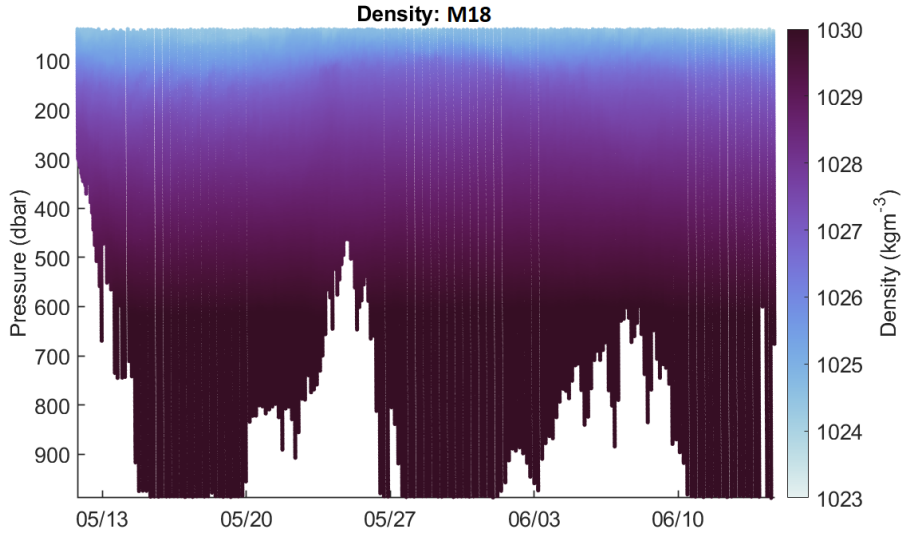

Figure 3.3: Hovmöller plot of density as a function of pressure and time form data collected M18 deployed in 2018 in the northwestern Gulf of Mexico.

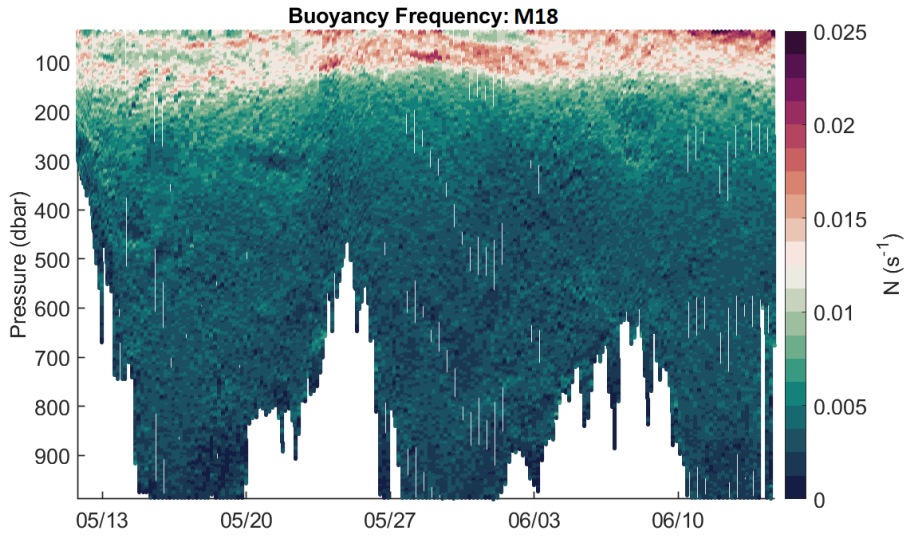

Figure 3.4: Hovmöller plot of Brunt-Väisälä frequency as a function of pressure and time form estimated from data collected by M18 deployed in 2018 in the northwestern Gulf of Mexico.

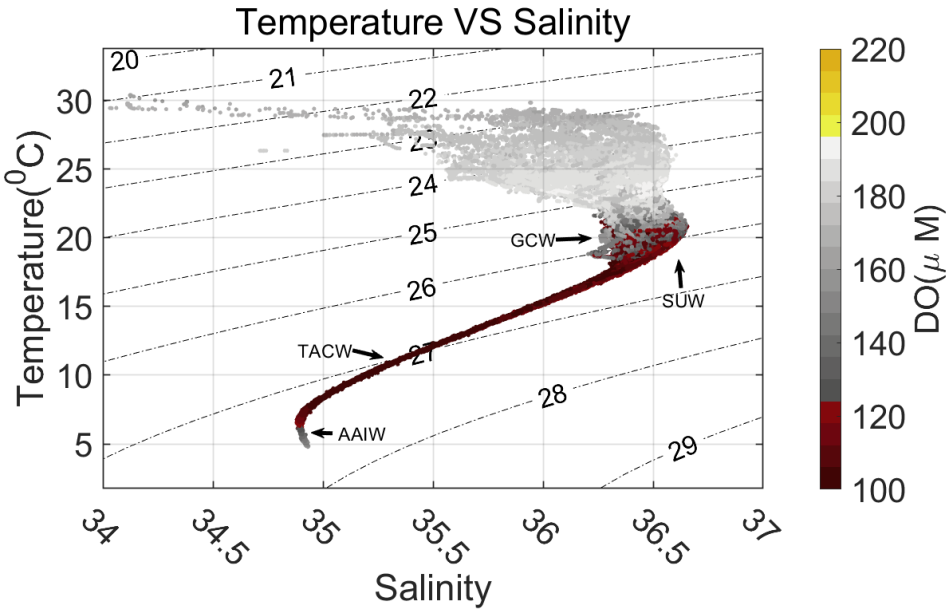

Figure 3.5: The temperature-salinity diagrams are shown for CTD data collected by M18. The black contour lines show the isopycnals in kgm^{-3}. The colors represent dissolved oxygen concentrations.

3.3 Vertical Water Velocity

A single profile of vertical velocities is shown in Fig.3.6. The right panel shows the measured vertical velocity from depth rate w_p (blue) and the modeled optimized velocity w_g (red). The measured and modeled vertical velocity show similar features. The vertical velocity of the glider is higher in shallow depth and decreases with the increase of depth. The glider maintains its flight path by adjusting its pitch angle, which is done by moving the battery pack around the center of mass. The 9 kg battery pack shift appeared as the jump around 400 m in the glider vertical velocity profiles (Fig. 3.6 right panel).

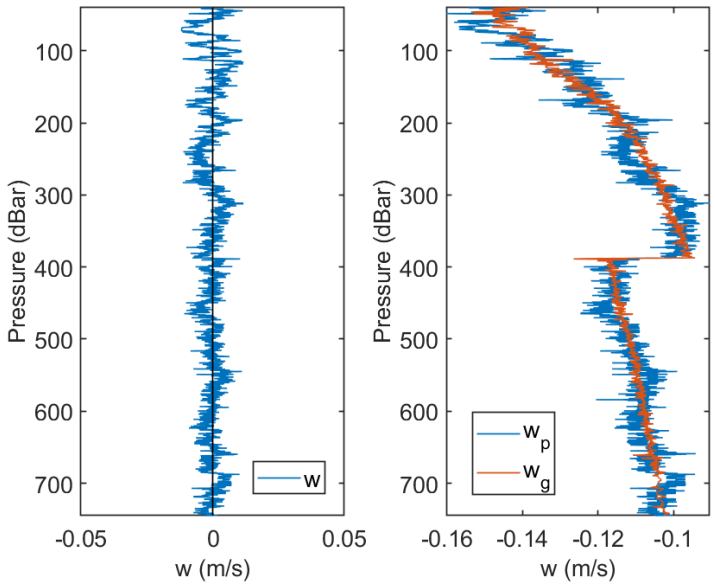

Figure 3.6: Profiles of vertical velocities (a) vertical velocity of water(w) (blue), (b) vertical velocity of glider from depth rate (w_p) (blue) and modeled (w_g) (red).

The left panel shows the vertical water velocity (w) from the difference between the glider velocity from depth rate and the modeled velocity. The internal waves cause the observed fluctuation in the vertical velocity profile (Rudnick et al., 2013). The estimated vertical water velocity doesn't show any spike caused by the pitch battery pack indicating the goodness of the least-square fit

optimization of the glider flight model. The optimized average values for the parasite drag (C_{D0}) is 0.2923, compressibility (ϵ)[1] is $5.5615 \times 10^{-10} Pa^{-1}$, and volume ($V_g$) is 0.0554 m^3.

The Hovmöller diagram of the vertical velocity of the water is shown in Fig.3.7a. The estimated vertical velocity for the entire mission shows a coherent horizontal structure aligned with the isopycnals. The strongest vertical velocity observed between $1026 - 1028\ kg\,m^{-3}$ density pycnocline, under the strong stratification layer (> $N \approx 0.012\,s^{-1}$).The estimated mean vertical velocity of water is $-6.2 \times 10^{-4}\ m\,s^{-1}$. Elevated vertical velocity also observed in near to the seafloor over the continental slope. The histogram is normally distributed around the mean with a maximum velocity is about $0.02\ m\,s^{-1}$ Fig. 3.7b, and RMS vertical velocity is $0.0048\ m\,s^{-1}$. The estimated vertical velocity is consistent with the findings of moored ADCP measurement in the GoM (Rivas et al., 2008). The estimated noise variance suggests the error associated with the estimated vertical water velocity is $0.002\ m\,s^{-1}$.

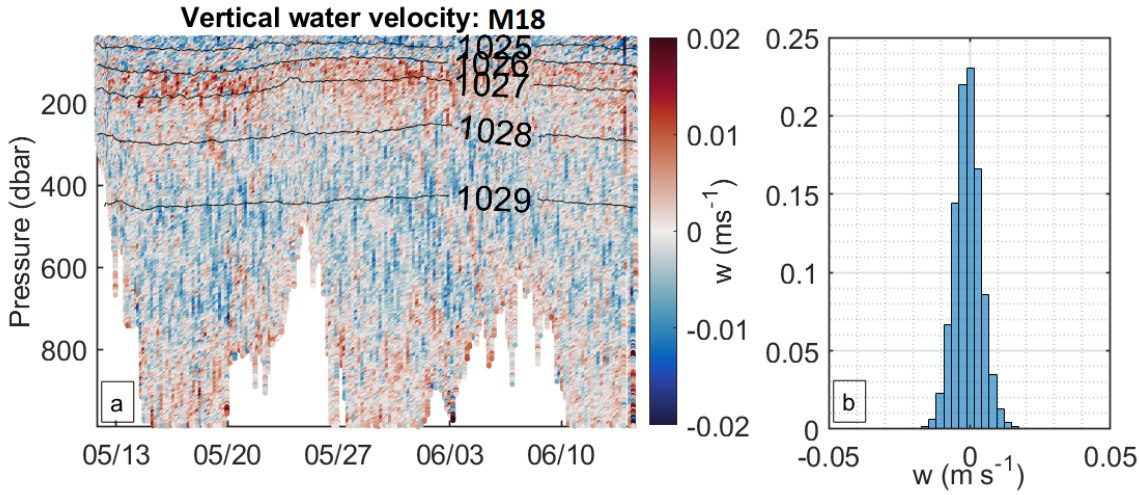

Figure 3.7: (a) Hovmöller plot of estimated vertical current velocity as a function of pressure and time form data collected by M18 deployed in 2018 in the northwestern Gulf of Mexico. The black lines represent the density contour. (b) Histograms of recorded vertical water velocities for the entire mission.

[1]Note: The letter ϵ here represent compressibility, not to confused with TKE dissipation rate discussed in turbulence estimation.

3.4 Comparison

To evaluate the performance of LEM calibrated with TM, a comparison between the TM-inferred TKE dissipation rates (ϵ_{TM}), LEM (calibrated with TM) estimated TKE dissipation rates (ϵ_{LEM}) and the MicroRider measured TKE dissipation rate ($\epsilon_{\mu R}$) is attempted. Due to the intermittent nature of turbulence, inherent variability in the GoM, and the difference between the glider and MicroRider sensor capability, comparisons are made using survey-averaged profiles, bin-averaged profiles, and probability distribution functions. Moreover, mean vertical profiles of mixing parameters of turbulent mixing are desired for large-scale ocean circulation models (Melet et al., 2013). The survey averaged profiles are created by averaging the data for the entire mission over 10-meter depth bins. The bin-averaged profiles are created by averaging the data of individual profiles over 10-meter depth bins.

3.4.1 Survey averaged profile

The linear least-squares fit between the survey-averaged profile using Eq. 2.1 and ϵ_{TH} produced the proportionality constant c_ϵ = 0.58. The survey-average profiles for ϵ_{LEM} (cyan) along with ϵ_{TM} (red) and $\epsilon_{\mu R}$(black) are shown in the Fig. 3.8a. The calibrated value for c_ϵ relative to ϵ_{TM} is broadly consistent with the reported value of c_ϵ = 0.37 in Beaird et al. (2012) and c_ϵ 1.96 ± 0.2 in Evans et al. (2018) calibrated against vertical microstructure profile and ADCP derived TKE dissipation rates, respectively.

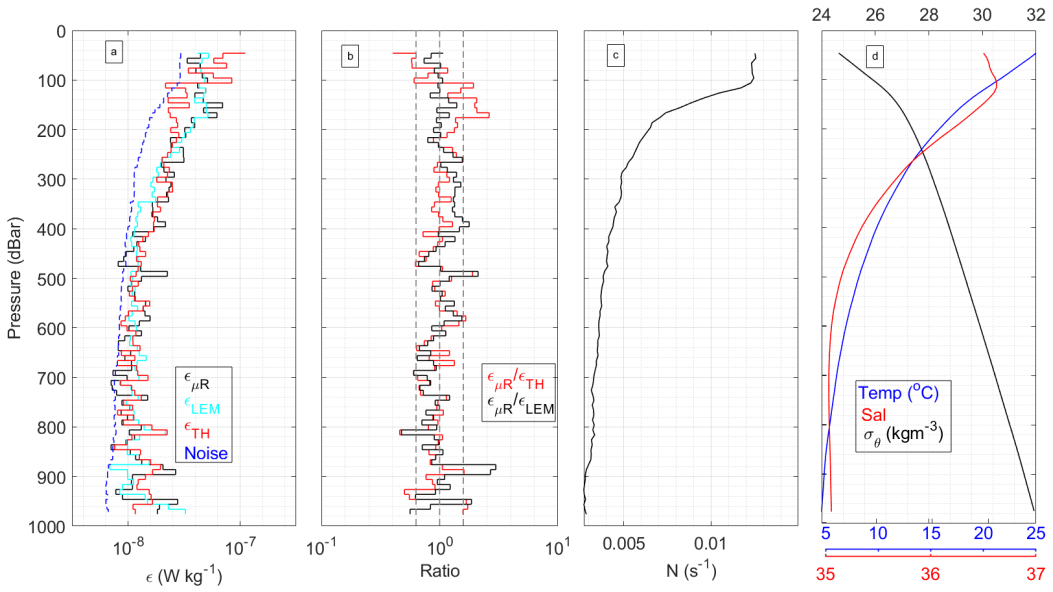

Figure 3.8: Survey averaged profiles(a) MicroRider $\epsilon_{\mu R}$(black), TH ϵ_{TH} (red), LEM ϵ_{LEM} (cyan), and noise level/lowest detection level of LEM (blue), (b) ratio of MicroRider to TH and MicroRider to LEM dissipation estimates (c) buoyancy frequency N, (d) temperature (blue), salinity (red) and potential density (black). Light gray lines in (b) show factor of 2 bounds.

The survey-averaged profiles of TKE dissipation rates (ϵ) show similar patterns and magnitudes throughout the water column and vary over one order of magnitude (Fig. 3.8a). The survey-averaged density (black), temperature (blue), and salinity (red) structure of the upper 1000 meters of glider survey area of the GoM is shown in Fig. 3.8d. The survey-averaged profiles of MicroRider TKE dissipation rates ($\epsilon_{\mu R}$), Thorpe scale TKE dissipation rates (ϵ_{TH}), and LEM TKE dissipation rates (ϵ_{LEM}) covary over the entire water column (Fig. 3.8a). Dissipation is elevated near the surface in the GCW layer, and it gradually falls to a minimum at the interface between TACW and AAIW layer at depth $\approx$ 700 m. Below that depth, it gradually increases with depth until the bottom of the survey depth.

The ratio of the survey-averaged profiles $\epsilon_{\mu R}/\epsilon_{TH}$ (red) and $\epsilon_{\mu R}/\epsilon_{LEM}$ (black) are shown in Fig. 3.8b. The gray dashed lines in Fig. 3.8b represent the factor of two bounds. The estimated ratio shows that the survey-averaged TM and LEM estimated TKE dissipation agree within a factor of 2 to the MicroRider measurements. The ratio of $\epsilon_{\mu R}/\epsilon_{TH}$ (red) varies by a factor of 3; it appears

the averaging is biased due to the low detection by TM in the upper 200 m (Fig. 3.12). The vertical mean and standard deviation of $\epsilon_{\mu R}/\epsilon_{TH}$ are 1.0661 and 0.3970 and $\epsilon_{\mu R}/\epsilon_{LEM}$ are 1.0801 and 0.3889.

The lowest detection level of the LEM is determined using the noise level of the estimated vertical water velocity using eq. 2.1 as $\epsilon_{noise} = 0.58 \times N \times (0.002)^2$, where vertical velocity noise $w_{noise} \approx$ 0.002 m s^{-1}. The blue dashed line in Fig. 3.8a represents the LEM's noise level/lowest detection limit.

Further, the survey-averaged ϵ_{TH} and ϵ_{LEM} are plotted in a scatter plot against the survey-averaged $\epsilon_{\mu R}$ (Fig. 3.9), where the color represents the temperature of the respective depth bin. The scatter plots of survey-average ϵ_{TH} and ϵ_{LEM} show a strong positive relationship with the $\epsilon_{\mu R}$ (Fig. 3.9). A simple least-squares fit of survey-averaged ϵ_{TH} and ϵ_{LEM} against $\epsilon_{\mu R}$ produced the line of best fit represented by the black line in both panels. The overall regression found statistically significant, and the analysis of the residuals shows no violation of the regression assumptions. R-Squared value indicates the survey-averaged ϵ_{TH} captured 47$\%$ variance of survey-averaged $\epsilon_{\mu R}$ ϵ_{TH} versus $\epsilon_{\mu R}$ (R^2 = 0.47 with p <.000) (Fig. 3.9a). In addition, the survey-averaged ϵ_{LEM} captured 84$\%$ variance of survey-averaged $\epsilon_{\mu R}$ (R^2 = 0.84 with p <.000) (Fig. 3.9b). Relatively lower R-squared value for TM method. However, a comparison between the 1:1 line (gray line) and the line of best fit indicates that estimated ϵ_{TH} and ϵ_{LEM} tend to underestimate at high TKE dissipation rates and overestimate at low TKE dissipation rates.

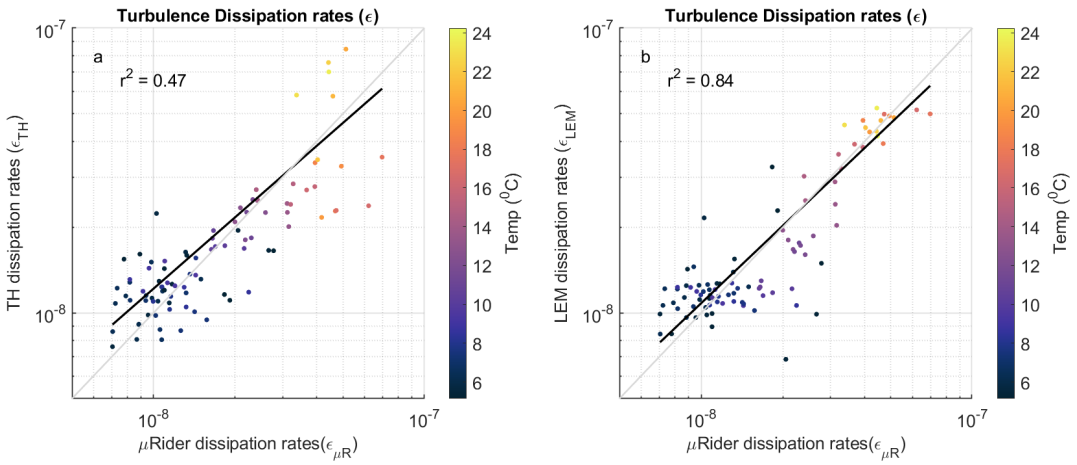

Figure 3.9: Scatter plots of survey-averaged TKE dissipation rates (a) ϵ_{TH} vs $\epsilon_{\mu R}$ (b) ϵ_{LEM} vs $\epsilon_{\mu R}$. The black like represent the best linear fits and the gray line represent one-to-one line.

3.4.2 PROBABILITY DISTRIBUTION

Probability density functions (PDFs) of $\epsilon_{\mu R}$ (gray patch), ϵ_{TH} (black line) and ϵ_{LEM} (red line) are plotted in (Fig. 3.10). Fig. 3.10a represents the PDFs of the full resolution data. The distribution of the $\epsilon_{\mu R}$ is right-skewed lognormal with a long tail at a higher magnitude. A similar distribution of measured turbulence is discussed in Gregg et al. (1993). The sharp cutoff is observed at low magnitudes of $\epsilon_{\mu R}$, where the $\epsilon_{\mu R}$ falls near the measurement's noise level. In contrast, the distribution for ϵ_{TM} and ϵ_{LEM} is nearly lognormal. The stratification-dependent lowest detection level for both methods limits the observation of low magnitude TKE dissipation. Fig. 3.10b represents the PDFs of bin-averaged data over 10-m depth bins. The data averaged over 10-meter depth bins increase the agreement between the distribution from LEM, TH, and MicroRider. The distributions of the bin-averaged data appear nearly lognormal.

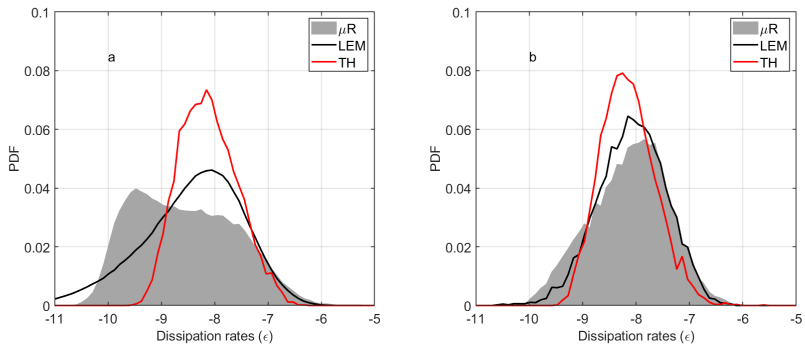

Figure 3.10: Probability density functions (PDFs) of $\epsilon_{\mu R}$ (gray patch), ϵ_{TH} (black line) and ϵ_{LEM} (red line) (a) full resolution data (b) bin-averaged data.

The TKE dissipation rates from all three methods were further sorted into four water mass layers (GCW, SUW, TACW, and AAIW) found in the upper 1000 m of the GoM. The distributions of ϵ_{TH} and ϵ_{LEM} agree with the $\epsilon_{\mu R}$ distributions fairly well in the GCW and SUW layers (Fig. 3.11(a-b)), where the magnitude of ϵ is high. However, distributions of ϵ_{TH} and ϵ_{LEM} largely vary from the distribution of $\epsilon_{\mu R}$ at weakley stratified TACW and AAIW water layers (Fig. 3.11(c-d)). That finding reconfirms the lower detection due to the stratification-dependent detection limit of TM and LEM. The PDFs of the bin-averaged $\epsilon_{\mu R}$, ϵ_{TH} and ϵ_{LEM} shows improved agreement between the distribution from LEM, TH, and MicroRider at all water four layers (Fig. 3.11(e-h)).

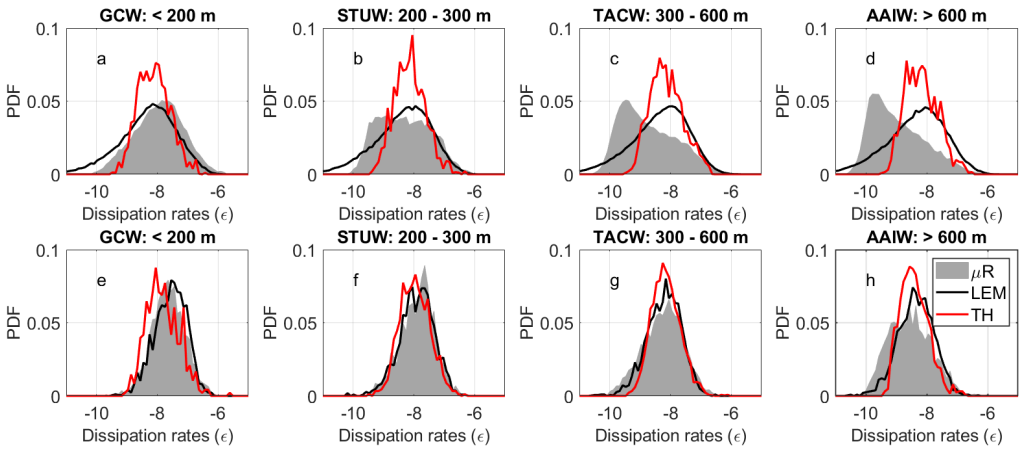

Figure 3.11: Probability density functions (PDFs) of $\epsilon_{\mu R}$ (gray patch), ϵ_{TH} (black line) and ϵ_{LEM} (red line) sorted by water mass GCW, SUW, TACW, and AAIW (a - d) full resolution data (b - d) bin-averaged data.

3.4.3 Point-to-point comparison

The Hovmöller plot of inferred TKE dissipation rates using TM is presented in Fig. 3.12c. TM applied to the glider data identified a few overturns in the upper $\approx$ 200 m (Fig. 3.12c). However, the detection of overturns using TM increased depth below $\approx$ 200 m. The Hovmöller plot of ϵ_{TH} shows that TM successfully captured the elevated TKE dissipation rate in the thermocline, and the magnitude of TKE dissipation decreased in the deep water. Additionally, the patchy nature of turbulence is also observed in the TM estimated TKE dissipation rates. Overall, TM captures the spatiotemporal distribution of turbulence similar to the MicroRider, but the magnitude is higher than the MicroRider dissipation in weakly stratified water. The mean value ϵ_{TH} for the entire dataset is $1.6667 \times 10^{-8}\, Wkg^{-1}$.

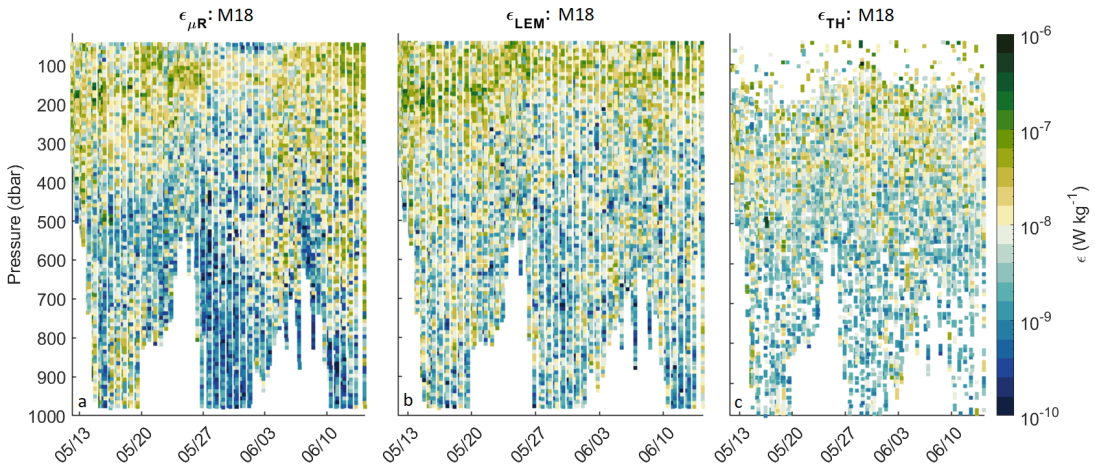

Figure 3.12: Hovmöller diagram of the (a) $\epsilon_{\mu R}$, (b) ϵ_{LEM}, and (c) ϵ_{TM} from the glider survey region of Gulf of Mexico during the GoMix experiment glider mission in 2018.

The Hovmöller plot of MicroRider dissipation rates and LEM (calibrated with TM) inferred dissipation rates are presented in Fig. 3.12a and Fig. 3.12b, respectively. The highest ϵ values were observed in near-surface layers and the near seabed over the continental slope, whereas the lowest ϵ estimates were obtained when the glider was in deep water. Due to boundary layer processes, high TKE dissipation is expected in the surface layer and thermocline (MacKinnon et al., 2016), where the enhanced dissipation rates and mixing levels on deep water over the GoM continental slope maybe attributed to the steep slope and rough topography, and the production and interaction of internal waves, internal tides, and topographic waves (Nash et al., 2004; Wang et al., 2016; St. Laurent and Merrifield, 2017). Overall, LEM did a better job compared to TM to capture the spatiotemporal distribution of turbulence similar to the MicroRider, but overestimates TKE dissipation in weakly stratified water. The mean value from ϵ_{LEM} and $\epsilon_{\mu R}$ are 2.0267×10^{-08} and $2.3118 \times 10^{-08}\ Wkg^{-1}$ respectively. The lowest detection level (noise level) in ϵ measurements based on MicroRider data in the was $1 \times 10^{-10}\ Wkg^{-1}$.

The resulting data were further compared in scatter plots (Fig. 3.13), color plotted with bin counts. The solid red line represented the best fit constructed by a simple least-squares fit, and dashed red and dashed black represent the factor of 2 and 5 bounds from the best-fit line. Fig. 3.13a

shows the scatter plot from dissipation rates from two shear probes of the MicroRider separated by a few centimeters. Dissipation rates from shear probes-1 ($\epsilon_{\mu R1}$) and shear probes-2 ($\epsilon_{\mu R2}$) show a strong positive correlation (Fig. 3.13a). Point-to-point comparison using bin-averaged data shows that 37% of data agree within the factor for 2 (red dashed) and 76% agree within the factor for 5 (black dashed) (Fig. 3.13a).

Inferred dissipation rates from TM (ϵ_{TH}) and LEM (ϵ_{LEM}) are positively correlated with MicroRider dissipation rates $\epsilon_{\mu R}$ (Fig. 3.13(b-c)), where, $\epsilon_{\mu R}$ is taken as the average of $\epsilon_{\mu R1}$ and $\epsilon_{\mu R2}$. Point-to-point comparison of ϵ_{TH} against the $\epsilon_{\mu R}$ shows 46% and 85%of data agrees within the factor for 2 (red dashed) and 5 (black dashed) respectively (Fig. 3.13b). The scatter plot between ϵ_{LEM} and $\epsilon_{\mu R}$ shows 39% and 77% of data agrees within the factor for 2 (red dashed) and 5 respectively (black dashed) (Fig. 3.13c).

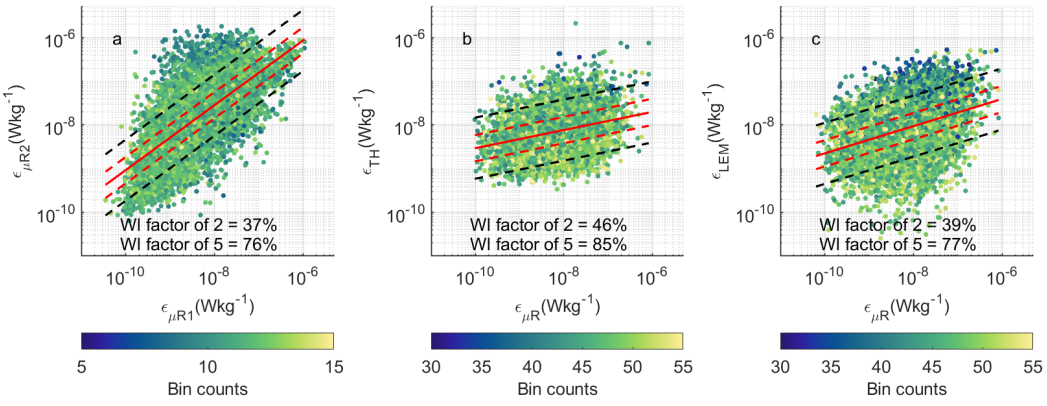

Figure 3.13: Scatter plots of TKE dissipation rates from (a) Two shear probe of MicroRider (b) ϵ_{TH} vs $\epsilon_{\mu R}$ (b) ϵ_{LEM} vs $\epsilon_{\mu R}$. The red solid like represent the best linear fits, red dotted line represent factor of 2 bounds and the black dotted line represent factor of 5 bounds.

3.5 Discussion

In this study, we applied the TM and LEM (calibrated with TM) to glider-collected CTD data from the continental shelf and slope environment of the GoM and compared the results with the

MicroRider measurements. There are many significant similarities in the TKE dissipation rates from MicroRider, TM, and LEM; however, some critical differences also need to be considered when using TM and LEM to estimate ocean turbulence. Our primary objective was to establish the methodology to calibrate LEM using TM and perform qualitative and quantitative assessments of the TM and LEM estimated TKE dissipation rates against MicroRider. Let's review the finding from both methods and the comparison.

3.5.1 Thorpe Scale

This study successfully applied the TM to CTD data collected by an underwater glider. The mean values of ϵ from TM and MicroRider at all depths agree by a factor of two. The agreement exceeds a factor of two in the upper $\approx$ 200 m due to the few overturns detected by TM in shallow water (Fig. 3.12c). TM estimate TKE dissipation only when an overturn is detected; the absence of estimation of dissipation at time/place (Fig. 3.12c) indicates that the dissipation rate is below the detection limit of TM (Ferron et al., 1998). TM's overturn detection is mainly limited by the density resolution/ stratification and vertical resolution of the CTD (Galbraith and Kelley, 1996). Estimated ϵ_{TH} with corresponding Thorpe lengths (L_{TH}), length of overturns (L), and the smallest observable overturn lengths (L_{min}) are shown in Fig. 3.14(a-d). ϵ_{TH} and (L_{TH}) is estimated using Eq. 2.9 and Eq. 2.10. In a stratified ocean, a similar length scale of Thorpe lengths is Ozmidov length $L_{oz} = \epsilon^{1/2} N^{-3/2}$, which measures the maximum vertical overturn displacement (Thorpe et al., 2007). In the thermocline with $\epsilon = 1 \times 10^{-6}\, W\, kg^{-1}$ and buoyancy frequency $N = 0.025\, s^{-1}$ is $\approx\ 0.25\, m$ and increased as stratification decreased. A similar increase in L_{TH} and L is observed in Fig. 3.14(b-c).

The vertical resolution of the glider data $\Delta_z \approx$ 0.21 m; therefore, according to the sampling theorem, the minimum detectable thickness of the overturn is 0.42 m. Following the recommendation of Galbraith and Kelley (1996), we set the minimum size of an overturn to be valid as 1 m, which is $\approx$ 5 times the vertical resolution of the glider data. Therefore, fewer overturns upper $\approx$ 200 m are likely due to the vertical resolution of the glider CTD. Additionally, the quality control criteria described in subsection 2.2.3 flagged and removed $\approx 35\%$ of the detected overturn as a

false positive.

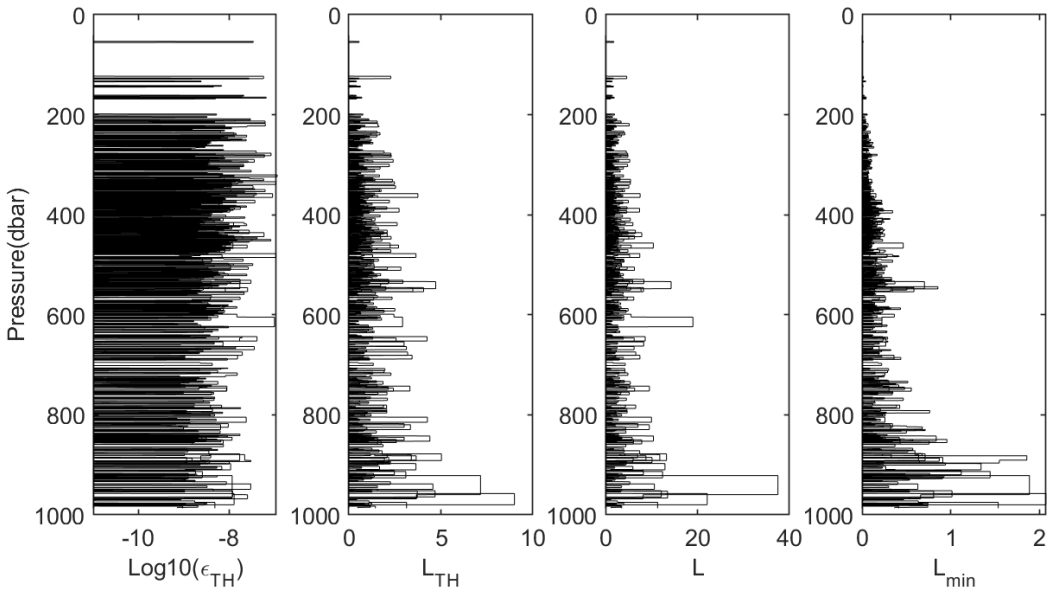

Figure 3.14: (a) ϵ_{TH}, (b) Thorpe Length, (c) Overturn Length and (d) smallest observable Thorpe Scale from 5 profiles collected during the GoMix experiment glider mission in 2018.

3.5.2 Large Eddy Method

The LEM was successfully applied the to Slocum glider data and directly compared the estimated ϵ against the MicroRider measurement. The mean values of ϵ from LEM calibrated with TM and MicroRider at all depths agree within a factor of two. The direct comparison of the survey-averaged data reveals a significant correlation at all depths. The histograms generated from the raw data show better agreement within the GCW and SUW but are overestimated in the TACW and AAIW layers where the magnitude to the ϵ is low. The disagreement is attributed to the stratification-dependent noise level of the LEM Beaird et al. (2012). The LEM estimated dissipation falls to near its noise level (lowest detection level) at the TACW and AAIW, which results in fewer measurements (Fig. 3.8a). However, the bin averaged data show better agreement at all water layers, indicating the detection limit for the glider sensors. Point to point comparison of

bin-averaged LEM and MicroRider ϵ show a similar spread from the mean as the spread of ϵ from two shear probes of MicroRider. The ratio of the majority of data points falls under the factor of 5; some data occasionally differ more than a factor of 10.

Estimating ϵ using the large-eddy method (LEM) assumes that an overturning eddy dissipates most of its kinetic energy when it overturns once. The challenges involved in applying the LEM are constructing the velocity scale and calibration. The velocity scale is constructed from the estimated vertical velocity of water after applying the filter described in section 3a. The noise level/ bias associated with the estimated vertical water velocity can lead to errors in the ϵ estimation. In contrast to the Merckelbach et al. (2010), we used the pressure data from the glider CTD to estimate vertical water velocity, which resulted in less noise ($\approx$ 0.002 m s^{-1}) than reported by Merckelbach et al. (2010) ($\approx$ 0.004 m s^{-1}). Additionally, any spurious vertical velocity signals or spikes resulting from inadequately optimized flight or flight model (Merckelbach et al., 2010; Frajka-Williams et al., 2011) can lead to errors and should remove from the ϵ estimation.

3.6 Summery

The vertical microstructure profiler dominates the turbulence measurements in the world ocean. However, the deployment of those instruments is expensive and is dependent on a highly trained workforce. Additionally, shipboard observations may not be sufficient to resolve the spatiotemporal variability of the ocean mixing because of the short survey times and relying on measurements from only a few stations.

Here, A direct comparisons is attempted between the rate of TKE dissipation ϵ using the MicroRider and estimated ϵ using TM from glider hydrography, LEM from glider hydrography, and vehicle dynamics. The measurements were used from the same Slocum glider 35-day mission sampled over the continental slope of the Gulf of Mexico. A total of 146 vertical profiles from the MicroRider and corresponding TM and LEM profiles were analyzed. Comparison with the μRider measurement shows that TM and LEM estimated TKE dissipation rates are valid within a factor of 2 to the μRider measurement. Both TM and LEM reasonably represent the spatiotemporal variability of TKE dissipation rates captured by MicroRider but are systematically overestimated when the

magnitude of TKE dissipation is low. The TM and LEM both estimates the TKE dissipation rate from the data collected by the glider sensors with a sampling frequency of 0.5 Hz. Therefore, it is not expected the estimation will be as accurate as the direct microstructure measurements. Still, it will be useful as an additional tool for the economic estimation of turbulence using glider surveys worldwide.

Additionally, the new calibration method of LEM using TM allows calibration from the glider CTD data and removes the dependency on microstructure measurement from the glider survey area and survey period. Therefore, LEM can be applied to the glider data, which doesn't have microstructure measurement during the glider survey. For example, the glider was deployed as a part of the GoMix experiment (M16) in 2016. The mission objective was to quantify the turbulence structure at the edge of the continental slope of the northern GoM. Due to saltwater leakage, the MicroRider only sampled for ten dives when the glider was on the continental shelf. LEM calibrated with TM was applied to the glider data to estimate the TKE dissipation rates (ϵ). The TKE dissipation rates from MicroRider and glider estimates are shown in Fig. 3.15 (a-b). The mean value of MicroRider and glider estimated dissipation rates are 8.8447×10^{-08} and 5.4418×10^{-08} Wkg^{-1}. The magnitude of the MicroRider and glider estimated is higher in the thermocline with maximum values exceeding 10^{-6} Wkg^{-1}. Most values of the estimated TKE dissipation rates over the continental shelf and slope are greater than 10^{-8} Wkg^{-1}, while the dissipation rate in the deepwater drop in order of 10^{-10} Wkg^{-1}, which is consistent with the previously reported studies (Wang et al., 2016; Ledwell et al., 2016). The probability distibution of MicroRider and glider estimated dissipation rates of overlapping profiles are in good agreement, excpt dissipation rates falls below 10^{-9} Wkg^{-1}.

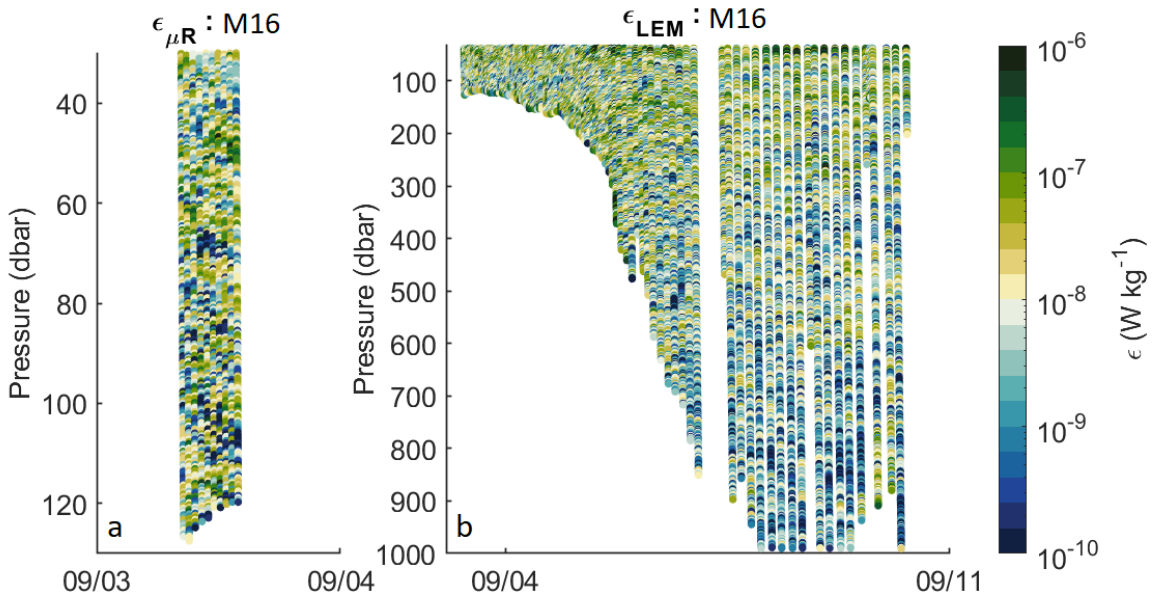

Figure 3.15: Hovmöller diagram of (a) $\epsilon_{\mu R}$ and (b) LEM (calibrated with TM) estimated ϵ_{LEM} for the entire M16 deployment deployed in 2016.

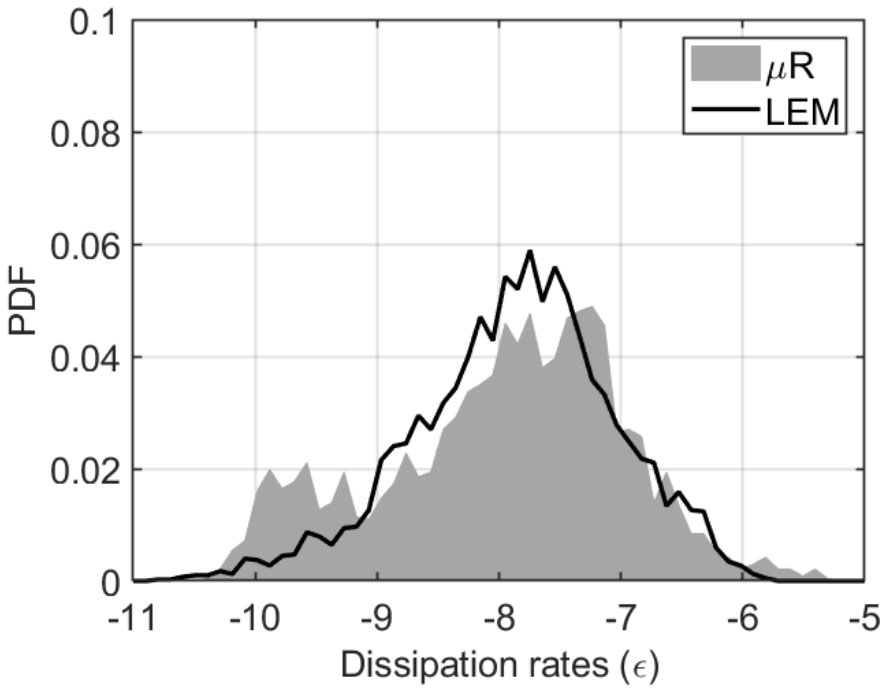

Figure 3.16: PDFs of $\mu Rider$ dissipation rates (gray patch) and LEM estimated dissipation rates from the corresponding 10 profile of $\mu Rider$ from glider deployed in 2016.

4. TURBULENT AND DOUBLE-DIFFUSIVE MIXING: LOOP CURRENT AND LOOP CURRENT EDDIES

4.1 Introduction

In this chapter, we present a glider-based estimation of turbulence and turbulence-related parameters, i.e., dissipation rate, Turner angle, mixing efficiency, geostrophic adjustment, from two Slocum gliders deployments (M15a and M15b) in the northwestern GoM on 5 August and 22 August 2015, respectively. Here, we aim to characterize the turbulent field in LC and LCE of the entire water column ($\approx 1000\,m$) and then examine the turbulent and double-diffusive mixing processes. Additionally, mixing parameters due to double diffusion condition such as the diffusivity of heat and salt are parameterized. Additionally, I will classify and assess the vertical structure of mixing processes e.g., double diffusiveness, salt-fingering, finestructure stability, under different environmental conditions in the deep Gulf of Mexico.

The Gulf of Mexico (GoM) is a semi-enclosed marginal sea. The surface circulation of the GoM is highly dominated by the Loop Current System, along with high mesoscale eddy activity. The Loop Current (LC) is a strong geostrophic current that enter the GoM through the Yucatan channel and exit through the Florida Straits (Hamilton, 1990). At the retracted state, the LC promptly turns east after slight intrudes into the GoM and exits through the Straits of Florida. When at the extended state, LC slowly stretches northward reaches between $27^\circ\ N - 28^\circ\ N$ (Leben, 2005; Gopalakrishnan et al., 2013). The extended form of the LC sporadically sheds large anticyclonic Loop Current eddies (Schmitz Jr, 2005) up to 200km in radius (Meunier et al., 2019). Before complete separation from LC, an LCE may detach and reattach several times. A separated LCEs drifts westward, transporting relatively warm and salty Caribbean water (Merrell Jr and Morrison, 1981; Morrison et al., 1983; Hamilton et al., 2005) and eventually decaying along the western GoM coast, diffusing large amounts of heat and salt (Meunier et al., 2018; Sosa-Gutiérrez et al., 2020).

Energetic mesoscale eddies often involve large-amplitude anomalies in ocean salinity, temperature, and other properties. It has been well observed that mesoscale and submesoscale eddies are associated with elevated vertical velocities (Liang et al., 2017; Chen et al., 2020), microscale turbulence, and diapycnal-isopycnal mixing (Mukherjee et al., 2016). These processes influence the mass, heat, nutrients, gas, and pollutant transport between the ocean surface and interior. Upwelling related to anticyclonic (clockwise rotation in the northern hemisphere) eddies are known to significantly contribute to the nutrient supply to the euphotic zone of the GoM (Nowlin Jr et al., 2000; Damien et al., 2021). The GoM mesoscale variability in- fluence the oceanic heat advection and heat exchange through air-sea interaction, which contributes to climate extremes and hurricane intensification (Putrasahan et al., 2017; Shay et al., 2000; Jacob and Shay, 2003).

In addition to turbulent mixing, double-diffusive mixing plays an important role in creating well-mixed internal layers in the global ocean. The double-diffusive process is widely present in the world ocean including Gulf of Mexico (Schmitt, 2003; Schmitz Jr et al., 2005) and has previously been observed in warm-core eddies including in the Gulf of Mexico (Fine et al., 2018; Meunier et al., 2018; Molodtsov et al., 2020). Double diffusion occurs when water masses of different densities overlay and interact. Because ocean density is controlled by salinity and temperature, the diffusion rates of heat and salt are different. Owing to molecular differences, heat diffuses faster than salt, which induces statically unstable temperature and salinity stratification; this process is termed double-diffusion (Stern, 1960). Double-diffusion has two forms, 1) diffusive convection (cooler-fresher water overlaying warm-salty water) and 2) salt-fingering (warm-salty water overlaying cooler-fresh water). In the Gulf of Mexico warm-salty Subtropical Underwater overlies relatively cold-fresh Tropic Atlantic Central water and Antarctic Intermediate Water, which we hypothesize can provide conditions necessary for double diffusion. The relative strength and vertical structure (placement in the water-column) of double-diffusive and salt-fingering processes is investigated and quantified in this chapter.

4.2 Data Sets

Two Slocum Glider "Stommel" S/N - 540 (hereafter M15a) and "Sverdrup" S/N - 541 (hereafter M15b) surveyed the northwestern GoM (Fig. 2.1) from August to November 2015. During that deployment, M15a surveyed a LCE and M15b surveyed the northward extended LC; both gliders sampled from surface to 1000 m depth and were equipped with finescale hydrographic sensors CTD, CDOM, and fluorescence (Table: 2.1). In this chapter, we will use the glider-based turbulence estimation to the finescale hydrographic data collected by glider M15a and glider M15b.

4.3 Method

4.3.1 Turbulent mixing

4.3.1.1 Estimation of TKE dissipation rate

In order to estimate the TKE dissipation rate, the glider-based turbulence estimation Large Eddy Method (LEM) (Beaird et al., 2012) is applied to the data collected by M15a and M15b. Next, LEM is calibrated and compared to estimates using the density-based Thorpe Scale Method (TM) (Thorpe, 1977) discussed in Chapter 2.

4.3.1.2 Vertical Eddy diffusivity

The vertical turbulent transport of density is often referred to as the vertical eddy dif- fusivity (k_ρ). Quantifying the magnitude of the subsurface diffusivity provides improved understanding of the mixing intensity and the influence of the main kinetic energy drives, i.e., LC and LCE in the mixing processes of GoM.

In a stably stratified ocean, the vertical eddy diffusivity (k_ρ) can be calculated from the TKE dissipation rate by the Osborn relation (Osborn, 1980; Goodman and Wang, 2009) as,

$$k_\rho = \Gamma \frac{\epsilon}{N^2} \tag{4.1}$$

where a mixing efficiency of $\Gamma = 0.2$, $\epsilon =$ TKE dissipation rate and, $N =$ Buoyancy frequency.

4.3.1.3 Geostrophic shear

The shear-generated instabilities or double-diffusive processes are generally thought to be the origin of the mixing within the stratified ocean interior (Gargett, 1989). We calculated along-track geostrophic shear to assess the mixing processes under the influence of the shear-associated with LC and LCE. The along-track geostrophic shear (vertical gradient of the geostrophic velocity) (S_g) associated with the eddy is computed using the thermal wind balance (Van Gastel and Pelegrí, 2004) as,

$$S_g = \left(\frac{g}{\rho_0 f}\right)\left(\frac{\partial \rho}{\partial x}\right) \tag{4.2}$$

where N is the buoyancy frequency, f is the Coriolis parameter, g is gravitational acceleration, and x is the distance between the glider profiles along the glider track.

4.3.2 Categorizing diffusion mixing processes using Turner Angle

4.3.2.1 Density ratio and Turner Angle

The oceanic density ratio (R_ρ) is a commonly used parameter for identifying different double-diffusion from finescale hydrographic measurements (Schmitt, 1981, 1987, 2003; Fer et al., 2010). The relative strength of double-diffusion in the water column can be identified using the density ratio (R_ρ) (Turner, 1979) expressed as,

$$\overline{R_\rho} = \frac{\alpha \overline{T_z}}{\beta \overline{S_z}} \tag{4.3}$$

where α and β are the thermal expansion and haline contraction coefficients, S_z and T_z are the vertical gradients of salinity and temperature, and the overbar represents a bulk gradient.

We calculate R_ρ from $\approx 0.1\,m$ resolution glider CTD temperature and salinity profiles in $5\,m$ moving segments. Density ratios between 1 and 2 are favorable conditions for strong double diffusion due to salt-fingering (Schmitt, 1981). Well-defined fine-structure thermohaline staircases are formed at a density ratio of less than 1.7 (see Section 4.5.3 for more on staircases). The fine-structure is classified "irregular" for R_ρ between $1.7 - 2$. However, the infinite range associated

with signs often makes the use of R_ρ ambiguous.

To remove that ambiguity in R_ρ Ruddick (1983) proposed Turner Angle (Tu), which is a function of R_ρ and ranges between $-180°$ to $180°$. Turner angle (Tu) identifies the mixing regimes, e.g., double diffusion, through the water column (Ruddick, 1983; Bebieva and Timmermans, 2016) as,

$$\overline{Tu} = tan^{-1}\left(\frac{1+\overline{R_\rho}}{1-\overline{R_\rho}}\right) \tag{4.4}$$

When Tu <$-90°$ or Tu >$90°$, the water column is gravitationally unstable; $72°$ <Tu <$90°$ the water column is favorable for strong salt fingering; $45°$ <Tu <$72°$ the water column is favorable for weak salt fingering; $-90°$ <Tu <$-51°$ the water column is favorable for strong diffusive convection; $-51°$ <Tu <$-45°$ the water column is favorable for week diffusive convection; $-45°$ <Tu <$45°$ indicates gravitationally stable conditions. Table: 4.1 provides a summary of mixing regimes categorized by the Turner angle. A schematic polar plot of Turner angle identifying different double-diffusive regimes is shown in Fig. 4.1.

Tu	**Double-diffusive regimes**
Tu < -90 or Tu > 90	Gravitationally unstable
72 < Tu < 90	Strong salt fingering
45 < Tu < 72	Weak salt fingering
-90 < Tu < -51	Strong diffusive convection
-51 < Tu < -45	Weak diffusive convection
-45 < Tu < 45	Gravitationally stable

Table 4.1: Double-diffusive regimes based on Turner Angle.

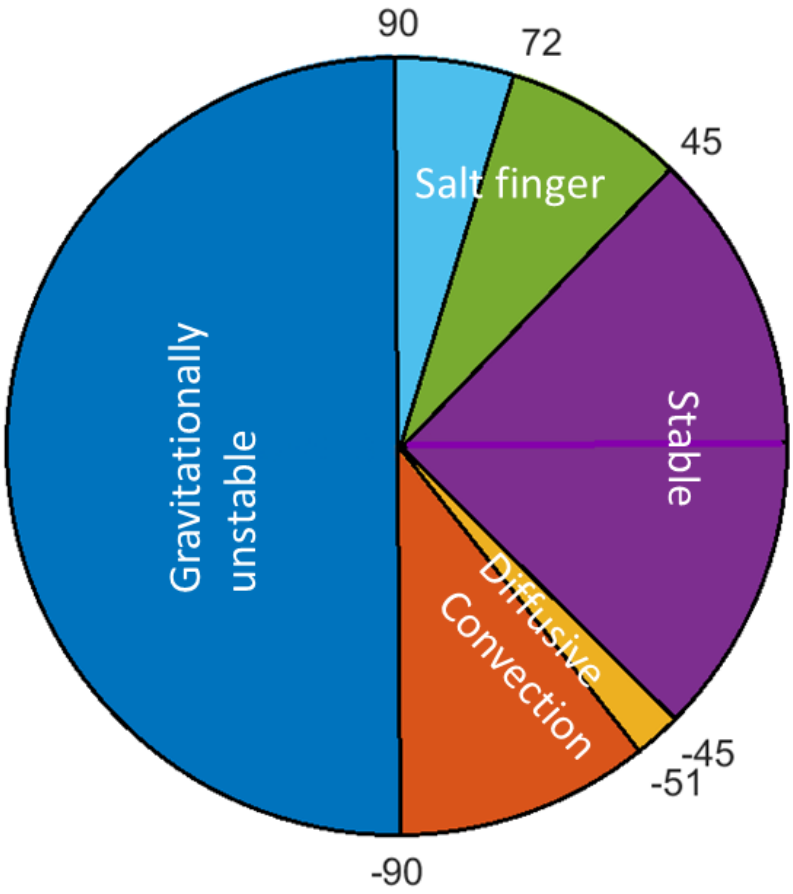

Figure 4.1: Schematic polar plot of Turner angle with background color depicting various double-diffusive regimes.

4.3.2.2 Eddy diffusivity of salt (k_s) and heat (k_θ)

For conditions favorable for salt fingering to occur, the eddy diffusivity of salt (k_s) can be calculated as (McDougall, 1988),

$$k_s = \left(\frac{R_\rho - 1}{1 - \gamma}\right) \frac{\epsilon}{N^2} \tag{4.5}$$

and

$$k_s = \frac{R_\rho}{\gamma} k_\theta \tag{4.6}$$

where, k_θ eddy diffusivity of temperature, R_ρ = density ratio and γ = heat/salt buoyancy flux ratio. γ >1 is favorable for diffusive convection and 0 <γ <1 is favorable for salt fingering.

4.4 Experiment overview/ observation

4.4.1 Loop Current Eddy

Composite figures of glider M15a track superimposed upon altimetry - derived sea surface height anomaly (SSHA) and surface currents are shown in Fig. 4.2 and Fig. 4.3 (Left track). In total, ten plots show the temporal and spatial evolution of SSHA, surface current, and approximate location of the glider from September 1 to October 31, 2015. The positive SSHA and the elevated surface current identify the position of an anticyclonic eddy (LCE) ($27.5°N$, $94°W$) at the north-western GoM (Fig. 4.2 and Fig. 4.3). The center of the LCE is characterized by a $+\,50\,cm$ SSHA anomaly, and surface currents reached $\approx 1\,m\,s^{-1}$.

The M15a data were sorted into time segments, which coincide with proximity to the LCE core. The different color of the glider track represents the corresponding GPS location of the time segments. The black and green section of the M15a track identifies the glider's location inside and outside of the LCE periphery, respectively. M15a entered the northern periphery of the LCE on August 14, 2015. On August 28, 2015, M15a reached near the center of the LCE and was sampled until September 9, 2015. By that period, the LCE drifted toward the south and started to weaken (Fig. 4.3 last panel).

The observed temperature (Fig. 4.4), salinity (Fig. 4.5), and density (Fig. 4.6) distribution shows the stratified water column in the GoM. Highest temperature is observed near surface and the upper thermocline (maximum temperature is $\approx 30°C$ is at the surface and exponentially drops to $\approx\ 5°C$ at $\approx\ 1000\,m$ depth). Similarly, higher salinity is observed in the upper thermocline with a maximum salinity exceeding 36.5 at the depth between $100\ -\ 200\,m$ and with a gradual drop with depth. The vertical temperature and salinity gradients resulted in vertical density gradients and therefore a variable vertical stability structure.

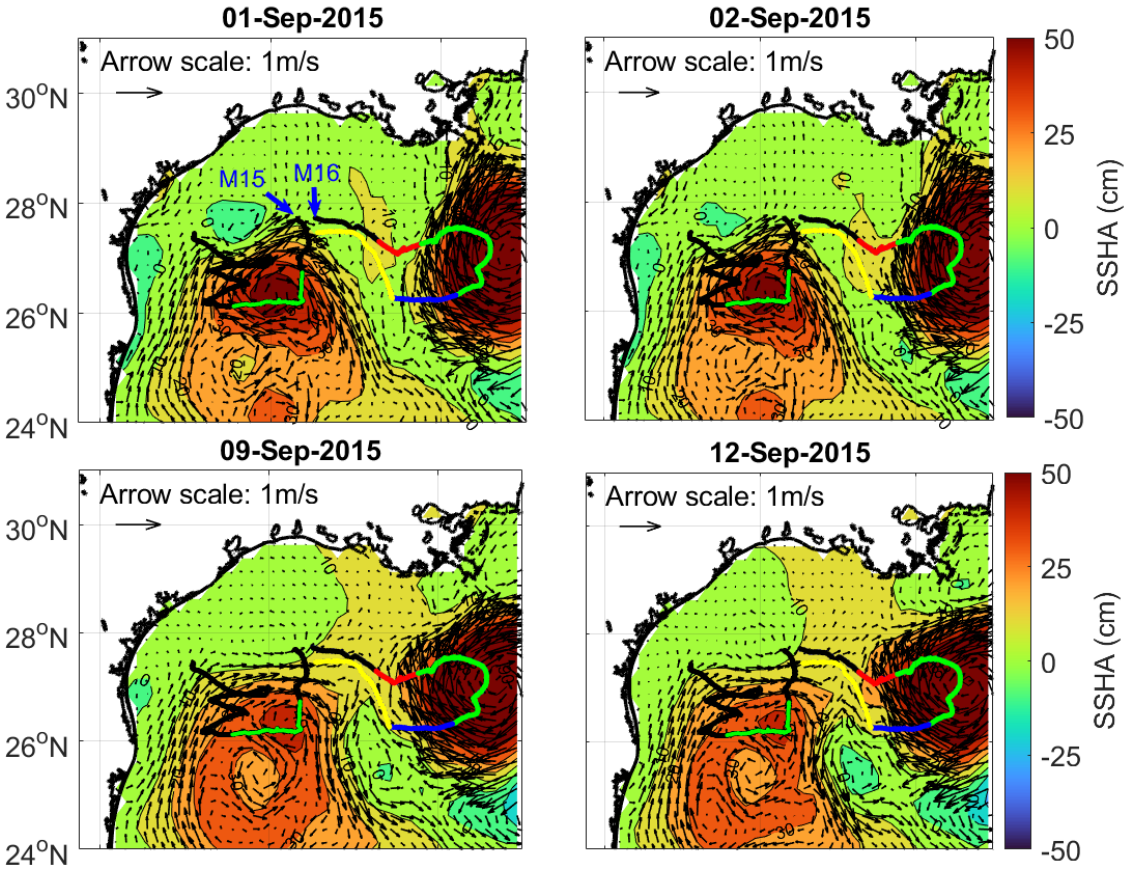

Figure 4.2: Tracks of glider M15a (left) and M15b (right) in the Northwestern Gulf of Mexico deployed in August 2015 color coded with survey dates. The green section of M15a track represent survey periods near the center of LCE (08/28/2015 - 09/09/2015). M15b track was divided into 5 section: Outside of LC (black and yellow: 08/31/2015 - 09/08/2015 and 10/20/2015 - 11/04/2015), at the edge of LC (red and blue: 09/08/2015 - 09/13/2015 and 10/11/2015 - 10/19/2015) and inside of LC (green: 09/14/2015 - 10/10/2015).The colormap represent the Sea Surface Height Anomaly (SSHA). Sea Surface Height Anomaly (SSHA) provided by NOAA CoastWatch/OceanWatch.

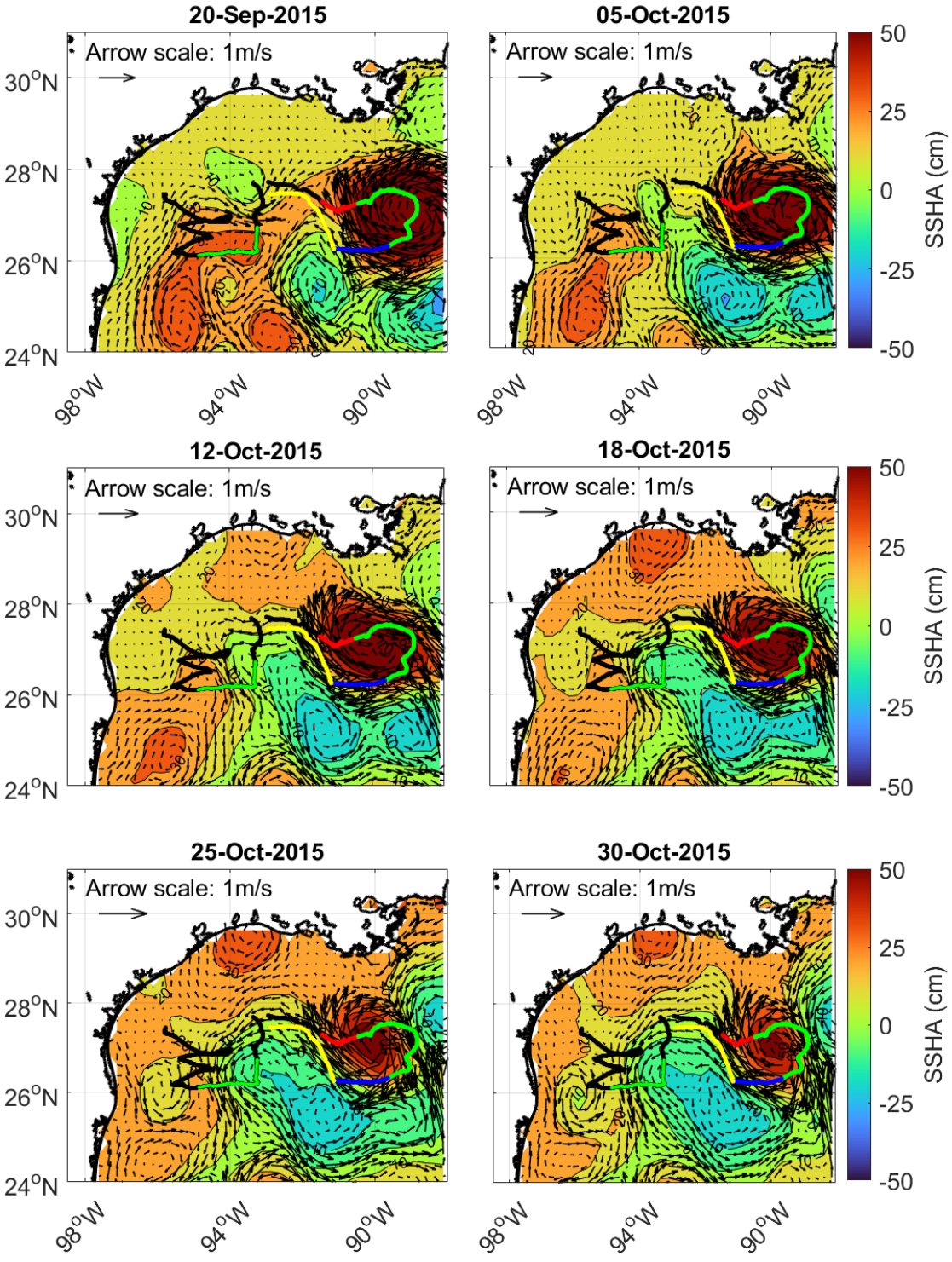

Figure 4.3: Continuation of Fig. 4.2.

The temperature, salinity, and density distribution reveal the existence of a subsurface core that defines the LCE structure (between depths of 50 and 250 m) and represents the water mass that entered into the Gulf of Mexico through the Yucatan Channel (Fig. 4.4). Subsurface warm water split the thermocline, pushed the isotherms (>$25°C$) upward, and the isotherm (<$25°C$) downward (Fig. 4.4). Similar deviations of isohalines (Fig. 4.5), and isopycnals (Fig. 4.6) were also observed. A gradual slope of isolines was observed when the glider was in the LCE periphery (14 -28 August), and a sharp drop of isolines was observed around the core boundaries. The deepening of isolines extends down to $\approx 800\,m$ beneath the LCE core.

The temperature and salinity relationship of the M15a is shown in Fig. 4.7. The relatively low near surface salinity suggests the presence of a terrestrial fresh water plume during summer (Morrison et al., 1983; Nowlin Jr et al., 2000) when the glider was over the continental shelf. The low salinity water was not found in later measurements when the glider was over the continental slope with seafloor depth over $1000\,m$. Offshore and in deep water, the observed surface salinity is $\approx$ 34.4, indicating the characteristic Gulf Common water (GCW) (Morrison et al., 1983; Nowlin Jr et al., 2000). Subsurface salinity maxima with salinity exceeding 36.5 beneath the core of LCE, indicating the presence of SUW (Fig. 4.4 and Fig. 4.5) (Rivas et al., 2008; Sosa-Gutiérrez et al., 2020). The presence of SUW beneath the LCE core is indicative of a water mass that originated in the tropical Atlantic and came into the Gulf of Mexico from the Caribbean Sea (rather than a locally water mass) (Fig. 4.5). The signature of high-salinity water extends below $400\,m$ depth within the eddy.

The Brunt-Väisälä frequency (N) (Fig. 4.8) shows a well-mixed surface mixed layer (ML) and weakly stratified interior of the GoM. The eddy core appeared to be well mixed with the Brunt-Väisälä frequency < $0.01s^{-1}$. A stripe of relatively strong stratification ($1.2 \times 10^{-3}\ s^{-1}$ < N < $1.5 \times 10^{-3}\ s^{-1}$) surrounds the core region of the eddy.

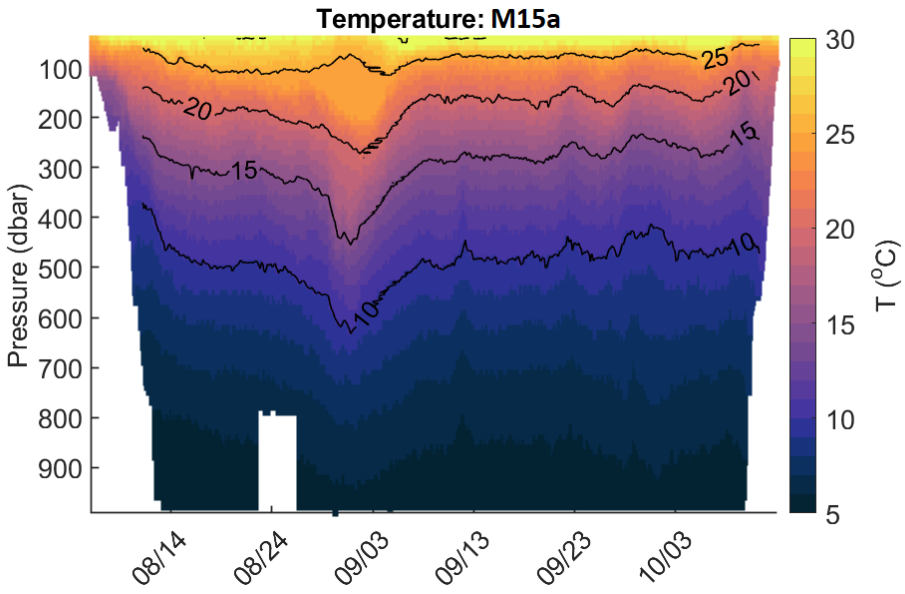

Figure 4.4: Hovmöller plot of temperature as a function of pressure and time form data collected by M15a deployed in 2015 in the northwestern Gulf of Mexico. The black lines represent the isothermal contours. The deepening of the isotherm outlines the location of the LCE.

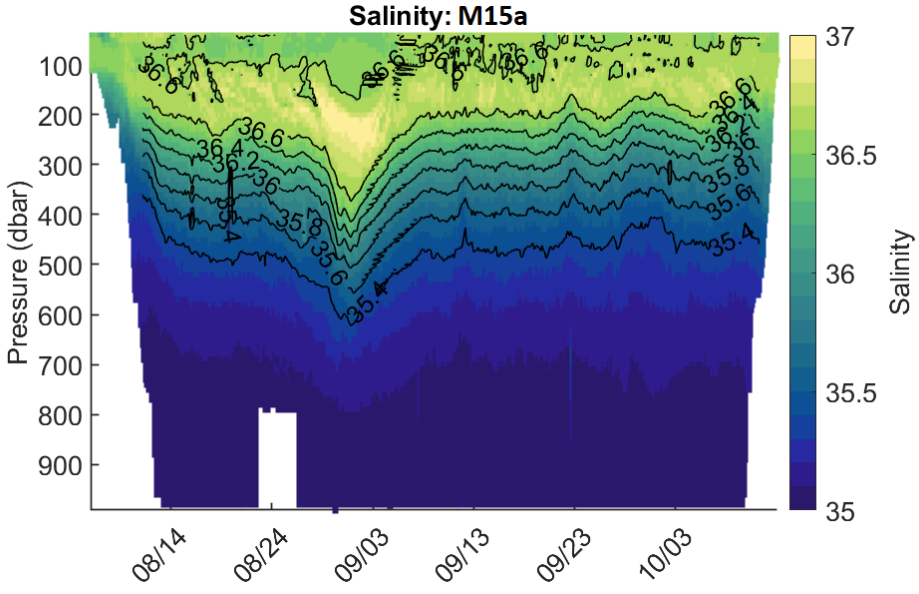

Figure 4.5: Hovmöller plot of salinity as a function of pressure and time form data collected by M15a deployed in 2015 in the northwestern Gulf of Mexico. The black lines represent the isohaline contours. The subsurface salinity maxima > 36.6 identifies high salinity core of subtropical under water.

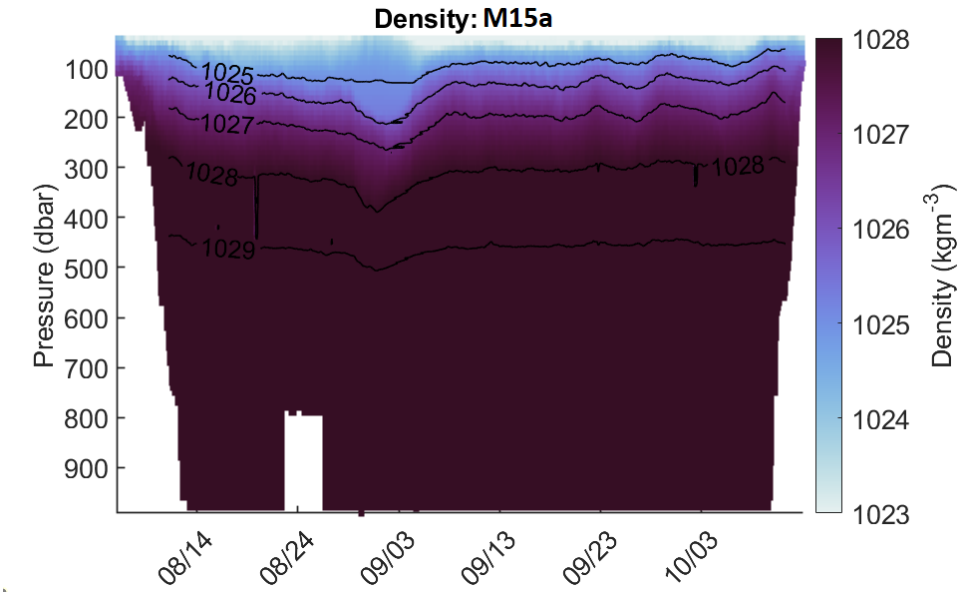

Figure 4.6: Hovmöller plot of density as a function of pressure and time form data collected by M15a deployed in 2015 in the northwestern Gulf of Mexico. The black lines represent the isopycnal contours.

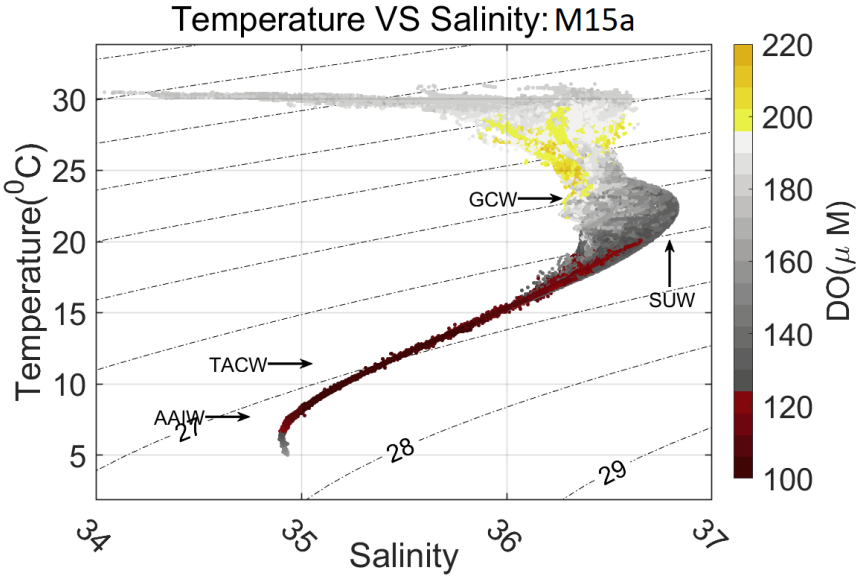

Figure 4.7: The temperature-salinity diagrams are shown for CTD data collected by M15a around the LCE and LCE periphery. The black contour lines show the isopycnals in kgm^{-3}. The colors represent dissolved oxygen concentrations.

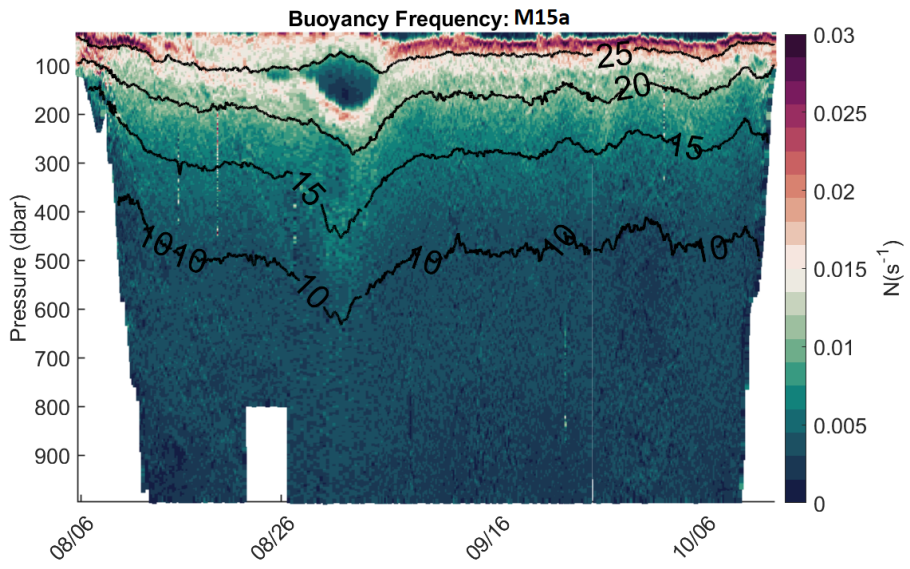

Figure 4.8: Hovmöller plot of Brunt-Väisälä frequency as a function of pressure and time estimated from data collected by M15a deployed in 2015 in the northwestern Gulf of Mexico. A strong stratification strip surrounding the core is observed.

4.4.2 Loop Current Extension

Composite figures of M15b track along with altimetry-derived sea surface height anomaly (SSHA) and surface currents are shown in Fig. 4.2 and Fig. 4.3 (Right track). The positive (> $+50\,cm$) SSHA anomaly and the elevated surface current (> $1m\,s^{-1}$) identify the presence of the strong anticyclone of Loop Current Extension (LC) center ($27°N,\ 89°W$) at the northwestern GoM (Fig. 4.2 and Fig. 4.3).

The track of M15b is divided into five sections: Black and yellow signify that the glider is outside of LC; red and blue show the glider is the edge of LC over sloping isopycnals, and green denotes a location inside of LC (Fig: 4.11). M15b reached outside the western edge of the LC on September 8, 2015. Between September 8 - October 10, 2015, the glider sampled inside the LC over the sloping and flat isolines; however, the glider did not quite reach the center of the LC extension. The glider exited the LC through the western edge on October 10, 2015 and continued to sample outside the LC.

Temperature distribution shows highest temperature recorded at the surface ($\approx\ 30°C$) and

gradually drops to depth. Elevated surface temperature ($\approx 30°C$) persisted until the end of October and gradually declined to $\approx 27.5°C$ by the end of the glider survey on November 4, 2015 (Fig. 4.9) indicating the seasonal progression from summer to fall to winter. A large body of homogeneous warm water identifies the subsurface location between depths of $20 - 300\,m$, resulting in the characteristics deepening of the isotherms (Fig. 4.9), isohalines (Fig. 4.10), and isopycnals (Fig. 4.11) down to $\approx 800\,m$ beneath the eddy cores.

The temperature and salinity relationship of M15b shows a trace amount of near-surface freshwater (likely Mississippi River plume water), Gulf Common water (Salinity $\approx$ 36.4), and a large volume of Subtropical Underwater (Salinity > 36.4) between temperature $20°C$ to $25°C$ (Fig. 4.12) and depth $200 - 300\,m$. The signature of high-salinity water extends below $600\,m$ depth and within the eddy.

The vertical structure of the estimated Brunt-Väisälä frequency (N) (Fig. 4.13) shows a well-mixed surface mixed layer (ML) and weakly stratified interior of the GoM. The LC core is well mixed ($N < 0.01\,s^{-1}$) and spatially isolated from the surrounding water mass by a stripe of relatively higher N at the edges and bottom of the water mass core ($1.2 \times 10^{-3}\ s^{-1} <$ N $< 1.5 \times 10^{-3}\ s^{-1}$). Elevated N is also seen very near the ocean surface ($N \approx 3 \times 10^{-3}\ s^{-1}$).

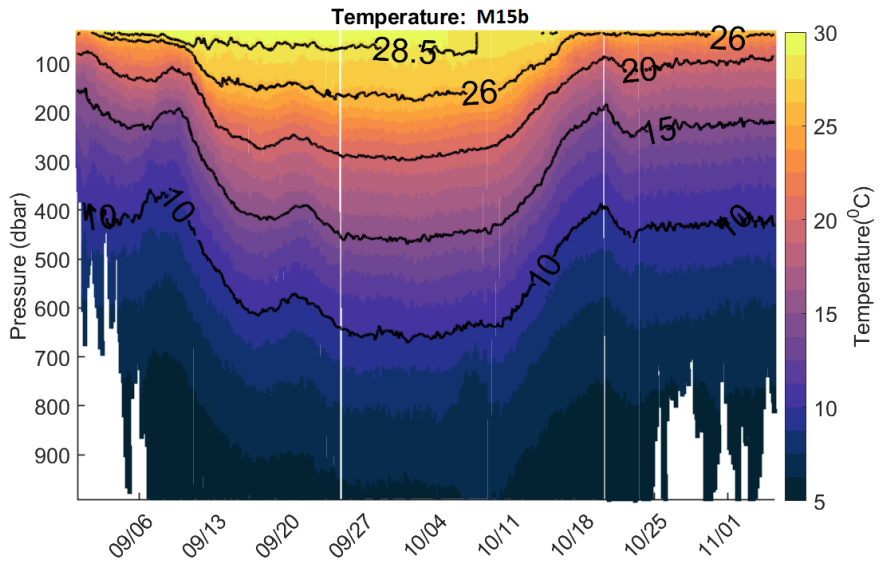

Figure 4.9: Hovmöller plot of temperature as a function of pressure and time form data collected by M15b deployed in 2015 in the northwestern Gulf of Mexico. The black lines represent the isothermal contours. The deepening of the isotherm outlines the location of the LC extension.

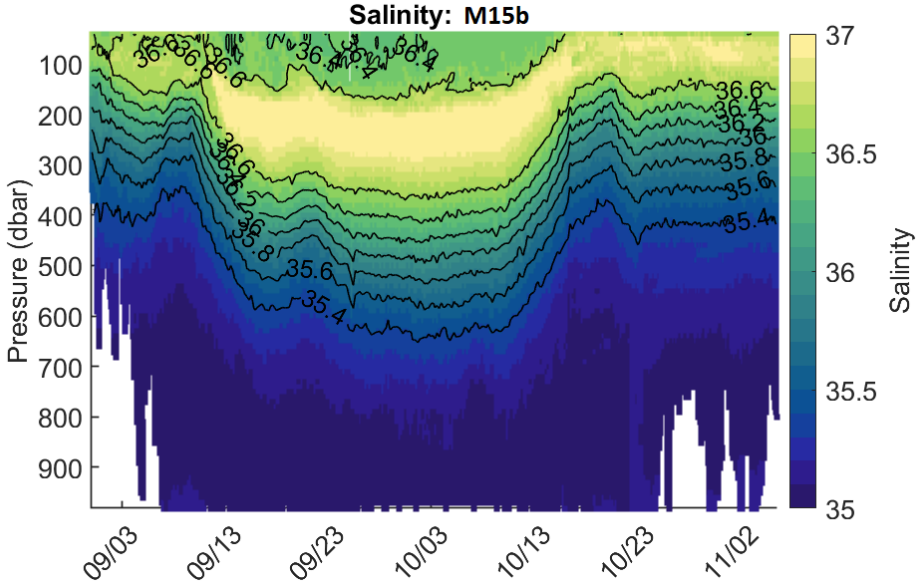

Figure 4.10: Hovmöller plot of salinity as a function of pressure and time form data collected by M15b deployed in 2015 in the northwestern Gulf of Mexico. The black lines represent the isohaline contours. The subsurface salinity maxima >36.6 identifies high salinity core of subtropical under water.

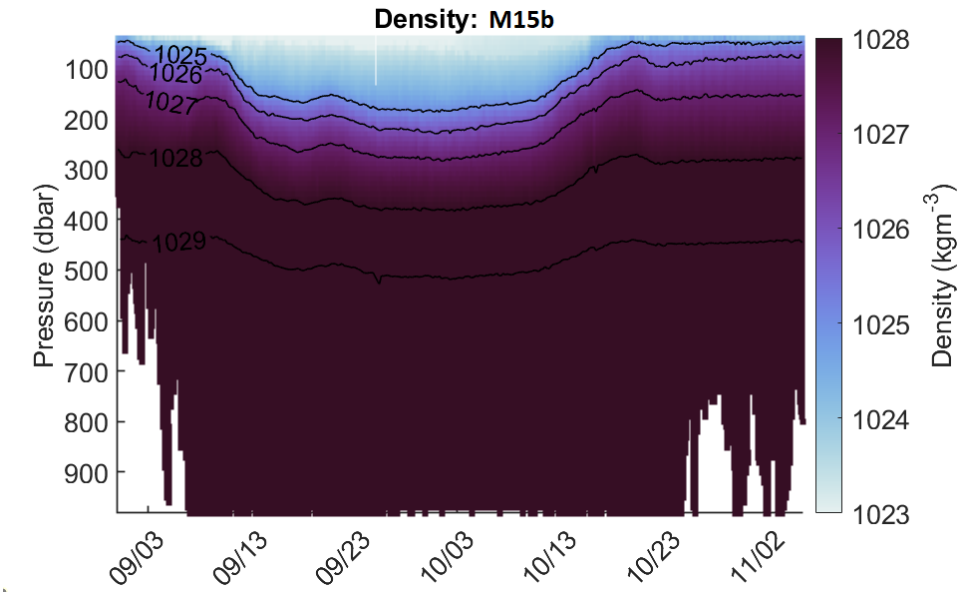

Figure 4.11: Hovmöller plot of density as a function of pressure and time form data collected M15b deployed in 2015 in the northwestern Gulf of Mexico. The black lines represent the isopycnal contours.

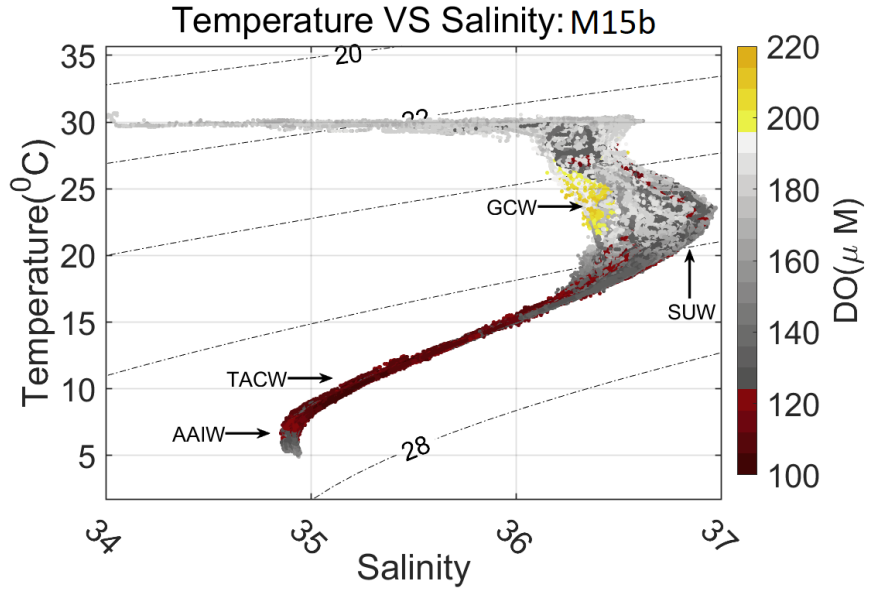

Figure 4.12: The temperature-salinity diagrams are shown for CTD data collected by M15b around the LC and LC periphery. The black contour lines show the isopycnals in kgm^{-3}. The colors represent dissolved oxygen concentrations.

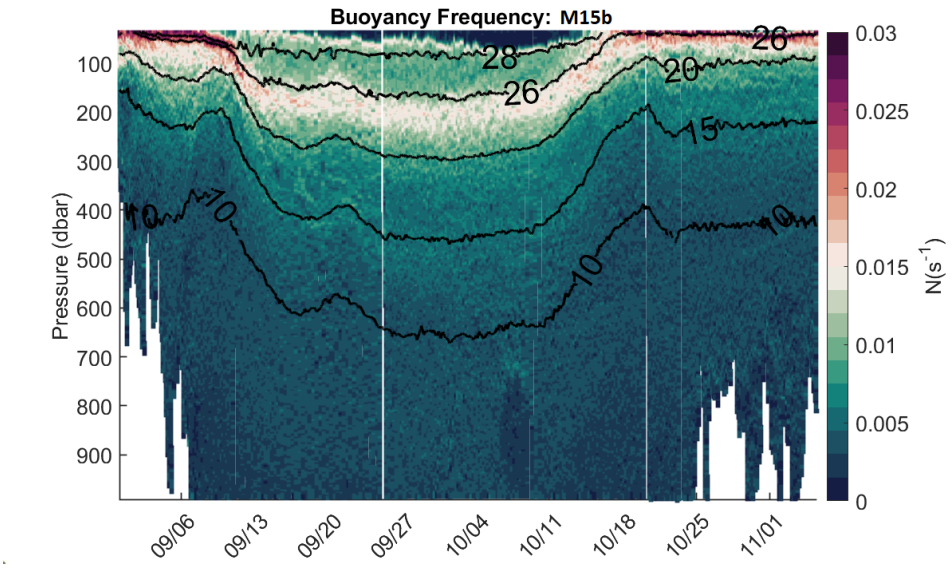

Figure 4.13: Hovmöller plot of Brunt-Väisälä frequency as a function of pressure and time form estimated from data collected by M15b deployed in 2015 in the northwestern Gulf of Mexico. A strong stratification strip surrounding the core is observed.

4.5 Result and discussion

4.5.1 Oceanographic Vertical Velocity Estimation within LC structures

The Hovmöller diagram of the vertical velocity of the water from M15a is shown in Fig.4.14. The estimated vertical velocity of water from M15a shows a coherent horizontal (temporal) structure aligned with the isopycnals. The vertical (depth) structure of the vertical water velocity shows the existence of alternating layers water masses. which have been previously associated with upwelling and downwelling processes, e.g., from moored ADCP measurements (Rivas et al., 2008).

The eddy core has predominantly negative vertical velocities, which is the well-observed characteristic of an anticyclonic eddy (Flierl and Mied, 1985). In the upper pycnocline between $1025 - 1028\,kg\,m^{-3}$, depth around $350\,m$ and >$700\,m$ positive vertical velocities were found to dominate and indicate upwelling favorable conditions. Such upwelling events have been related to the presence of an anticyclonic eddy (Nowlin Jr et al., 2000). Intensification of upwelling around the eddy periphery is also observed (Fig. 4.14) and may be associated with submesoscale insta-

bility (Brannigan, 2016). Beneath the upper thermocline, weak negative vertical velocities were observed, i.e., $\approx 200 - 700\,m$.

The Hovmöller diagram of the vertical velocity of the water from M15b is shown in Fig.4.15. The structure of vertical water velocity observed from M15b is consistent with the observations of M15a. However, the intensity of elevated upwelling around the edge (isopycnals between $1025 - 1027\,kg\,m^{-3}$) of the LC is significantly higher than LCE, which may be associated with the elevated geostrophic shear and higher swirl velocities associated with the more energetic LC (Fig. 4.21).

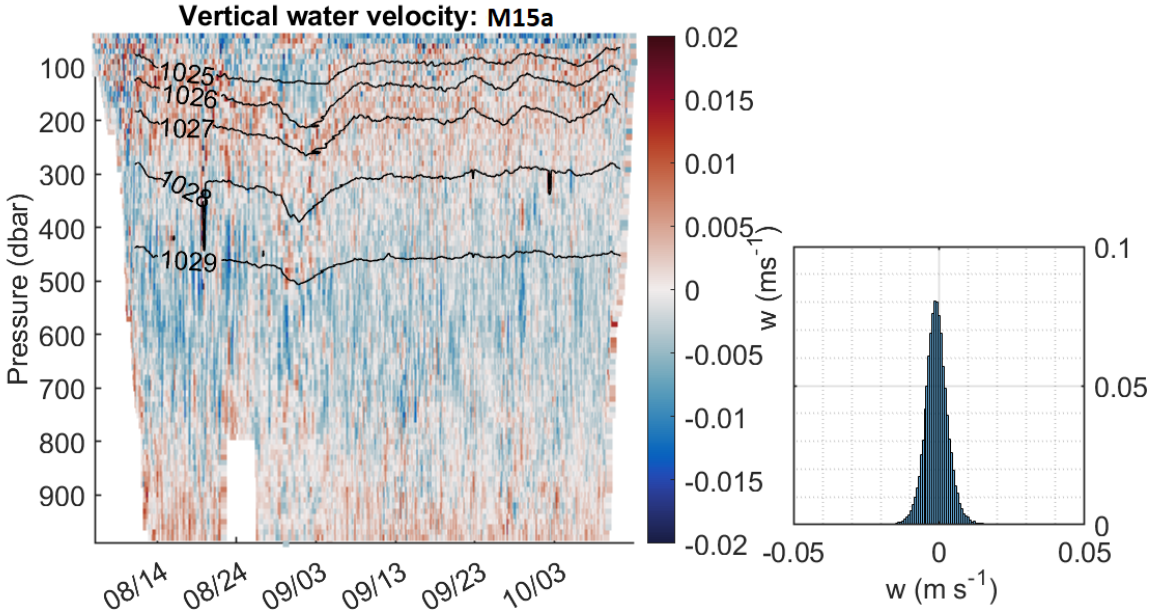

Figure 4.14: Hovmöller plot of estimated vertical current velocity as a function of pressure and time form data collected by M15a deployed in 2015 in the northwestern Gulf of Mexico. The black lines represent the density contour.

The estimated mean vertical velocity of water from M15a and M15b are $-7.8 \times 10^{-4}\ m\,s^{-1}$ and $-6.7 \times 10^{-4}\ m\,s^{-1}$, respectively; however, these small values are statistically different from zero. The histogram is symmetrical and normally distributed around the mean with a maximum velocity exceeding $\pm 0.04\ m\,s^{-1}$ at the surface (Fig. 4.14 and 4.15). That symmetrical shape

of the distribution of the vertical water velocity is expected in the presence of the internal wave (Merckelbach et al., 2010). The RMS of vertical water velocity is $0.0052\, m\, s^{-1}$ for both glider missions (M15a and M15b). Estimated noise variance suggests that the error associated with the vertical water velocity estimation are $0.0022\, m\, s^{-1}$ and $0.0021\, m\, s^{-1}$, respectively. These findings are consistent with the findings of moored ADCP measurement in the GoM (Rivas et al., 2008).

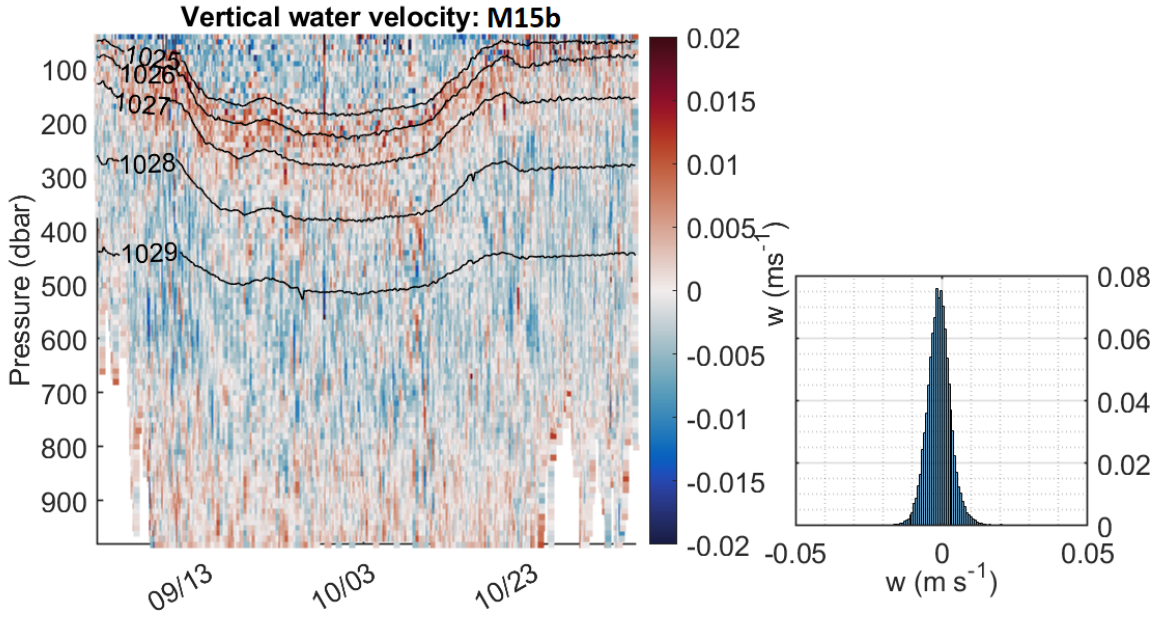

Figure 4.15: Hovmöller plot of estimated vertical current velocity as a function of pressure and time form data collected by M15b deployed in 2015 in the northwestern Gulf of Mexico. The black lines represent the density contour.

4.5.2 Mixing due to turbulence

4.5.2.1 Survey-averaged profiles

Here, we applied the glider-based estimation of TKE dissipation rates described in section 2.2 and constructed time-space map of turbulence in the northwestern GoM. In order to estimate TKE dissipation rates, the value of C_ϵ in Eq. 2.1 must be determined by comparison with the Thorpe Scale (TM) dissipation rate. Survey-averaged profiles using Eq. 2.1 and Thorpe Scale

(TM) dissipation rate using Eq. 2.9 were constructed by averaging the data from entire mission in 10-m depth bins. A linear least-squares fit between the survey-averaged profiles using equation 2.1 and TM dissipation rate produced the proportionality constant $C_\epsilon = 0.5215$ and 0.4788 for the LCE and LC glider missions, respectively. These values are consistent with the reported value in section 3.4.1 and previous studies using equation 2.1, for example $C_\epsilon = 0.37$ in Beaird et al. (2012), $C_\epsilon = 0.3 - 0.6$ in D'Asaro and Lien (2000b).

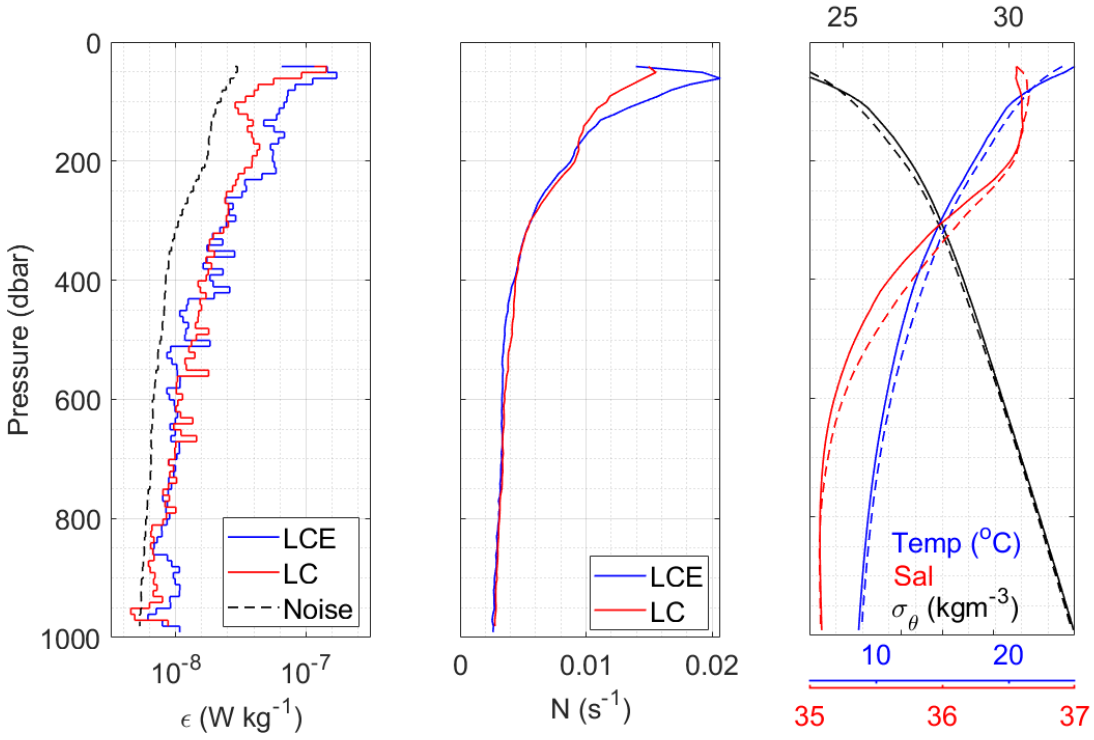

Figure 4.16: Survey averaged profiles (a) ϵ of LCE (blue) and LC (red) and noise level/lowest detection level of LEM (black), (b) Brunt-Väisälä frequency (N), (c) temperature (blue), salinity (red) and potential density (black). The solid and dashed line in d represent LCE (M15a) and LC (M15b), respectively.

The survey-averaged profiles of glider estimated TKE dissipation rates (ϵ) for LCE (M15a) and LC (M15b) missions are shown in (Fig. 4.16 a). The survey-averaged profiles for LCE and LC co-vary below depth $\approx 250\,m$ (Fig. 4.16 a). Both survey-averaged profiles captured the

quiescent nature of Gulf of Mexico outside of the LCE and LC core in the upper water-column, i.e., between $\approx\ 60\ -\ 250\,m$ (Fig. 4.17 and 4.18); however, the lower average value within the LC reflects a longer mission length, and therefore more observation, in and around the LC core ($\approx\ 41$ days) compared to LCE core ($\approx\ 10$ days). A similar effect of averaging is noticeable in the survey-averaged Brunt-Väisälä frequency (N) profiles (Fig. 4.16 b). The noise level and the lowest detection limit of the estimated TKE dissipation rate using the vertical velocity noise $w_{noise} \approx\ 0.002\,m\,s^{-1}$ (Fig. 4.16 a, black dashed line).

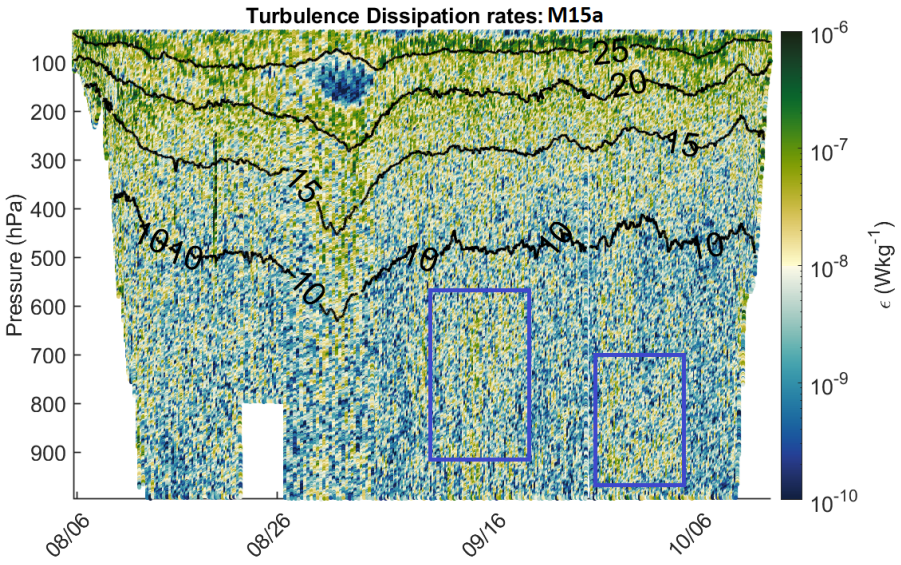

Figure 4.17: Hovmöller diagram of estimated ϵ) from data collected during M15a in the north-western Gulf of Mexico. Blue boxes are identifying location of elevated ϵ) in deep water (> 600 m).

4.5.2.2 Characterization of Turbulent mixing within the Loop Current Eddy

The M15a glider's hydrography, buoyancy frequency (N), and TKE dissipation rates (ϵ) underline the structure of LCE within the water column (Fig. 4.17). The estimated (ϵ) (Fig. 4.17) ranges from 10^{-11} to $10^{-6}\ Wkg^{-1}$ (Fig. 4.19). The largest (ϵ) ($order\ of\ 10^{-6}\ Wkg^{-1}$) are observed in the surface layer. The relatively large (ϵ) in the surface layer is attributed to surface boundary

layer processes like winds, waves, and buoyancy forcing (MacKinnon et al., 2016). Below the surface layer (> 50 m), elevated (ϵ) ($order\,of\,10^{-7}\ Wkg^{-1}$) is observed at depths between ≈ 50 and $350\,m$, where the vertical gradient of temperature, salinity, and density are highest. Large temperature and salinity gradients associated with elevated (ϵ) indicate heat and salt transfer from the eddy's core into the surrounding water (Fine et al., 2018). Though high dissipation ($order\,of\,10^{-7}\ Wkg^{-1}$) is observed around the LCE core, the core interior is relatively quiescent. The well-mixed core interior reflects the movement of the Atlantic Ocean water mass into the Gulf interior and that the water mass is mixed from the outside first. This interpretation is consistent with the understanding that separated LC eddies weaken and dissipate as they move from east to west in the Gulf of Mexico. This is further evidenced by the observation of M15a and weaker gradients of density, temperature, and salinity surrounding the western LCE core.The magnitude of the dissipation rate at the core is order $order\,of\,10^{-10}\ Wkg^{-1}$ and is consistent with previously reported direct microstructure observations (using MicroRider) within an LCE in the GoM (Molodtsov et al., 2020). Beneath the LCE core, high dissipation aligned with the deepened isotherm; reaching to $600\,m$ depth. Some elevated turbulence patches were observed at greater depth (Fig. 4.17 blue box), which may be a result of breaking and interaction waves (internal wave, shelf wave) with a steep slope and rough topography of continental slope of GoM. The histograms of observed dissipation rates from M15a and M16b (Fig. 4.19) show remarkably similar structure and range and indicate that the physical processes that contribute to mixing in the Gulf interior are similar in the eastern and western parts of the basin.

4.5.2.3 Characterization of Turbulent mixing at the edge of and within the Loop Current

TKE dissipation rates (ϵ) from the LC extension region are shown in Fig. 4.18. The $26°C$ isothermal line defines the position of the LC temperature core. Although the magnitude and the structure of turbulence of LC are very similar to the turbulence structure of LCE, some key differences are apparent. Relatively low ϵ ($order\,of\,10^{-9}\ Wkg^{-1}$) are found at the LC core compared to the surrounding of the core; however, patches of elevated ϵ ($order\,of\,10^{-9}\ Wkg^{-1}$) are also found at the core near the surface boundary layer. This is attributable to a more weakened structure in the

western regime (where the water mass had longer times to interact with the Gulf's interior) than the relatively recent intrusion of the LC core. Beneath the LC core, relatively large dissipation rates are aligned with the deepened isotherm and reach the bottom of the survey depth (i.e., to $1000\,m$). Elevated dissipation is also observed at the eddy edges (i.e., the sloping isolines shown in blue outline), reaching up to $700\,m$ depth (Fig. 4.18).

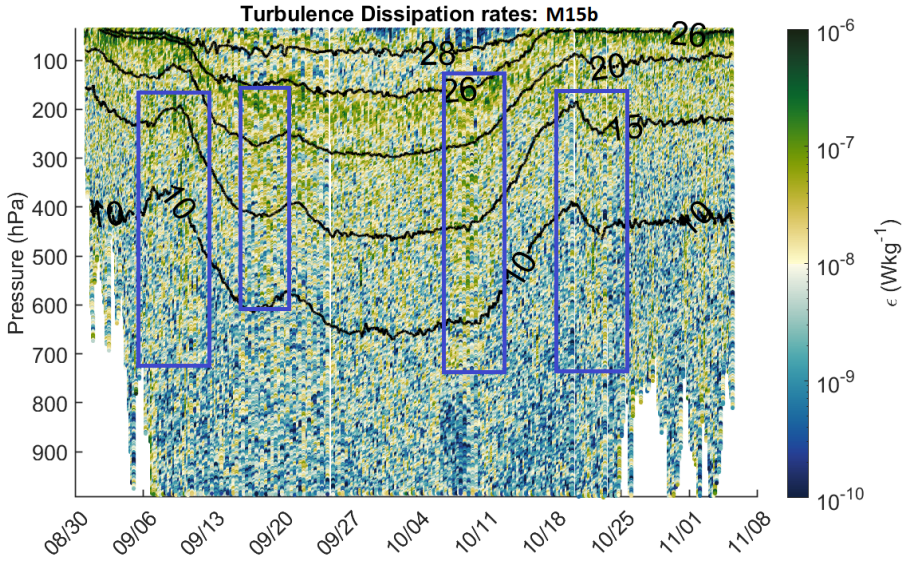

Figure 4.18: Hovmöller diagram of estimated ϵ from data collected (M15b) in the northwestern Gulf of Mexico. Blue boxes are identifying LC induced elevated ϵ in depths (200 to $700\,m$) associated with the deep eddy fronts.

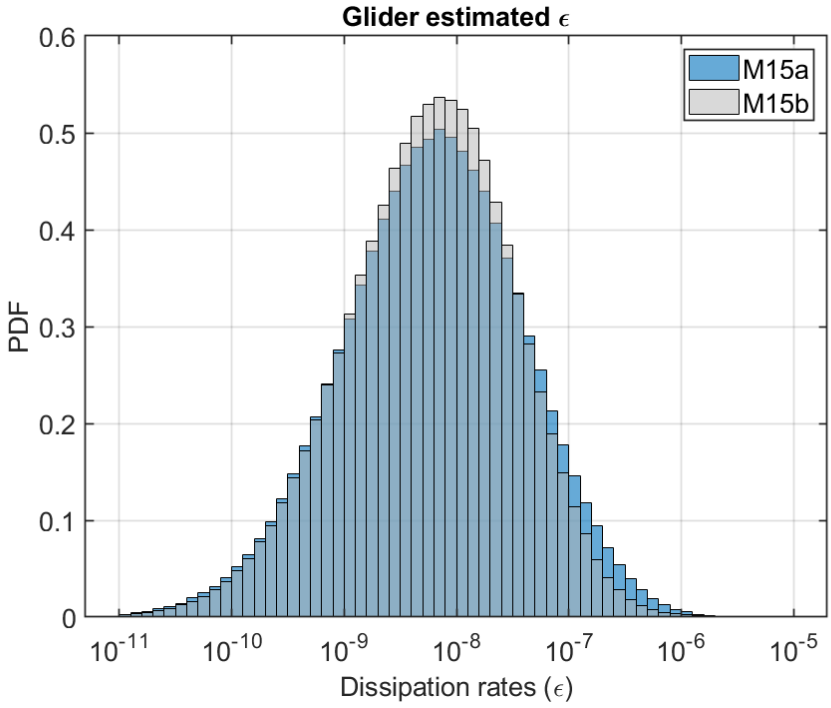

Figure 4.19: Probability density functions (PDFs) of ϵ from glider M15a (blue) and M15b (gray)

4.5.2.4 Shear induced turbulence

The velocity data from altimetry shows geostrophically-derived surface currents exceed $1m\ s^{-1}$ (Fig. 4.2 and 4.3). To assess the effect of velocity shear on the turbulence structure qualitatively, we calculate the along-track geostrophic shear from the glider profiles (the gliders do not have direct current velocity measurement capability). The along-track geostrophic velocity shear calculated using the thermal wind Eq. 4.2 from M15a and M15b is shown in Fig. 4.20 and Fig. 4.21 respectively. Because the LCE was anticyclonic, the positive geostrophic shear is defined as the flow direction to the left of the glider track and vice versa.

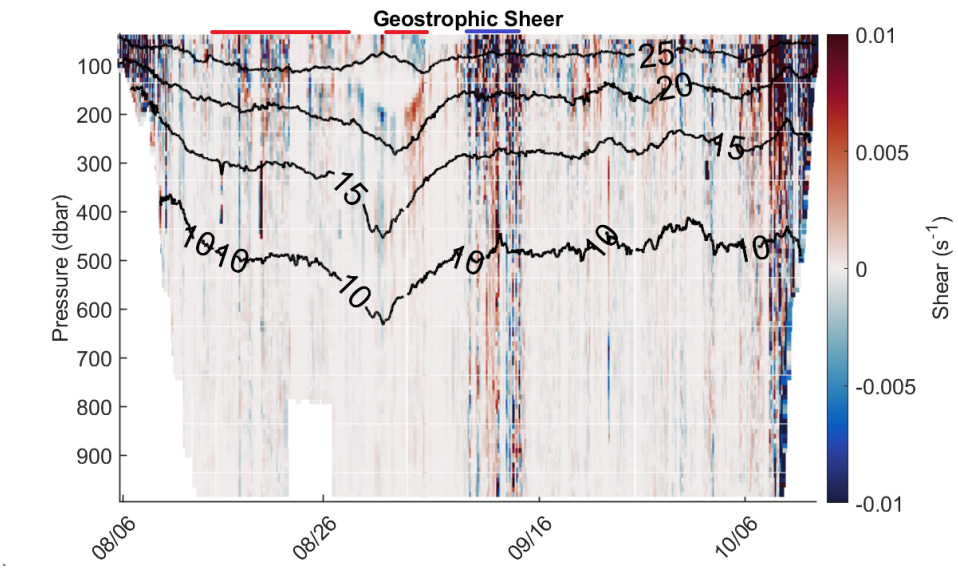

Figure 4.20: Hovmöller plot of along track geostrophic shear calculated using thermal wind equation from data collected M15a. Red, purple, blue bars at the top of the graph denote times when the glider was near the eddy front and within the eddy core.

Elevated geographic shear, i.e., larger values, is observed at the edge of the eddies during the gliders entering and exiting LCE and LC (indicated as colored bars at the top of the graph, i.e., over sloping isopycnals, Fig. 4.20 and Fig. 4.21). The observed elevated dissipation rate is coincident with high shear values in for LCE (M15a) (Fig. 4.20) and LC (M15b) (Fig. 4.21). At the LCE and LCE periphery strong geographic shear is observed. Additionally, elevated shear and dissipation rates are observed around and beneath the core (Fig. 4.20 and Fig. 4.21).

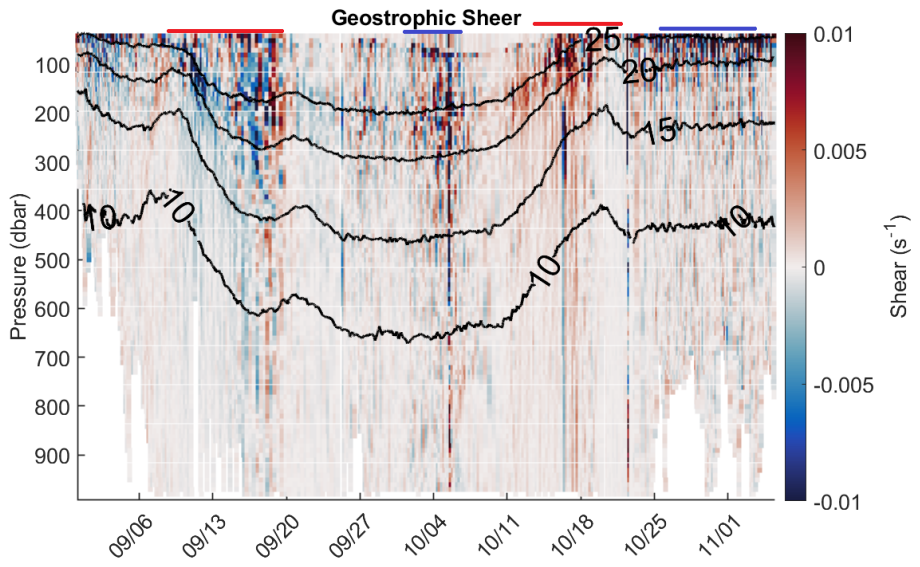

Figure 4.21: Hovmöller plot of along track geostrophic shear calculated using thermal wind equation from data collected M15b. Red, purple, blue bars at the top of the graph denote times when the glider was near the eddy front and within the eddy core.

4.5.2.5 Diapycnal eddy diffusivity within the LC and LCE

The estimated diapycnal eddy diffusivity (k_ρ) for LCE is shown in Fig. 4.22. The k_ρ is calculated from estimated ϵ using the Eq. 4.1. The k_ρ (Fig. 4.22) shows a coherent horizontal structure aligned with stratification (Fig. 4.8). Eddy diffusivity (k_ρ) is relatively high ($order\ 10^{-4}\, m^2\, s^{-1}$) in the surface mixed layer ($\approx\ 50\, m$), where the stratification is relatively low. Beneath the surface mixed layer, the upper thermocline is the layer of ($\approx\ 50\ -\ 200\, m$) strong stratification. Although the TKE dissipation rate (ϵ) is relatively high in the upper thermocline, the k_ρ is found to be weak ($order\ 10^{-5}\, m^2\, s^{-1}$). Because k_ρ is normalized by the Brunt-Väisälä frequency (N), the strong local stratification suppresses the vertical mixing (Wang et al., 2016). The LCE core appears to be well mixed with weak k_ρ ($order\ 10^{-5}\, m^2\, s^{-1}$) where weak ϵ was observed at. Below $300\, m$, the stratification and ϵ are relatively weak and relatively strong k_ρ are observed within the order of 1×10^{-4} to $5 \times 10^{-4}\, m^2\, s^{-1}$. Patches of elevated k_ρ is observed in deep water and is coincident with the previously described elevated ϵ patches. The average k_ρ for the entire survey is order $1 \times 10^{-4}\, m^2\, s^{-1}$, and compares well with previously reported values (Molodtsov et al., 2020).

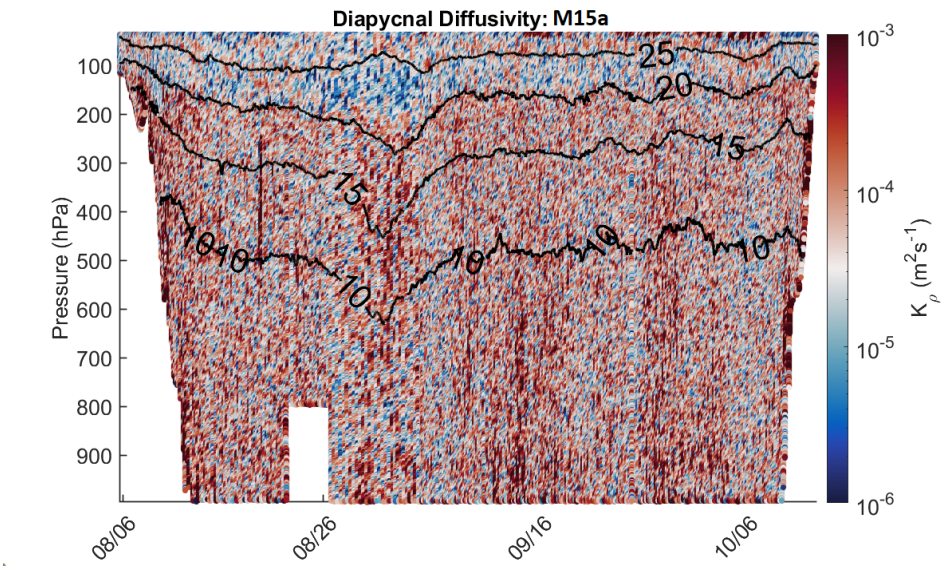

Figure 4.22: Hovmöller diagram of estimated diapycnal diffusivity k_ρ from M15a in the northwestern Gulf of Mexico.

Fig. 4.23 shows the observed M15b diapycnal eddy diffusivity (k_ρ) near the LC and LC periphery. The structure of k_ρ of LC is similar to the LCE with the magnitude of k_ρ ranges within the order of $1 \times 10^{-}3$ to $5 \times 10^{-4}\, m^2\, s^{-1}$. The largest observed k_ρ is found in the surface mixed layer, which indicate the presence of boundary layer processes. Elevated k_ρ patches consistent with the elevated ϵ patches and geostrophic shear are found in deep water. However, regions with larger ϵ and geostrophic shear (LC edge) show low k_ρ values, resulting from the strong local stratification of the LC edges, and suppressed vertical mixing (Wang et al., 2016).

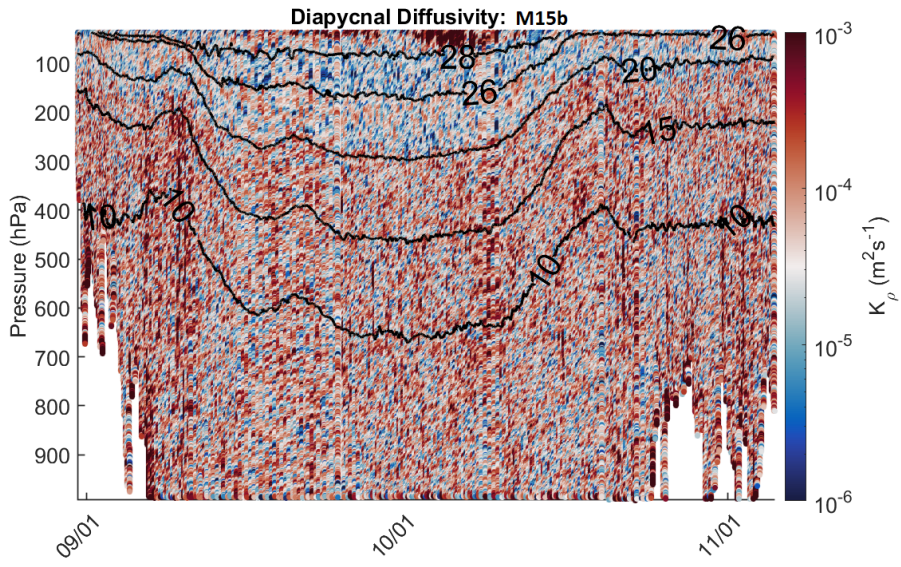

Figure 4.23: Hovmöller diagram of estimated diapycnal diffusivity k_ρ from M15b in the north-western Gulf of Mexico.

4.5.3 Characterizing LC and LCE Mixing using Turner Angle

The diffusion processes in the water-column can be characterized using the Turner Angle (Tu) (Eq: 4.4). Fig. 4.24 shows the Turner Angle estimated from the temperature and salinity for M15a. Diffusion regimes are color-coded based on the stability condition defined by the magnitude of the Tu. Dark blue identifies gravitationally unstable; light blue and green identify salt fingering; purple identity stable water mass; and yellow and red identify diffusive convection. The criteria of double- diffusive regimes of water masses based on Turner Angle are given in Table: 4.1.

The Turner Angle plot shows that identified diffusive regimes in the GoM are aligned with the isothermal lines (Fig. 4.24). However, the stable high salinity water associated with well mixed water masses of the LCE core is confirmed, i.e., the temperature core of LCE is dominated by stable water mass. Most water masses with temperature >$18°C$ (upper $\approx$ $150\,m$) and temperature <$7°C$(below $\approx$ $800\,m$) are stable (Purple shading: $-45 \leq Tu \leq 45$).

Between temperature $7°C$ and $18°C$ (depth $\approx$ 150 to $800\,m$), Tu is between $45°$ and $90°$ (light blue shading: strong salt-fingering, green shading: weak salt-fingering), indicating salt-fingering

favorable conditions. Between that depth, warm-salty SUW overlies relatively cold-fresher TACW and AAIW, which creates favorable conditions for salt-finger formation (Molodtsov et al., 2020; Meunier et al., 2019). Salt-fingering in a similar water mass was reported in western tropical North Atlantic near the Lesser Antilles (Fer et al., 2010). On the edge and the lower boundary of LCE (blue box in Fig. 4.24), alternating layers of warm-salty and cold-fresh water are found. Closer examination of Tu shows the water masses in this region has alternating values of Tu between $72 < Tu < 90$ (salt-fingering) and $-90 > Tu > -45$ (diffusive convection). Such alternating layers of salt-fingering and diffusive convection regions have previously be associated with thermohaline intrusion Fine et al. (2018); Molodtsov et al. (2020). The identified regions (blue box in Fig. 4.24) are at eddy frontal boundaries, where water warmer-salty LCE waters exist next to relatively cold-fresh water and creating favorable conditions for intrusion. The salinity profiles color plotted with the temperature of the identified thermohaline intrusion regions in the LCE is given in Fig. 4.26. The coherent structure of alternating layers of cold–fresh and warm–salty water mass across multiple profiles is further evidence of the intrusions.

Fig. 4.25 shows the Turner Angle (Tu) estimated from the temperature and salinity for M15b. The Tu plot shows a similar distribution of the diffusive regimes as M15a; however, the direct LC influence on temperature and salinity distribution of the identified double-diffusive regimes is more pronounced.

Inside the LC, stable water mass (purple shading: $-45 \leq Tu \leq 45$) in the surface were found above the $23°C$ (upper $\approx$ $250\,m$). The depth of the stable water mass regime inside the LC is $\approx$ $100\,m$ deeper compared to the outside of the LC. Additionally, evidence of diffusive layers ($-45° < Tu < -90°$) was found inside that layer, resulting from increasing temperature and salinity with depth inside the eddy (Fine et al., 2018). Between $18°C$ and $23°C$ (depth $\approx$ 250 to $350\,m$), the Tu is between $45°$ and $72°$ (green shading), indicating weak salt-fingering conditions. The salinity plot (Fig. 4.10) shows that the high salinity core of the LC (SUW, salinity > 36.5) is located in that identified region. Weak salt-fingering (Green shading: $72° < Tu < 72°$) is found between 18◦C and 9◦C isotherm. Below < $7°C$ isotherm is dominated by stable water mass.

However, between $7°C$ and $9°C$ isotherms, water masses are prone to salt-fingering and diffusive convection, which indicates that the formation of stable water mass is through double diffusion. Similar to M15a, thermohaline intrusions were found around the edge of the LC. Location of a thermohaline intrusion region is shown as blue boxes in Fig. 4.25 and corresponding salinity profiles are shown in Fig. 4.27.

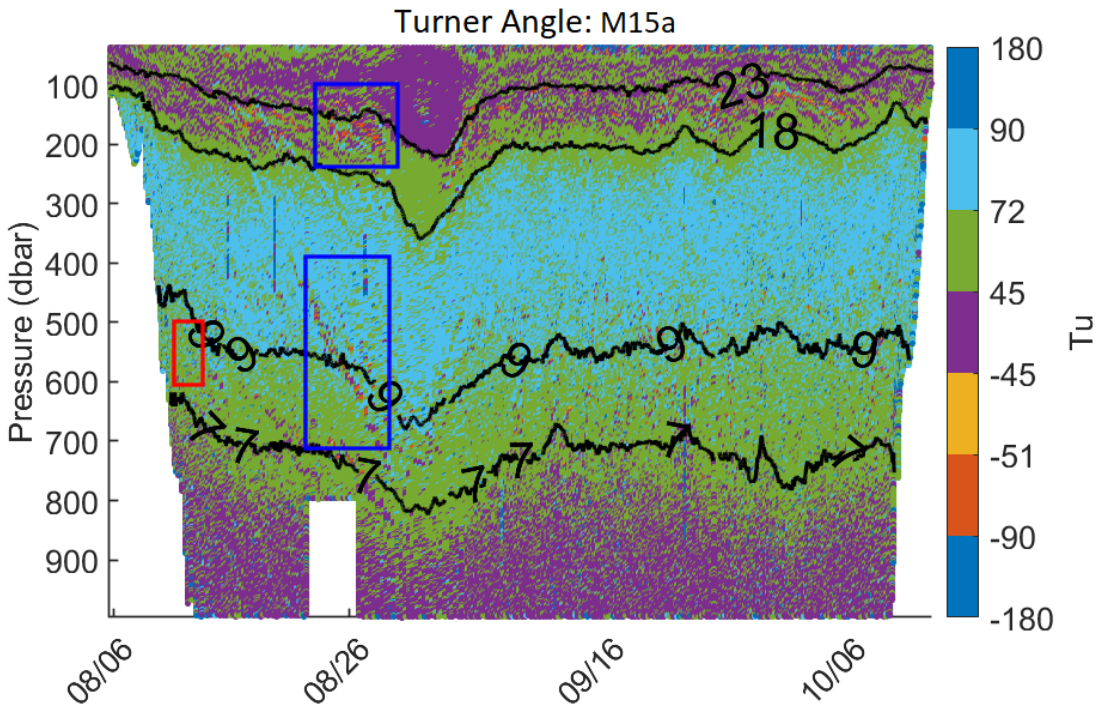

Figure 4.24: Turner angle from M15a. The blue boxes showing the location of diffusive- convective layer and green box show the location of observed themohaline staircase.

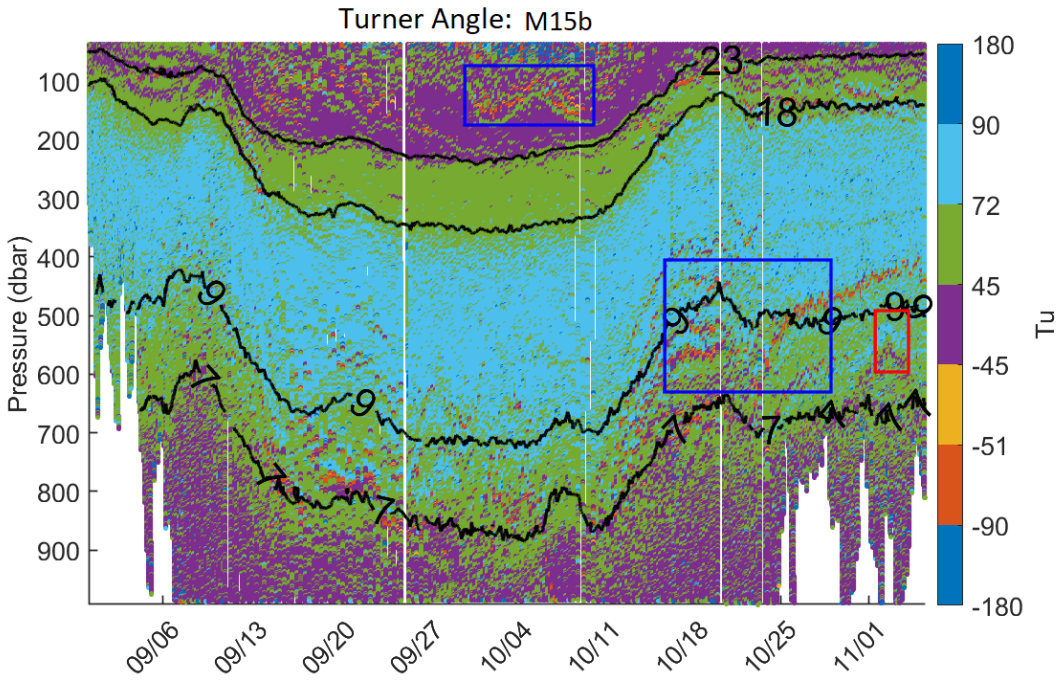

Figure 4.25: Turner angle from M15b. The blue boxes showing the location of diffusive- convective layer and green box show the location of observed themohaline staircase.

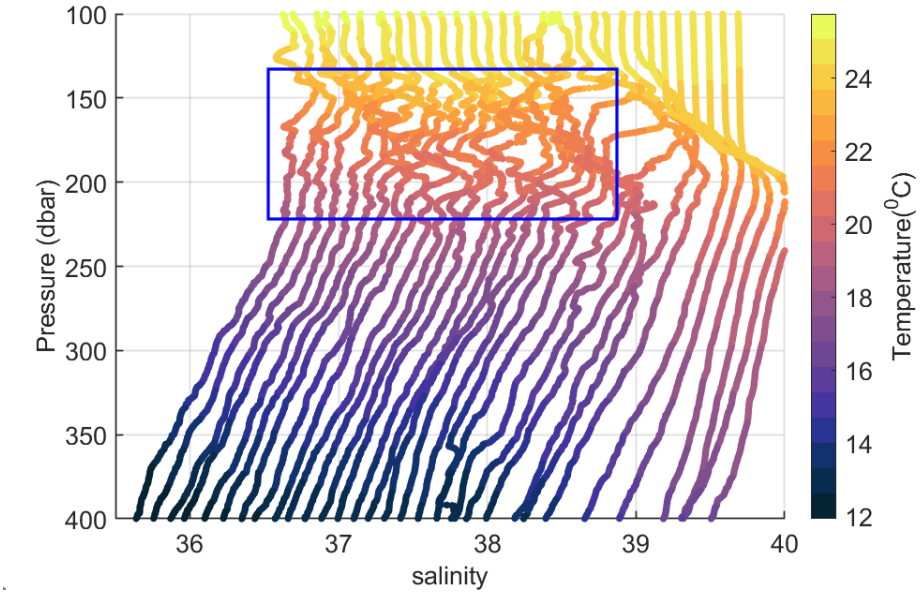

Figure 4.26: Salinity profiles of thermohaline intrusion is observed from M15a. The colors represent temperature. Salinity profiles are offset by 0.05 to avoid overlap and to illustrate the temporal and spatial evolution of the profiles.

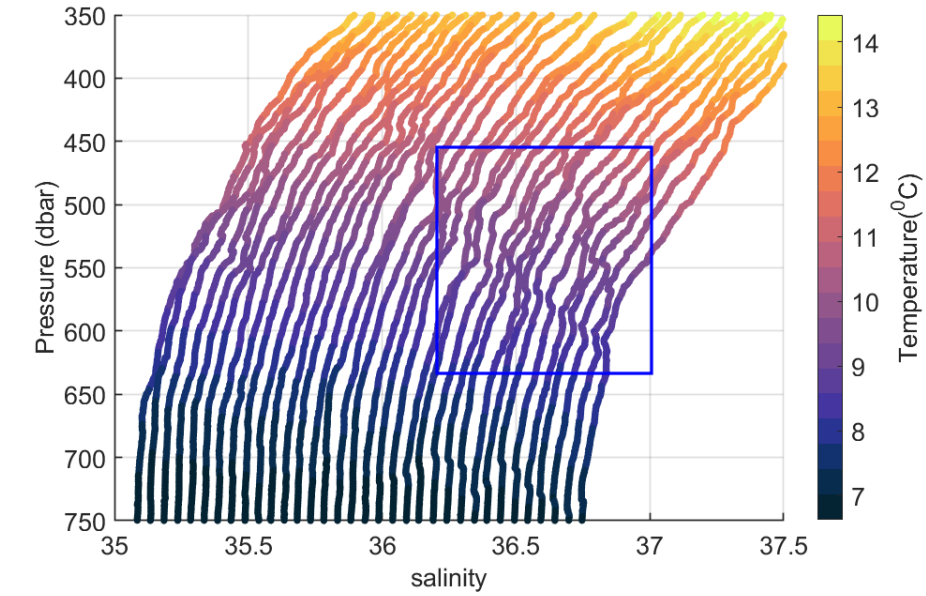

Figure 4.27: Salinity profiles of thermohaline intrusion is observed from M15b. The colors represent respective temperature. Salinity profiles are offset by 0.05 to avoid overlap and to illustrate the temporal and spatial evolution of the profiles.

To characterize the vertical structure of diffusion more fully, the glider data were treated as individual segments (section 4.4.1). Fig. 4.28 to Fig. 4.30 shows the polar plot of Turner Angle (Tu) as a function of temperature colored with salinity (left panel), PDF of Tu as a function of temperature (middle panel), and eddy diffusivities (right panel). Eddy diffusivity of salt (k_s) and heat (k_θ) are calculated using Eq. 4.5 and Eq. 4.6, respectively for density ratio $R_\rho = 1.6$ and $\gamma = 0.7$. Fig. 4.28 represent the data from M15a before entering LCE, Fig. 4.29 represent inside of the LCE and, Fig. 4.30 represent glider data after exiting the LCE.

The polar plots provided an enhanced and composite representation of Tu values to identify diffusive processes at different temperature regimes. The polar plots show that surface water (temperature >$20°C$) and bottom water (temperature <$7°C$) are dominated by stable water mass ($-45°$ <Tu <$45°$); however, salt-fingering favorable condition ($72°$ <Tu <$90°$) dominates temperature between $18°C$ to $7°C$. Generally, that water mass stability was observed in all data segments. When the glider was inside the LCE, a large volume of stable ($-45°$ <Tu <$45°$) water mass is observed for temperature > $18°C$. The salinity value associated with that water mass is > 35.5, indicating that water mass consists of SUW associated with the LCE core. Additionally, a small number of diffusive-convection prone water mass was found between temperatures $20°C$ and $25°C$ when the M15a was inside the LCE and after exiting the LCE.

The Tu PDF (probability density represented as a histogram) showed a multimodal distribution, i.e., the presence of multiple diffusion favorable processes, of the stable water mass when the glider was outside (Fig. 4.28 and Fig. 4.29) of LCE. Alternating layers of stable and salt- fingering prone water masses are observed above the $20°C$ isotherm (Fig.4.24). However, inside the LCE, Tu PDF of stable water masses peaks around $27°C$. This peak represents the water mass of the stable LCE core observed in M15a (4.29) .

Between $18°C$ and $23°C$, the percentage of salt-fingering favorable conditions increases. This increase represents the water mass associated with the SUW under the LCE core. Additionally, a small volume of diffusive- convection prone water mass between temperature $18°C$ to $23°C$ and deep water identifies the thermocline intrusion (Fig. 4.24). A small percentage of unstable and

diffusive convection favorable water masses are found near the surface (Fig. 4.30). Hovmöller plot of Tu (Fig. 4.24) shows that water mass on the surface were encountered after September 16, 2015, when the glider was sampling the LCE periphery. By that period, the LCE started to spin down and decay, diffusing warm and salty SUW to the background GCW, i.e., another indication of unstable and diffusive convection water masses near surface.

The estimated diffusivities show different relative diffusivities for heat(k_θ) and salt(k_s), which is expected in under salt-fingering favorable conditions (Schmitt, 2003). The diffusivities (k_ρ k_s, and k_θ) at the surface are relatively lower than at depth, indicating less mixing in the more stable water masses. Additionally, higher diffusivity associated with the unstable and diffusive convection-favorable water masses is observed at the surface after M15a exited the LCE.

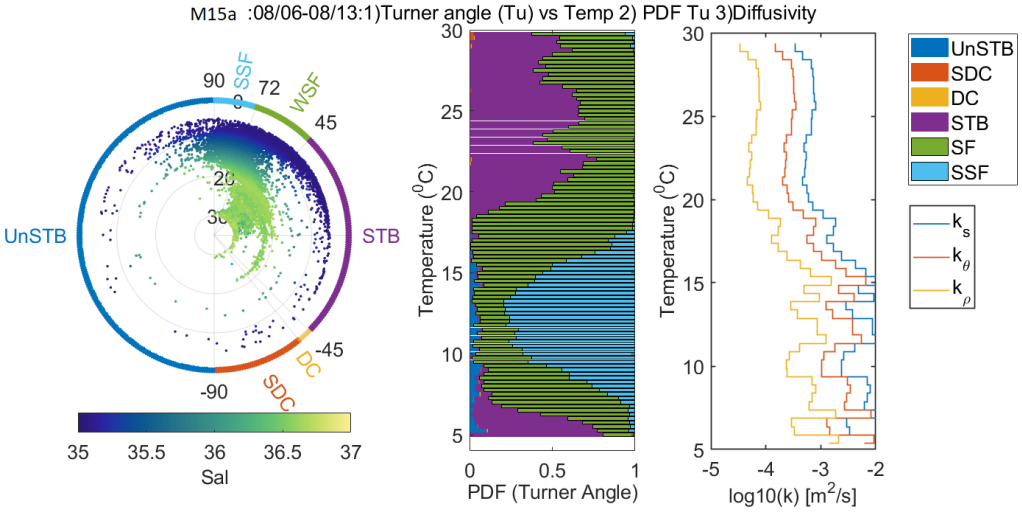

Figure 4.28: Polar plot of Tu (left: radius is observed temperature; diffusion class is labeled along the circumference); PDF histogram of Tu as function of temperature (middle) and estimated diffusivities for salt-fingering condition for M15a near LCE front 08/06/2015 - 08/13/15.

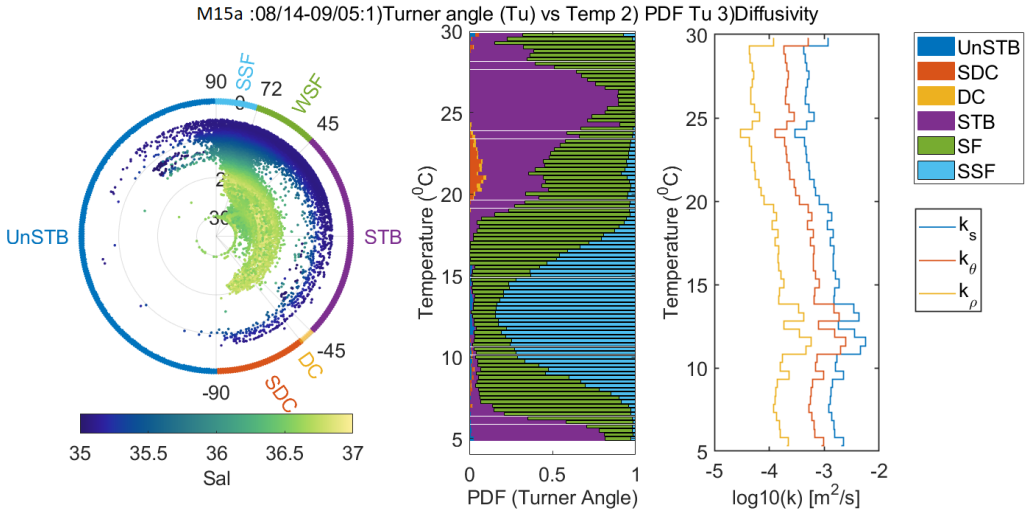

Figure 4.29: Polar plot of Tu (left, radius is observed temperature; diffusion class is labeled along the circumference), PDF histogram of Tu as function of temperature (middle) and estimated diffusivities for salt-fingering condition. M15a close to LCE core between 08/14/2015 - 09/05/15.

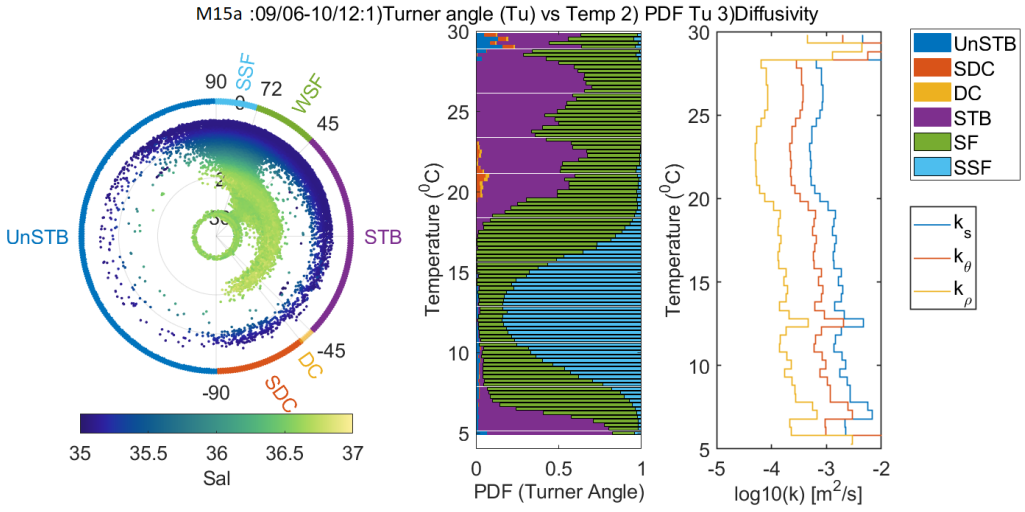

Figure 4.30: Polar plot of Tu (left, radius is observed temperature; diffusion class is labeled along the circumference), PDF of temperature as a function of Tu (middle) and estimated diffusivities for salt-fingering condition. M15a outside LCE, 09/06/2015 - 10/12/15.

Fig. 4.31 to 4.35, are a sequence of five plots depicting the glider at different dynamical po-

sitions along the LC region. As with figure 4.28 to 4.30, the plots have three panels: polar representation of Tu (left panel), PDF histogram (middle panel), and eddy diffusivities as a function of temperature (right panel). Fig. 4.31 M15b before entering LC, 4.32 represents over the inclined isoline at the LC edge, Fig. 4.33 inside the LC, Fig. 4.34 over inclined isoline during transit out of the LC and, Fig. 4.35 after exit out of LC and sampling around the edge of the LC.

The Tu plot and PDF of the LC (M15b) mission show similar general patterns of water mass stability and diffusive processes as the LCE (M15a) mission. However, the LC observations are more pronounced details than the LCE mission. The polar plots in Fig. 4.31 show that surface ocean (temperature > $20°C$) and deep ocean (temperature < $7°C$) are dominated by stable water masses ($-45°$ < Tu <$45°$). Salt-fingering favorable conditions ($72°$ < Tu < $90°$) dominate at intermediate depths (temperature between $18°C$ to $7°C$ and similar to vertical structure outside the western LCE). When the glider was at the edge LC (Fig. 4.32 and Fig. 4.34), a large volume of stable ($-45°$ < Tu < $45°$) water mass is observed for temperature > $18°C$. The salinity value (>35.5) indicated that water mass is associated with the LC. Additionally, a small number of diffusive-convection ($-90°$ < Tu < $-45°$) favorable water masses is found at temperatures > $17°C$. Inside the LC (Fig. 4.33), the stable water mass was observed above the $\approx 23°C$ isotherm, and salt-fingering favorable ($72°$ < Tu < $90°$) water mass layer extend temperature between $23°C$ to $7°C$. Diffusive-convection prone water masses was also found at temperature > $17°C$. As M15b exits the LC, the salinity value indicates the strong presence of GCW and SUW.

The PDF of Tu outside (Fig. 4.31) of the LC shows the presence of multiple diffusive processes of stable water mass and salt-fingering as observed in the LCE mission. Alternating layer of stable and salt-fingering prone water mass above the $20°C$ isotherm (Fig.4.25). At the edge of the LC (Fig. 4.32 and Fig. 4.34), Tu PDF of stable water mass and salt-fingering favorable water is similar to LCE core,i.e., stable water mass peaks at $27°C$ and salt-fingering favorable water masses increased between $18°C$ to $23°C$ due to the strong oceanographic front (increased property gradients, strong velocity shear, etc.) near the LC front and LC core.

Diffusive convection-favorable water masses are observed at the frontal edge indicating ther-

mohaline intrusion (Schmitt et al., 1986; Molodtsov et al., 2020). Inside the LC (Fig. 4.33), the structure is different than outside the LC. Here, the Tu PDF for stable water masses peaks around $24°C$ and only found at temperature > $23°C$, i.e., the highly stratified LC core. Unstable and diffusive convection-favorable water masses are observed above the $\approx 25°C$ isotherm (Fig. 4.33). Above the LC core, temperature and salinity increase with depth, providing favorable conditions for diffusive layering. A similar finding was reported in an anticyclonic warm-core in the Canada Basin (Fine et al., 2018). The high salinity core of the LC is found between $18°C$ and $23°C$ isotherm (Fig. 4.10). The Tu distribution of the salinity core shows a significant difference from other survey locations. At these temperatures, weak salt-fingering conditions dominate the water mass.

The estimated diffusivities show expected (Schmitt, 2003) different magnitudes for heat(k_θ) and salt(k_s). The diffusivities (k_ρ k_s, and k_θ) at the surface are relatively less than at depth, indicating lower mixing in the stable water mass. The low magnitude diffusivities is observed at the LC core. Higher diffusivity is associated with the unstable and diffusive convection favorable water masses near-surface and above the core.

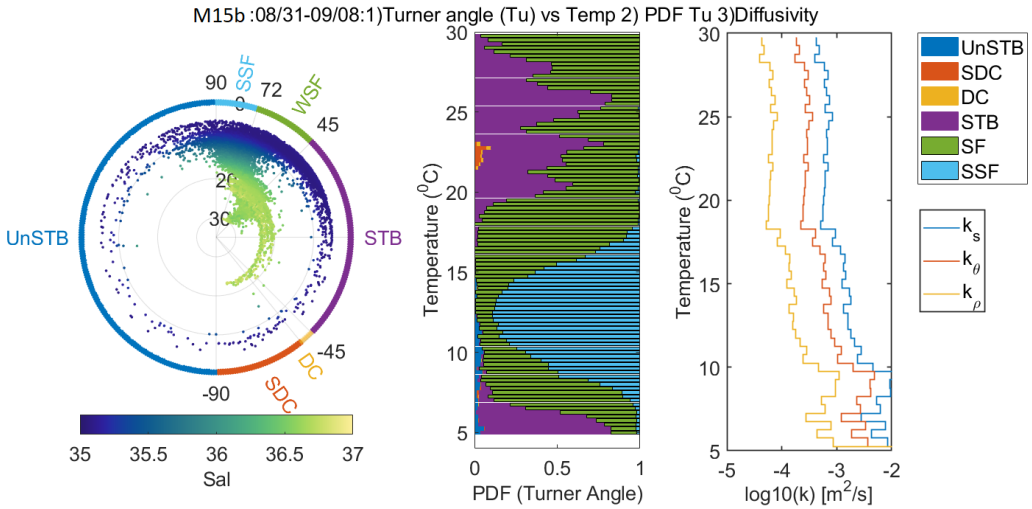

Figure 4.31: Polar plot of Tu (left, radius is observed temperature; diffusion class is labeled along the circumference), PDF of temperature as a function of Tu (middle) and estimated diffusivities for salt-fingering condition. M15b before entering LC, 08/31/2015 - 09/08/15.

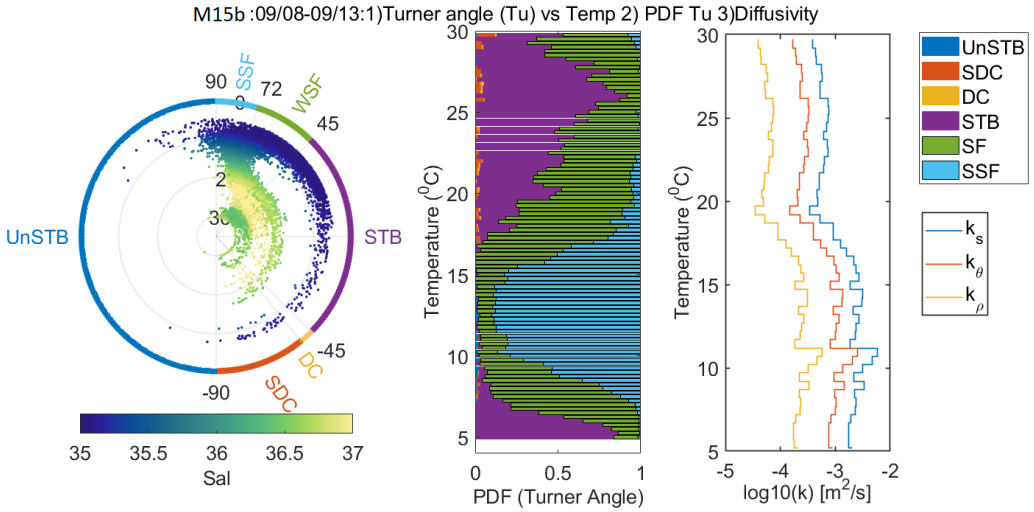

Figure 4.32: Polar plot of Tu (left, radius is observed temperature; diffusion class is labeled along the circumference), PDF of temperature as a function of Tu (middle) and estimated diffusivities for salt-fingering condition. M15b over the inclined isoline at the LC edge, 09/08/2015 - 09/13/15.

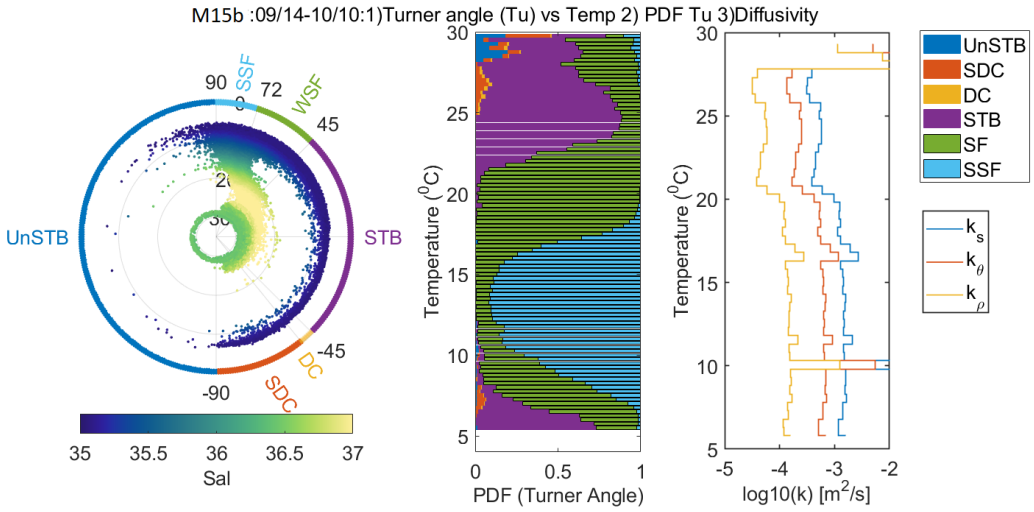

Figure 4.33: Polar plot of Tu (left, radius is observed temperature; diffusion class is labeled along the circumference), PDF of temperature as a function of Tu (middle) and estimated diffusivities for salt-fingering condition. M15b inside the LC, 09/14/2015 - 10/10/15.

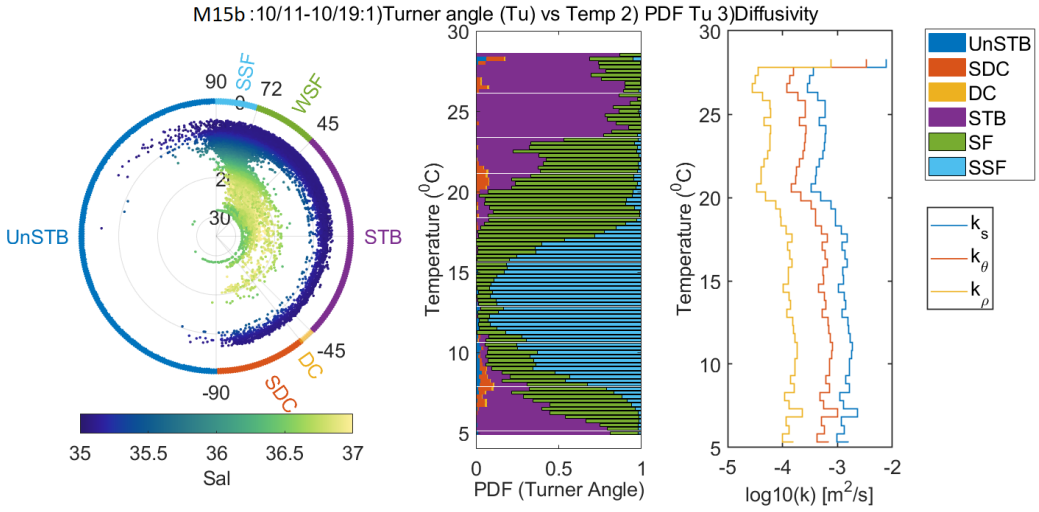

Figure 4.34: Polar plot of Tu (left, radius is observed temperature; diffusion class is labeled along the circumference), PDF of temperature as a function of Tu (middle) and estimated diffusivities for salt-fingering condition. M15b over inclined isoline during transit out of the LC, 10/11/2015 - 10/19/15.

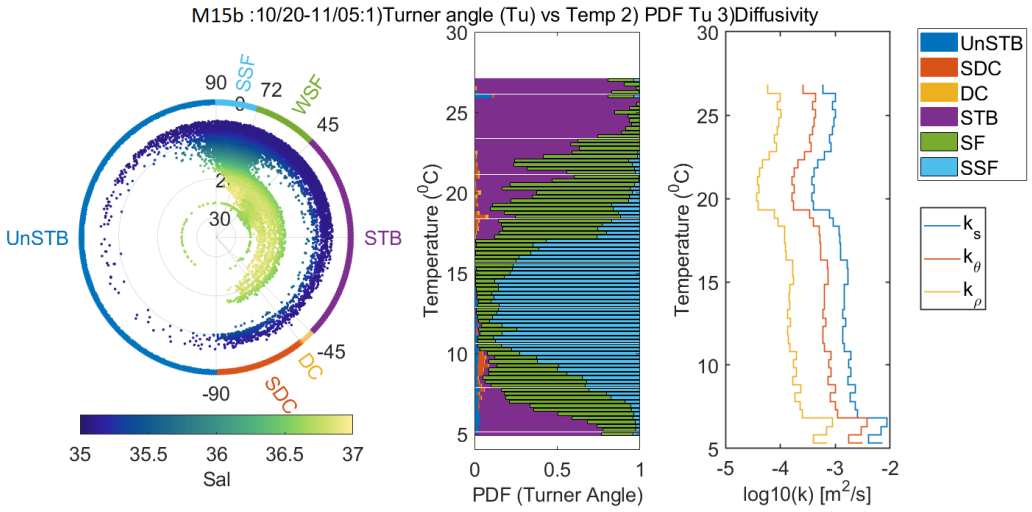

Figure 4.35: Polar plot of Tu (left, radius is observed temperature; diffusion class is labeled along the circumference), PDF of temperature as a function of Tu (middle) and estimated diffusivities for salt-fingering condition. M15b after exit out of LC, 10/20/2015 - 11/05/15.

Although Tu provides useful information to identify and characterize water masses stability conditions, the density ratio (R_ρ) has been used to identify the presence of fine-structure thermohaline staircases. The value of (R_ρ) provides the relative strength of the vertical salinity gradient to the temperature gradient and is commonly used to identify the existence of thermohaline staircase formation (Schmitt, 1981, 1987; Fer et al., 2010). For well-defined fine-structure thermohaline staircases to form, the values of R_ρ requires values < 1.7. The shape of the fine-structure thermohaline staircases becomes irregular for R_ρ between $1.7 - 2$, and no fine-structure form for R_ρ >2 (Schmitt, 1981; Schmitt et al., 1986).

Histograms of the occurrence frequency of density ratio (R_ρ) are constructed following Schmitt et al. (1986) to investigate the existence of thermohaline staircases in the GoM (Fig. 4.36 and 4.37). The LCE and LC data peaks in R_ρ occurrence for 1 <R_ρ <3 are consistent with the double-diffusive processes due to salt-fingering (Schmitt, 1981; Schmitt et al., 1986). Both histograms shows that a significant number of R_ρ values are <1.7, indicating the existence of the fine-structure thermohaline staircase in the GoM. However, the histogram of R_ρ occurrence for LCE and LC peaks near 1.9 and 1.8, which is not a favorable condition for well define fine-structure thermohaline staircases.

Information from the R_ρ value and the histogram were used to identify the fine-structure thermohaline staircases in the GoM. Fig. 4.38 and Fig. 4.39 show some detected fine-structure temperature staircases and corresponding salinity profiles from LCE glider missions. The location of the profiles is shown in the red box in Fig. 4.24. Similarly, the fine-structure temperature staircases, salinity, and the location of the profiles for LC glider missions are shown in Fig. 4.40, Fig. 4.41 and Fig. 4.25 (red box). Relatively well-defined staircases, i.e., with R_ρ values below 1.7 (blue box), are observed in the temperature and salinity profiles. From the shape of the fine-structure thermohaline staircases, the thickness of the stairs formed due to salt fingering $\leq 5\,m$.

Most of the observed staircases are irregular in shape i.e., 1 < R_ρ < 3. High turbulent mixing resulting from internal waves, rough topography, and boundary forcing may disrupt well-defined thermohaline staircases structure formation (Fer et al., 2010). Such irregular shape staircases were found in North Atlantic Centra water (Schmitt, 1981) and western tropical North Atlantic under

Subtropical Underwater (Fer et al., 2010) for $R_\rho > 1.7$.

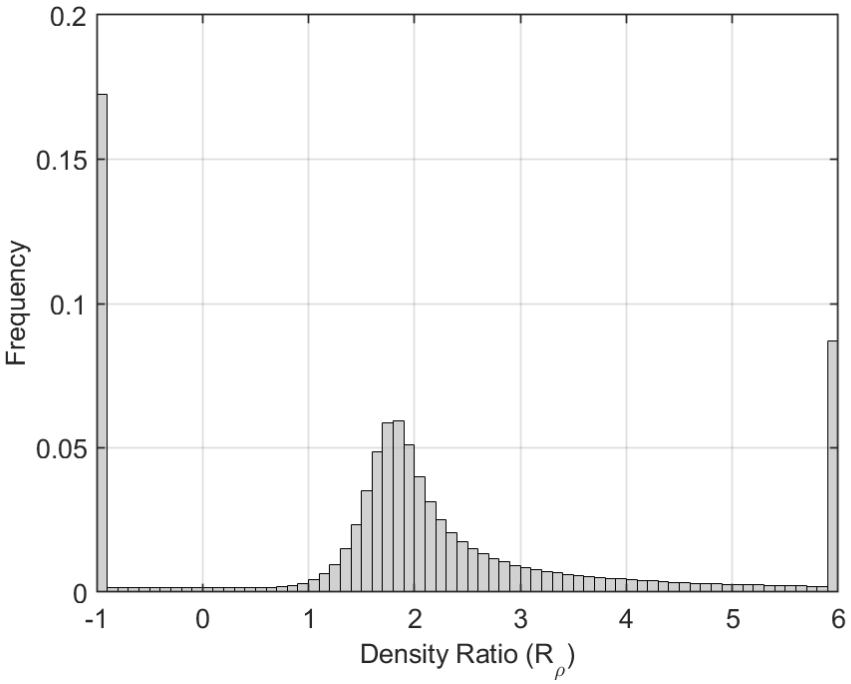

Figure 4.36: The distribution of $R\rho$ for the CTD from M15a. The end bins (at -1 and 6) include all data outside the indicated range. $R\rho < 0$ corresponds to stable water mass and $R\rho > 10$ corresponds to gravitationally unstable water mass.

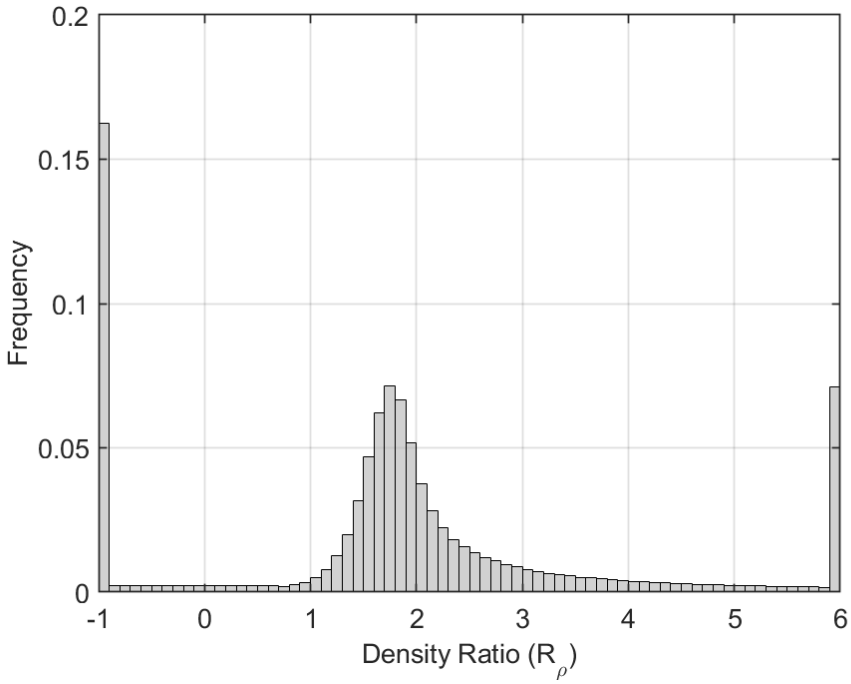

Figure 4.37: The distribution of $R\rho$ for the CTD from M15b. The end bins (at -1 and 6) include all data outside the indicated range. $R\rho < 0$ corresponds to stable water mass and $R\rho > 10$ corresponds to gravitationally unstable water mass.

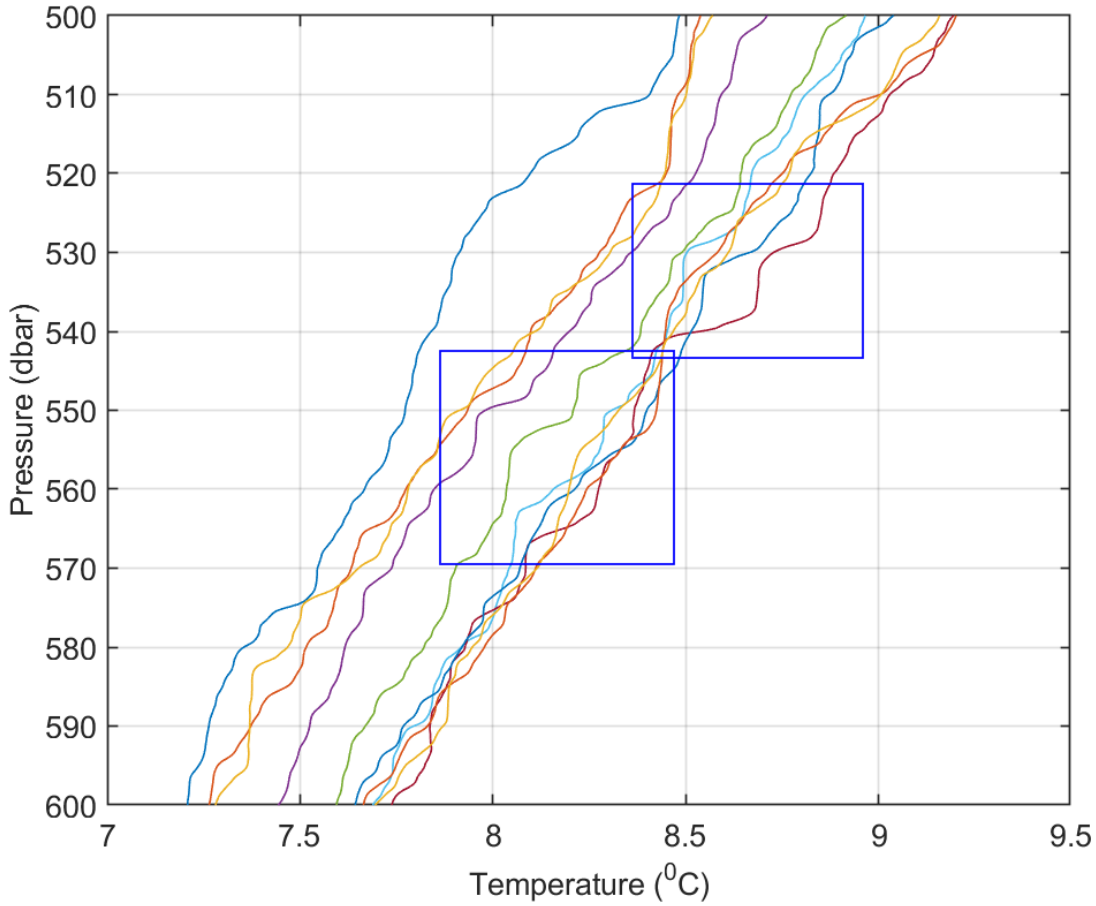

Figure 4.38: Temperature profiles from M15a that identify thermohaline staircases in the north-western GoM. The blue boxes are showing relatively well define finescale staircase.

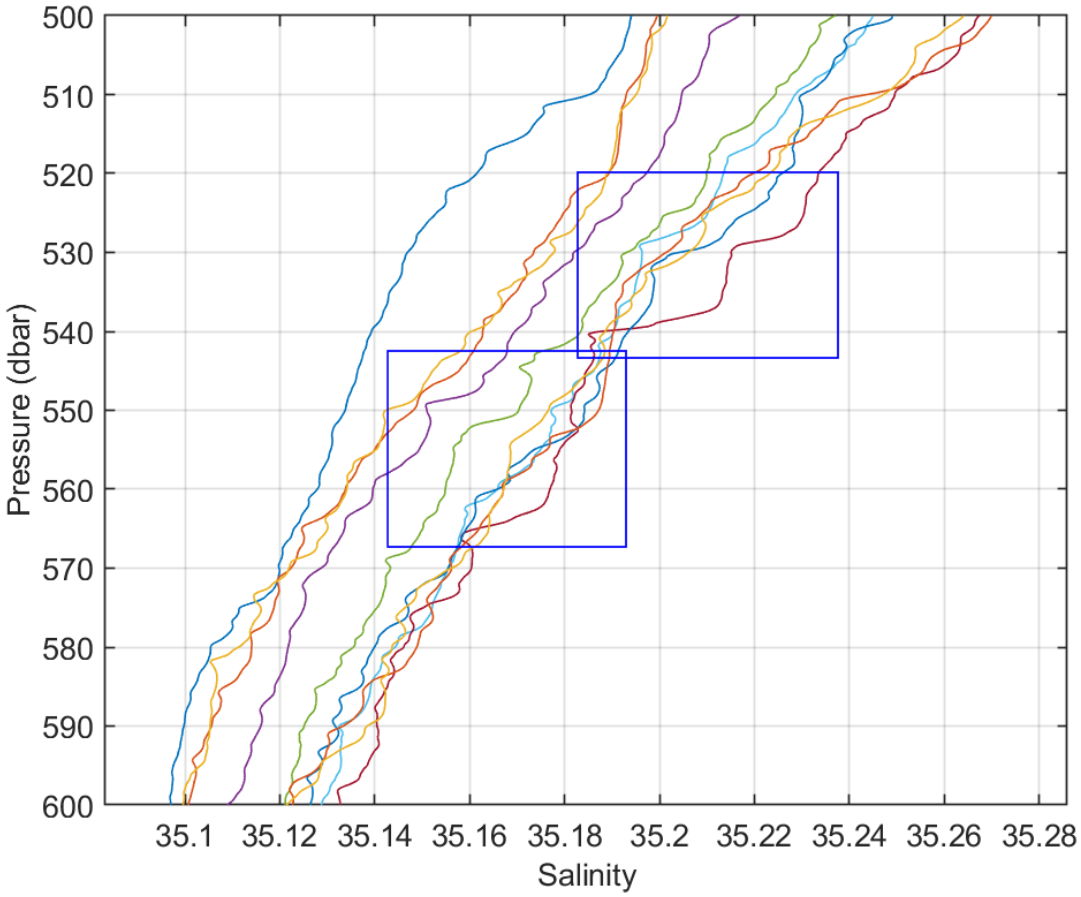

Figure 4.39: Corresponding salinity profiles of profiles shown in Fig. 4.38. The blue boxes show relatively well define finescale staircase.

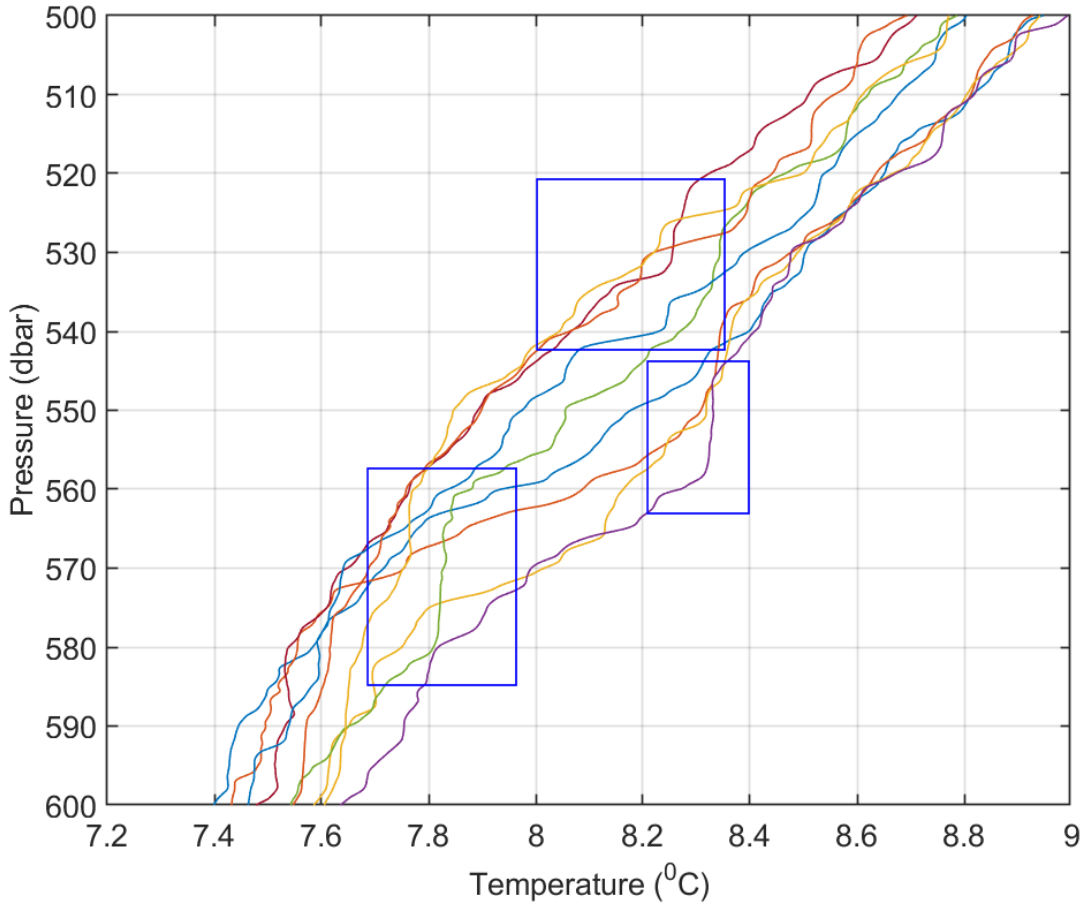

Figure 4.40: Temperature profiles from M15b identifying thermohaline staircases in the northwestern GoM. The blue boxes are showing relatively well define finescale staircase.

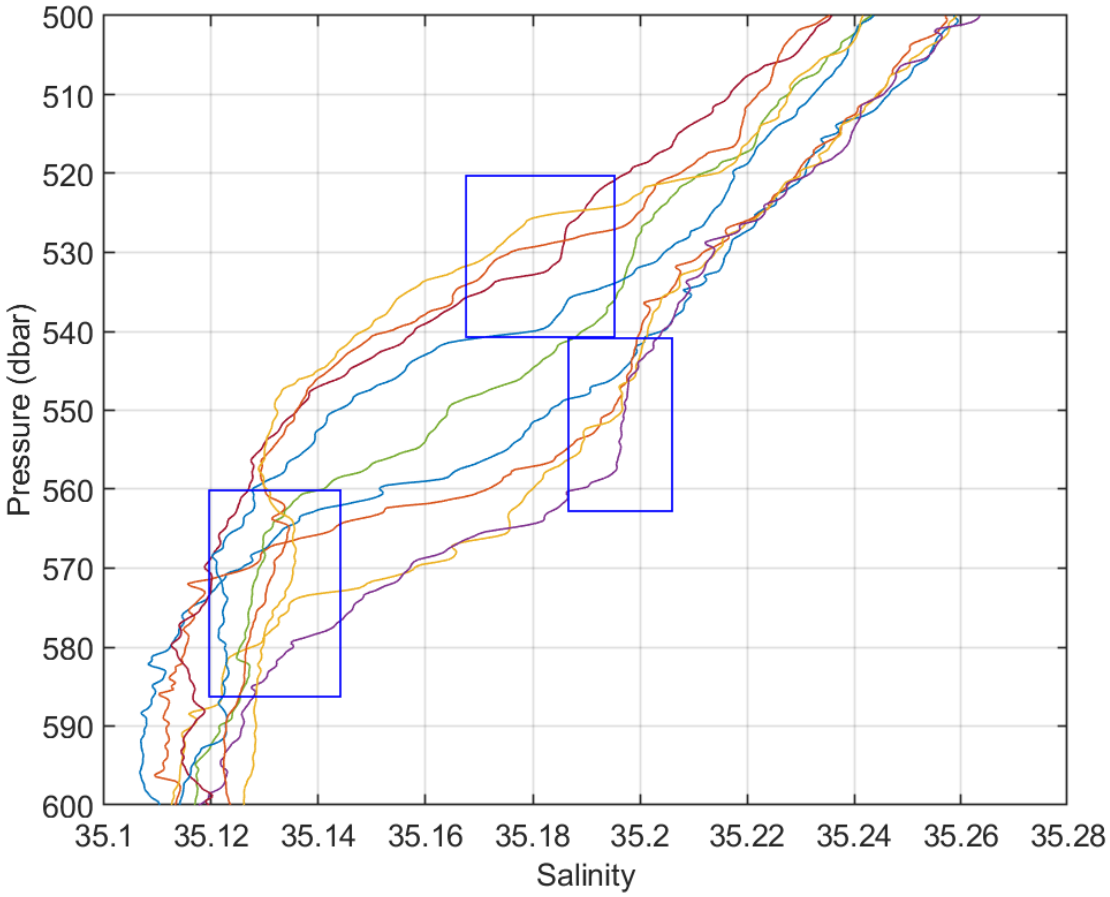

Figure 4.41: Corresponding salinity profiles of profiles shown in Fig. 4.40. The blue boxes are showing relatively well-define finescale staircase.

4.6 Summary: Mixing Characterization of Loop Current and Loop Current Eddy

The main objective of Chapter 4 is to characterize, categorize, and quantify the suite of mixing parameters and mixing processes in the deep northern GoM close to and including dynamical mesoscale processes associated with LCE and LC. We have used two long (90-day) missions Slocum glider missions for these calculations; the mixing estimates of chapter 4 were calculated in the absence of direct microstructure observations. We applied the glider vehicle-based turbulence estimation method (developed in Chapters 2 and 3) to estimate the TKE dissipation rate and diapycnal diffusivity to achieve the objective. Additionally, we assessed the contribution of double-

diffusive mixing processes in the GoM. The sawtooth sampling afforded by a buoyancy glider provided an opportunity to estimate turbulence in high spatiotemporal resolution in the study region. It provides insight into the spatiotemporal variation of the TKE dissipation and diapycnal diffusivity and underlying physical processes.

The turbulence structure in the northwestern GoM at water depths between 40 and $1000\,m$ in the proximity of Loop current and a Loop Current eddy is governed by multiple processes which depend on proximity to the eddy front and depth within the dynamic structure. Elevated TKE dissipation rates are found in the surface and upper thermocline. Elevated TKE dissipation rates are also found around the core of LC and LCE, but the core itself is quiescent. Further, we have categorized and identified the diffusion mixing process, i.e., double-diffusive regimes in Loop Current and Loop Current Eddy. Salt-fingering is the predominant double-diffusion process in the GoM. One key finding is the existence of thermohaline staircases.

By applying glider vehicle-based methodology to estimate oceanic mixing parameters allows investigators the capability to revisit the historical record of glider observation and quantify mixing processes in the absence of direct micro-structure observation. Because global oceanographic observational programs such as GOOS, OceanSites, and OOI, (Testor et al., 2010; Liblik et al., 2016; Testor et al., 2019) have recommended the continued use of autonomous vehicles, the application of these methods can continue to advance understanding of mixing processes, heat exchange, biochemical transformation, extreme weather formation and intensification, and improved parameterizations for predictive skill, assessment and validation of numerical weather and climate models. As chapter 3 shows, glider vehicle-based observations have limitations as to the spectral range in which dissipation rates can be accurately estimated and, therefore, cannot fully replace direct microstructure estimates. However, given the paucity of publically available direct measurements of ocean mixing, the glider-based estimation can be helpful in filling the spatial and temporal gap between direct measurements.

5. SUMMARY AND CONCLUSIONS

Understanding the mixing processes of the deep ocean can lead to improved understanding and prediction of short term (weather band) and long-term (climate-related) trends and variability. In the Gulf of Mexico, improved understanding, and prediction of the dominant physical processes, i.e., the Loop Current (LC) system can have profound ecological, social, and economic benefit and improve the well-being of coastal communities by improving resilience and sustainability. Although the LC system and associated mesoscale activities dominate surface circulation and are significant contributors to water mass properties, the mixing processes associated with LC are still not well understood due to limited amounts of data. This dissertation has combined observations from four Slocum glider missions in the deep Gulf of Mexico to quantify the turbulent and diffusive mixing processes in the basin.

Since their conceptual introduction in 1990, successful development in the late-1990's, and routine commercial availability in 2005, glider technology has shown the ability to provide real-time data for many scientific, commercial, and military applications. Underwater glider platforms offer relatively inexpensive and longer endurance than micro- and fine-structure observational system counterparts. The glider's sawtooth dive pattern allows for mapping water column properties in both spaces (vertical and horizontal) and time, which allows us to examine the spatial evolution of ocean properties. Over the last decade, scientists have expanded the use of buoyancy gliders for oceanographic applications, of ocean mixing and characterizing oceanic fronts and eddies.

In this dissertation, I have applied methodologies to calibrate and validate glider vehicle-based observations to simultaneously measured microstructure observations using the Thorpe scale (TM) method to estimate TKE dissipation rates(ϵ). The TM estimates of dissipation rate (ϵ), are then used to construct depth ϵ profiles (surface to 1000 m) using the Large Eddy Method (LEM). Updated TM-based calibration estimates allowed for the removal of the LEM methodology dependence requiring directly measured turbulence profile estimates. The estimation accuracy is compared and quantified against the glider carrying MicorRider survey. I have shown that the application of the

TM and LEM is valid to a factor of 2 when compared with the direct estimates from a simultaneous /co-located MicroRider deployment in the Gulf of Mexico (i.e., a glider equipped with MicroRider). Profile to profile comparison with ϵ reveals that LEM systematically overestimates when the magnitude of ϵ is low. Overestimation is attributed to the stratification-dependent detection limit of the LEM. Overestimation is mostly observed in deep water, where ϵ falls close to the noise level of LEM. Additionally, the low sampling resolution and noise level of glider sensors limit the measurements in low stratified water. However, LEM reasonably captured the spatiotemporal variability of turbulence as MicroRider measurement and when survey-averaged profiles of the three methods are compared, the differences are within the range of expected error. Spectral comparison of dissipation rates from the three methods (using histograms of occurrence) confirms that that the LEM and TM are able to capture dissipation rate variability greater than $1 \times 10^{-9}\, Wkg^{-1}$; however, less than this limit, only the direct measurement of TKE and dissipation rate (in regions of weak vertical density gradients) are robust. Despite this limitation, the TM /LEM-derived rate estimates are able to provide structures that are interpretable as associated with the underlying physical processes.

In Chapter 4, I have applied TM/LEM calibrated methodology to two Slocum Gliders surveys to construct the three-dimensional maps of turbulence of the northern GoM between in 2015. This time period is a particularly active for LC activity in the Gulf's interior. M15a sampled a Loop Current Eddy (LCE), and M15b sampled the Loop Current (LC) extension. Maps showing the temporal and spatial variability of ϵ were able to capture the well-defined turbulence structure of LCE and LC. Eddy-induced elevated ϵ are observed around the core of LC and LCE, but the interior of the eddy core is relatively quiescent when compared to the oceanic frontal regions of the eddy. Diapycnal mixing around the eddy cores is suppressed around the eddy core due to the presence of stronger stratification. Away from the eddy cores, where stratification is less, diapycnal mixing is enhanced.

The analysis quantifying the relative strength of the diffusion processes in the GoM concluded that Salt-finger is the dominant double-diffusive process in the GoM and is related to proximity to

the LC and depth of observation influence the strength of the salt-fingering in the water column. The vertical eddy diffusivities for heat and salt are calculated for salt finger conditions. Diffusivities for heat and salt have different values observed in the salt finger situation. Diffusive convection and lateral thermohaline intrusion have also been found around eddy boundaries. The potential for fine-structure thermohaline staircases is quantified and observations of irregular shape staircases in the M15a and M15b data sets are reported.

Accepting the limitations imposed by the LEM /TM method, glider-based measurements provide an economic estimation of ocean turbulence and has the potential to fill up the gaps between the direct microstructure measurements and provides opportunity to obtain mixing parameters of the world ocean in the absence of direct microstructure observations.

REFERENCES

Baird, M. E. and K. R. Ridgway (2012). The southward transport of sub-mesoscale lenses of bass strait water in the centre of anti-cyclonic mesoscale eddies. *Geophysical Research Letters 39*(2), 1–6.

Beaird, N., I. Fer, P. Rhines, and C. Eriksen (2012). Dissipation of turbulent kinetic energy inferred from seagliders: An application to the eastern nordic seas overflows. *Journal of Physical Oceanography 42*(12), 2268–2282.

Bebieva, Y. and M.-L. Timmermans (2016). An examination of double-diffusive processes in a mesoscale eddy in the arctic ocean. *Journal of Geophysical Research: Oceans 121*(1), 457–475.

Brannigan, L. (2016). Intense submesoscale upwelling in anticyclonic eddies. *Geophysical Research Letters 43*(7), 3360–3369.

Chen, K., P. Gaube, and E. Pallàs-Sanz (2020). On the vertical velocity and nutrient delivery in warm core rings. *Journal of Physical Oceanography 50*(6), 1557–1582.

Damien, P., J. Sheinbaum, O. Pasqueron de Fommervault, J. Jouanno, L. Linacre, and O. Duteil (2021). Do loop current eddies stimulate productivity in the gulf of mexico? *Biogeosciences 18*(14), 4281–4303.

Davis, R. E., C. C. Eriksen, C. P. Jones, et al. (2002). Autonomous buoyancy-driven underwater gliders. *The technology and applications of autonomous underwater vehicles*, 37–58.

Dickey, T. D. and R. R. Bidigare (2005). Interdisciplinary oceanographic observations: the wave of the future. *Scientia Marina 69*(S1), 23–42.

DiMarco, S. F., W. D. Nowlin, and R. Reid (2005). A statistical description of the velocity fields from upper ocean drifters in the gulf of mexico. *Geophysical Monograph-American Geophysical Union 161*, 101.

D'Asaro, E. A. and R.-C. Lien (2000a). Lagrangian measurements of waves and turbulence in stratified flows. *Journal of physical oceanography 30*(3), 641–655.

D'Asaro, E. A. and R.-C. Lien (2000b). The wave–turbulence transition for stratified flows. *Journal of Physical Oceanography 30*(7), 1669–1678.

Ekman, V. W. (1905). *On the influence of the earth's rotation on ocean-currents.* Almqvist & Wiksells boktryckeri, A.-B.,.

Eriksen, C. C., T. J. Osse, R. D. Light, T. Wen, T. W. Lehman, P. L. Sabin, J. W. Ballard, and A. M. Chiodi (2001). Seaglider: A long-range autonomous underwater vehicle for oceanographic research. *IEEE Journal of oceanic Engineering 26*(4), 424–436.

Evans, D. G., N. S. Lucas, V. Hemsley, E. Frajka-Williams, A. C. Naveira Garabato, A. Martin, S. C. Painter, M. E. Inall, and M. R. Palmer (2018). Annual cycle of turbulent dissipation estimated from seagliders. *Geophysical Research Letters 45*(19), 10–560.

Fer, I., P. Nandi, W. S. Holbrook, R. W. Schmitt, and P. Páramo (2010). Seismic imaging of a thermohaline staircase in the western tropical north atlantic. *Ocean Science 6*(3), 621–631.

Fer, I., A. K. Peterson, and J. E. Ullgren (2014). Microstructure measurements from an underwater glider in the turbulent faroe bank channel overflow. *Journal of Atmospheric and Oceanic Technology 31*(5), 1128–1150.

Ferron, B., H. Mercier, K. Speer, A. Gargett, and K. Polzin (1998). Mixing in the romanche fracture zone. *Journal of Physical Oceanography 28*(10), 1929–1945.

Fine, E. C., J. A. MacKinnon, M. H. Alford, and J. B. Mickett (2018). Microstructure observations of turbulent heat fluxes in a warm-core canada basin eddy. *Journal of Physical Oceanography 48*(10), 2397–2418.

Flierl, G. R. and R. P. Mied (1985). Frictionally induced circulations and spin down of a warm-core ring. *Journal of Geophysical Research: Oceans 90*(C5), 8917–8927.

Frajka-Williams, E., C. C. Eriksen, P. B. Rhines, and R. R. Harcourt (2011). Determining vertical water velocities from seaglider. *Journal of Atmospheric and Oceanic Technology 28*(12), 1641–1656.

Galbraith, P. S. and D. E. Kelley (1996). Identifying overturns in ctd profiles. *Journal of Atmospheric and Oceanic Technology 13*(3), 688–702.

Gargett, A. and T. Garner (2008). Determining thorpe scales from ship-lowered ctd density profiles. *Journal of Atmospheric and Oceanic Technology 25*(9), 1657–1670.

Gargett, A. E. (1989). Ocean turbulence. *Annual Review of Fluid Mechanics 21*(1), 419–451.

Goodman, L., E. R. Levine, and R. G. Lueck (2006). On measuring the terms of the turbulent kinetic energy budget from an auv. *Journal of Atmospheric and Oceanic Technology 23*(7), 977–990.

Goodman, L. and Z. Wang (2009). Turbulence observations in the northern bight of monterey bay from a small auv. *Journal of Marine Systems 77*(4), 441–458.

Gopalakrishnan, G., B. D. Cornuelle, I. Hoteit, D. L. Rudnick, and W. B. Owens (2013). State estimates and forecasts of the loop current in the gulf of mexico using the mitgcm and its adjoint. *Journal of Geophysical Research: Oceans 118*(7), 3292–3314.

Grant, H., A. Moilliet, and R. Stewart (1959). A spectrum of turbulence at very high reynolds number. *Nature 184*(4689), 808–810.

Gregg, M., H. Seim, and D. Percival (1993). Statistics of shear and turbulent dissipation profiles in random internal wave fields. *Journal of physical oceanography 23*(8), 1777–1799.

Gregg, M. C. (2021). *Mixing and its role in the ocean*, pp. 1–24. Cambridge: Cambridge University Press.

Hamilton, P. (1990). Deep currents in the gulf of mexico. *Journal of Physical Oceanography 20*(7), 1087–1104.

Hamilton, P., J. C. Larsen, K. D. Leaman, T. N. Lee, and E. Waddell (2005). Transports through the straits of florida. *Journal of physical oceanography 35*(3), 308–322.

Hamilton, P., R. Leben, A. Bower, H. Furey, and P. Pérez-Brunius (2018). Hydrography of the gulf of mexico using autonomous floats. *Journal of Physical Oceanography 48*(4), 773–794.

Howatt, T., S. Waterman, and T. Ross (2021). On using the finescale parameterization and thorpe scales to estimate turbulence from glider data. *Journal of Atmospheric and Oceanic Technology 38*(6), 1187–1204.

Jacob, S. D. and L. K. Shay (2003). The role of oceanic mesoscale features on the tropical cyclone–

induced mixed layer response: A case study. *Journal of physical oceanography 33*(4), 649–676.

Jaimes, B., L. K. Shay, and E. W. Uhlhorn (2015). Enthalpy and momentum fluxes during hurricane earl relative to underlying ocean features. *Monthly Weather Review 143*(1), 111–131.

Jung, E. and B. P. Kirtman (2016). Can we predict seasonal changes in high impact weather in the united states? *Environmental Research Letters 11*(7), 074018.

Koch, S., J. Barker, and J. Vermersch (1991). The gulf of mexico loop current and deepwater drilling. *Journal of Petroleum Technology 43*(09), 1046–1119.

Kunze, E., E. Firing, J. M. Hummon, T. K. Chereskin, and A. M. Thurnherr (2006). Global abyssal mixing inferred from lowered adcp shear and ctd strain profiles. *Journal of Physical Oceanography 36*(8), 1553–1576.

Leben, R. R. (2005). Altimeter-derived loop current metrics. *Geophysical Monograph-American Geophysical Union 161*, 181.

Ledwell, J. R., R. He, Z. Xue, S. F. DiMarco, L. J. Spencer, and P. Chapman (2016). Dispersion of a tracer in the deep g ulf of m exico. *Journal of Geophysical Research: Oceans 121*(2), 1110–1132.

Liang, X., M. Spall, and C. Wunsch (2017). Global ocean vertical velocity from a dynamically consistent ocean state estimate. *Journal of Geophysical Research: Oceans 122*(10), 8208–8224.

Liblik, T., J. Karstensen, P. Testor, P. Alenius, D. Hayes, S. Ruiz, K. J. Heywood, S. Pouliquen, L. Mortier, and E. Mauri (2016). Potential for an underwater glider component as part of the global ocean observing system. *Methods in Oceanography 17*, 50–82.

Lipphardt, B., A. Poje, A. Kirwan, L. Kantha, and M. Zweng (2008). Death of three loop current rings. *Journal of Marine Research 66*(1), 25–60.

Lueck, R. G., F. Wolk, and H. Yamazaki (2002). Oceanic velocity microstructure measurements in the 20th century. *Journal of Oceanography 58*(1), 153–174.

MacKinnon, J., L. St Laurent, and A. C. N. Garabato (2013). Diapycnal mixing processes in the ocean interior. In *International Geophysics*, Volume 103, pp. 159–183. Elsevier.

MacKinnon, J. A., J. D. Nash, M. H. Alford, A. J. Lucas, J. B. Mickett, E. L. Shroyer, A. F.

Waterhouse, A. Tandon, D. Sengupta, A. Mahadevan, et al. (2016). A tale of two spicy seas. *Oceanography 29*(2), 50–61.

MacKinnon, J. A., Z. Zhao, C. B. Whalen, A. F. Waterhouse, D. S. Trossman, O. M. Sun, L. C. St. Laurent, H. L. Simmons, K. Polzin, R. Pinkel, et al. (2017). Climate process team on internal wave–driven ocean mixing. *Bulletin of the American Meteorological Society 98*(11), 2429–2454.

Margirier, F., A. Bosse, P. Testor, B. l'Hévéder, L. Mortier, and D. Smeed (2017). Characterization of convective plumes associated with oceanic deep convection in the northwestern mediterranean from high-resolution in situ data collected by gliders. *Journal of Geophysical Research: Oceans 122*(12), 9814–9826.

McDougall, T. (1988). *Small-Scale Turbulence and Mixing in the Ocean: A Glossary*, Volume 46, pp. 3–9. Elsevier.

Melet, A., R. Hallberg, S. Legg, and K. Polzin (2013). Sensitivity of the ocean state to the vertical distribution of internal-tide-driven mixing. *Journal of Physical Oceanography 43*(3), 602–615.

Merckelbach, L., A. Berger, G. Krahmann, M. Dengler, and J. R. Carpenter (2019). A dynamic flight model for slocum gliders and implications for turbulence microstructure measurements. *Journal of Atmospheric and Oceanic Technology 36*(2), 281–296.

Merckelbach, L., D. Smeed, and G. Griffiths (2010). Vertical water velocities from underwater gliders. *Journal of Atmospheric and Oceanic Technology 27*(3), 547–563.

Merrell Jr, W. J. and J. M. Morrison (1981). On the circulation of the western gulf of mexico with observations from april 1978. *Journal of Geophysical Research: Oceans 86*(C5), 4181–4185.

Meunier, T., E. Pallás-Sanz, M. Tenreiro, E. Portela, J. Ochoa, A. Ruiz-Angulo, and S. Cusí (2018). The vertical structure of a loop current eddy. *Journal of Geophysical Research: Oceans 123*(9), 6070–6090.

Meunier, T., E. P. Sanz, M. Tenreiro, J. Ochoa, A. R. Angulo, and C. Buckingham (2019). Observations of layering under a warm-core ring in the gulf of mexico. *Journal of Physical Oceanography 49*(12), 3145–3162.

Mitchell, T. M., R. G. Lueck, M. J. Vogel, R. E. Raye, and G. Z. Forristall (2007). Turbulence measurements in a gulf of mexico warm-core ring. In *International Conference on Offshore Mechanics and Arctic Engineering*, Volume 42673, pp. 837–861.

Molodtsov, S., A. Anis, R. Amon, and P. Perez-Brunius (2020). Turbulent mixing in a loop current eddy from glider-based microstructure observations. *Geophysical Research Letters 47*(14), e2020GL088033.

Morrison, J. M., W. J. Merrell Jr, R. M. Key, and T. C. Key (1983). Property distributions and deep chemical measurements within the western gulf of mexico. *Journal of Geophysical Research: Oceans 88*(C4), 2601–2608.

Moum, J. N. (1996). Energy-containing scales of turbulence in the ocean thermocline. *Journal of Geophysical Research: Oceans 101*(C6), 14095–14109.

Mukherjee, S., S. Ramachandran, A. Tandon, and A. Mahadevan (2016). Production and destruction of eddy kinetic energy in forced submesoscale eddy-resolving simulations. *Ocean Modelling 105*, 44–59.

Munk, W. H. (1966). Abyssal recipes. In *Deep Sea Research and Oceanographic Abstracts*, Volume 13, pp. 707–730. Elsevier.

Nash, J. D., E. Kunze, J. M. Toole, and R. W. Schmitt (2004). Internal tide reflection and turbulent mixing on the continental slope. *Journal of Physical Oceanography 34*(5), 1117–1134.

Nasmyth, P. W. (1970). *Oceanic turbulence*. Ph. D. thesis, University of British Columbia.

National Academies of Sciences, Engineering, and Medicine and others (2018). *Understanding and predicting the gulf of mexico loop current: Critical gaps and recommendations*. National Academies Press.

NOAA (2015-2018). Sea level anomaly and geostrophic currents, multi-mission, global,optimal interpolation, gridded. Accessed: 06-24-2022.

Nowlin Jr, W. D., A. E. Jochens, M. K. Howard, S. F. DiMarco, and W. W. Schroeder (2000). Hydrographic properties and inferred circulation over the northeastern shelves of the gulf of mexico during spring to midsummer of 1998. *Gulf of Mexico Science 18*(1), 5.

Osborn, T. (1980). Estimates of the local rate of vertical diffusion from dissipation measurements. *Journal of physical oceanography 10*(1), 83–89.

Palmer, M. R., G. R. Stephenson, M. E. Inall, C. Balfour, A. Düsterhus, and J. Green (2015). Turbulence and mixing by internal waves in the celtic sea determined from ocean glider microstructure measurements. *Journal of Marine Systems 144*, 57–69.

Pezzi, L. P., R. B. de Souza, M. F. Santini, A. J. Miller, J. T. Carvalho, C. K. Parise, M. F. Quadro, E. B. Rosa, F. Justino, U. A. Sutil, et al. (2021). Oceanic eddy-induced modifications to air–sea heat and co2 fluxes in the brazil-malvinas confluence. *Scientific reports 11*(1), 1–15.

Pinkel, R., W. Munk, P. Worcester, B. D. Comuelle, D. Rudnick, J. Sherman, J. H. Filloux, B. D. Dushaw, B. M. Howe, T. B. Sanford, et al. (2000). Ocean mixing studied near hawaiian ridge. *Eos, Transactions American Geophysical Union 81*(46), 545–553.

Putrasahan, D., I. Kamenkovich, M. Le Hénaff, and B. Kirtman (2017). Importance of ocean mesoscale variability for air-sea interactions in the gulf of mexico. *Geophysical Research Letters 44*(12), 6352–6362.

Richards, K. J., S.-P. Xie, and T. Miyama (2009). Vertical mixing in the ocean and its impact on the coupled ocean–atmosphere system in the eastern tropical pacific. *Journal of climate 22*(13), 3703–3719.

Rivas, D., A. Badan, J. Sheinbaum, J. Ochoa, and J. Candela (2008). Vertical velocity and vertical heat flux observed within loop current eddies in the central gulf of mexico. *Journal of Physical Oceanography 38*(11), 2461–2481.

Ruddick, B. (1983). A practical indicator of the stability of the water column to double-diffusive activity. *Deep Sea Research Part A. Oceanographic Research Papers 30*(10), 1105–1107.

Rudnick, D. L., R. E. Davis, and J. T. Sherman (2016). Spray underwater glider operations. *Journal of Atmospheric and Oceanic Technology 33*(6), 1113–1122.

Rudnick, D. L., G. Gopalakrishnan, and B. D. Cornuelle (2015). Cyclonic eddies in the gulf of mexico: Observations by underwater gliders and simulations by numerical model. *Journal of Physical Oceanography 45*(1), 313–326.

Rudnick, D. L., T. S. Johnston, and J. T. Sherman (2013). High-frequency internal waves near the luzon strait observed by underwater gliders. *Journal of Geophysical Research: Oceans 118*(2), 774–784.

Schmitt, R. W. (1981). Form of the temperature-salinity relationship in the central water: Evidence for double-diffusive mixing. *Journal of Physical Oceanography 11*(7), 1015–1026.

Schmitt, R. W. (1987). The caribbean sheets and layers transects (c-salt) program. *Eos, Transactions American Geophysical Union 68*(5), 57–60.

Schmitt, R. W. (2003). Observational and laboratory insights into salt finger convection. *Progress in oceanography 56*(3-4), 419–433.

Schmitt, R. W. (2012). Finger puzzles. *Journal of fluid mechanics 692*, 1–4.

Schmitt, R. W., R. G. Lueck, and T. M. Joyce (1986). Fine-and microstructure at the edge of a warm-core ring. *Deep Sea Research Part A. Oceanographic Research Papers 33*(11-12), 1665–1689.

Schmitz Jr, W., D. Biggs, A. Lugo-Fernandez, L.-Y. Oey, and W. Sturges (2005). A synopsis of the circulation in the gulf of mexico and on its continental margins. *Washington DC American Geophysical Union Geophysical Monograph Series 161*, 11–29.

Schmitz Jr, W. J. (2005). Cyclones and westward propagation in the shedding of anticyclonic rings from the loop current. *Washington DC American Geophysical Union Geophysical Monograph Series 161*, 241–261.

Schultze, L. K., L. M. Merckelbach, and J. R. Carpenter (2017). Turbulence and mixing in a shallow shelf sea from underwater gliders. *Journal of Geophysical Research: Oceans 122*(11), 9092–9109.

Shay, L. K., G. J. Goni, and P. G. Black (2000). Effects of a warm oceanic feature on hurricane opal. *Monthly Weather Review 128*(5), 1366–1383.

Sherman, J., R. E. Davis, W. Owens, and J. Valdes (2001). The autonomous underwater glider" spray". *IEEE Journal of Oceanic Engineering 26*(4), 437–446.

Smyth, W. and S. Thorpe (2012). Glider measurements of overturning in a kelvin-helmholtz billow

train. *Journal of Marine Research 70*(1), 119–140.

Sosa-Gutiérrez, R., E. Pallàs-Sanz, J. Jouanno, A. Chaigneau, J. Candela, and M. Tenreiro (2020). Erosion of the subsurface salinity maximum of the loop current eddies from glider observations and a numerical model. *Journal of Geophysical Research: Oceans 125*(7), e2019JC015397.

Spencer, L. J., S. F. DiMarco, Z. Wang, J. J. Kuehl, and D. A. Brooks (2016). Asymmetric oceanic response to a hurricane: Deep water observations during hurricane isaac. *Journal of Geophysical Research: Oceans 121*(10), 7619–7649.

St. Laurent, L. and S. Merrifield (2017). Measurements of near-surface turbulence and mixing from autonomous ocean gliders. *Oceanography 30*(2), 116–125.

Stern, M. E. (1960). The "salt-fountain" and thermohaline convection. *Tellus 12*(2), 172–175.

Stommel, H. (1989). The slocum mission. *Oceanography 2*(1), 22–25.

Talley, L. D. (2011). *Descriptive physical oceanography: an introduction*. Academic press.

Testor, P., B. De Young, D. L. Rudnick, S. Glenn, D. Hayes, C. M. Lee, C. Pattiaratchi, K. Hill, E. Heslop, V. Turpin, et al. (2019). Oceangliders: a component of the integrated goos. *Frontiers in Marine Science 6*, 422.

Testor, P., G. Meyers, C. Pattiaratchi, R. Bachmayer, D. Hayes, S. Pouliquen, L. Petit de la Villeon, T. Carval, A. Ganachaud, L. Gourdeau, et al. (2010). Gliders as a component of future observing systems. OceanObs' 09.

Thorpe, S. (2012). Measuring overturns with gliders. *Journal of Marine Research 70*(1), 93–117.

Thorpe, S. A. (1977). Turbulence and mixing in a scottish loch. *Philosophical Transactions of the Royal Society of London. Series A, Mathematical and Physical Sciences 286*(1334), 125–181.

Thorpe, S. A. et al. (2007). *An introduction to ocean turbulence*, Volume 10. Cambridge University Press Cambridge.

Turner, J. S. (1979). *Buoyancy effects in fluids*. Cambridge university press.

Van Gastel, P. and J. L. Pelegrí (2004). Estimates of gradient richardson numbers from vertically smoothed data in the gulf stream region. *Scientia Marina 68*(4), 459–482.

Vidal, V. M., F. V. Vidal, and J. M. Pérez-Molero (1992). Collision of a loop current anticyclonic

ring against the continental shelf slope of the western gulf of mexico. *Journal of Geophysical Research: Oceans 97*(C2), 2155–2172.

Wang, Z., S. F. DiMarco, and K. Polzin (2018). Turbulence observations in the northern gulf of mexico from a slocum glider. In *2018 OCEANS-MTS/IEEE Kobe Techno-Oceans (OTO)*, pp. 1–6. IEEE.

Wang, Z., S. F. DiMarco, and S. A. Socolofsky (2016). Turbulence measurements in the northern gulf of mexico: Application to the deepwater horizon oil spill on droplet dynamics. *Deep Sea Research Part I: Oceanographic Research Papers 109*, 40–50.

Whalen, C., L. Talley, and J. MacKinnon (2012). Spatial and temporal variability of global ocean mixing inferred from argo profiles. *Geophysical Research Letters 39*(18), 1–6.

Wolk, F., R. Lueck, and L. S. Laurent (2009). Turbulence measurements from a glider. In *OCEANS 2009*, pp. 1–6. IEEE.

Wunsch, C. and R. Ferrari (2004). Vertical mixing, energy, and the general circulation of the oceans. *Annu. Rev. Fluid Mech. 36*, 281–314.